

TU

Technische Universität Wien

Dissertation

Precipitation Kinetics in Al-Alloys Observed by Dilatometry

ausgeführt zum Zwecke der Erlangung des akademischen Grades eines Doktors der technischen
Wissenschaften unter der Leitung von

O.Univ.Prof. Dipl.-Ing. Dr.techn. Hans Peter Degischer

E 308

Institute of Materials Science and Technology

eingereicht an der Technischen Universität Wien
Faculty of Mechanical and Industrial Engineering

von

Hamid Reza Mohammadian Semnani

0525968

Felbigergasse 75/16

1140 Wien

به نام خداوند جان و خرد

In the name of God

To my father and mother

Acknowledgments

It has been a valuable and pleasant time during my studies at the Institute of materials science and Technology of Vienna University of Technology in Austria. I received guidance, advice, help and encouragement from a large number of people whom I am truly grateful to. First and foremost I would like to express my sincere appreciation to my Supervisor, Professor Hans Peter Degischer for his invaluable guidance through my doctoral thesis. Each stage of my thesis was guided by him. I have learned so much from him in both technical and non-technical aspects of life. I gratefully appreciate the guidance and help of Dr. Falahati For many useful critical comments and helpful discussions. I am also very grateful to Priv. Doz. Dr. Helmut Kaufmann for accepting to review this work, interesting comments and suggestions. I would also like to express my appreciation to my colleagues and friend of the institute for their assistance and collaboration in this thesis and creating enjoyable working atmosphere particularly Guillermo, Warcho, Cecilia, Fernando Christian, Heide, Sthephan Tomas and especially S.R.Aalavi and his family that I and my family had a very pleasure time with them in Vienna. I would like to thanks to the secretaries of our institute Silvia, Dagmar and Tanja that they helped me a lot in officialism field.

I owe an extra special thank you to my wife Elahe her love and Encouragement is greatly cherished. Special gratitude goes to my son Parham he warms my heart everyday. Last but not least I would like to express my deep gratitude to my parents brothers and sister who encouraged and supported me in all respects.

Kurzfassung

Aluminium wird in vielen industriellen Arbeitsfeldern verwendet. Angefangen von Getränkedosen und Aluminiumfolie bis hin zu großen Containern und Flugzeugstrukturen ist die Gewichtsreduzierung der Produkte die treibende Kraft. Dies wird durch kontinuierliche Verbesserung der Aluminiumlegierungen hinsichtlich Zusammensetzung, Herstellungstechnologien und Wärmebehandlungen bewerkstelligt.

Aluminiumlegierungen zeichnen sich durch gute Umformbarkeit aus. Dies ermöglicht wirtschaftliches Walzen, Extrudieren und Schmieden in die gewünschte Form. Mechanische Eigenschaften wie zum Beispiel die Festigkeit werden durch Kaltumformung, Anlassen und/oder Ausscheidungshärtung signifikant gesteigert.

Aushärtbare Aluminiumlegierungen enthalten ein oder mehrere lösliche Bestandteile, wie Kupfer, Magnesium, Silizium und Zink, welche individuell oder als Verbindung ausgeschieden werden. Diese gelösten Atome sammeln sich stellenweise innerhalb der Matrix der Legierung an, wodurch die Ausscheidung eingeleitet wird. Eine solche Phasentransformation wird durch die Tatsache hervorgerufen, dass die Legierung in ihrem Ausgangszustand weit entfernt vom Gleichgewichtszustand ist und, dass bei ausreichender Zeit und Temperatur, Diffusion dieser Atome schrittweise zum Gleichgewicht führt.

Ingenieurwerkstoffe werden während der Umformung hohen Temperaturen ausgesetzt was, thermische Ausdehnung verursacht. In dieser Arbeit werden Dilatometerversuche eingesetzt, um Wärmeausdehnungseffekte durch Ausscheidungen zu messen.

Ausgangspunkt dieser Arbeit ist die Studie der Ausscheidungsfolge von Al-Ge, Al-Ge-Si mittels Dilatometrie und der Vergleich dieser Ergebnisse mit den Werten der Differential Scanning Kalorimetrie (DSC). Dilatometrie wird für die Bestimmung der Formation und Auflösung von Ge, Si oder Si-Ge Ausscheidungen erfolgreich eingesetzt. DSC der gleichen Proben belegen die Temperaturen der Ausscheidungsbildung und -Auflösungen. Weiters werden unterschiedliche Al-Legierungen (3XXX, 4XXX, 5XXX, 6XXX, 7XXX) untersucht, um die Temperaturabhängigkeit des linearen Ausdehnungskoeffizient (CTE) mit Ausscheidungsvorgängen zu korrelieren.

Entsprechend den Dilatometermessungen von AW3003 ist die Ausscheidung von Mn zwischen 300 und 380°C, und seine Auflösung über 450°C in CTE(T) -Kurvenerkennbar.

Isotherme Dilatometrieexperimente bei 200°C von Al-Mg-Legierungen (5XXX) zeigen eine Expansion entsprechend der Bildung von β''/β' -Phasen, wobei eine Volumenreduktion eine Auflösung bei 300°C zeigt.

Die Festigkeitssteigerung von Al-Mg-Si-Legierungen (6XXX) wird den GP Zonen und β'' -Phasen zugeschrieben. In diesen Legierungen erzeugt überschüssiges Si Ausscheidungen und somit Wärmeausdehnungen. Die DSC Thermogramme zeigen Mg_2Si und Si Ausscheidungen, während CTE(T) von Si Ausscheidungen dominiert wird. Mittels Dilatometrie ist es nicht möglich den Ausscheidungsvorgang von Mg_2Si darzustellen.

DSC und Dilatometrie Versuche an Al-Zn-Mg-Legierungen (7XXX) zeigen die Auflösung von GP(I) Zonen und die Bildung und spätere Auflösung von η' and η Ausscheidungen.

Die Dilatometrie erlaubt die Beschreibung der Temperatur- und Zeitabhängigkeit der Si, Ge, Al_6Mn , Al_8Mg_5 Ausscheidungen und von Modifikationen von Zn_2Mg in Aluminium legierungen..

Isotherme Kalorimetrie kann eingesetzt werden, um die Zeitabhängigkeit der Ausscheidungs und/oder Auflösung in Legierungen bei konstanter Temperatur zu untersuchen, was mit Kalorimetrie nicht möglich ist.

Abstract

Aluminum is used in many industrial fields. From soda cans and household foil to rigid containers, automotive and aircraft structures. Demands for weight reductions of products are the driving force for continuous improvement of standard alloys in regard of composition, manufacturing technologies and heat treatments.

Aluminum alloy systems are characterized by good workability. That enables these alloys to be economically rolled, extruded or forged into useful shapes. Mechanical properties such as strength are significantly altered by cold working, annealing, and/or precipitation hardening.

Heat-treatable aluminum alloys contain one or more soluble constituents such as copper, magnesium, silicon and zinc that precipitate individually or as compounds. The solute atoms progressively cluster within the matrix grains of the alloy, this process initiates precipitation. Such a phase transformation responds to the fact that the alloy is initially in a state far from equilibrium (W.Q and T4 conditions) and, given sufficient time, diffusion of atoms occurs progressively to transform towards the equilibrium situation.

Engineering materials exposed to elevated temperatures during manufacturing and service needs exact thermal expansion values. In this thesis dilatometric techniques are used to measure thermal expansion effects originated from precipitation, where phase transformations cause changes in the specific volume of the alloy.

The starting point of this research is to study the precipitation sequence of Al-Ge, Al-Ge-Si by means of dilatometry and to compare the results with differential scanning calorimetry. Dilatometry is used successfully to identify the formation and dissolution of Ge, Si or Si-Ge precipitates due to the change in atomic volume from solid solution to precipitates in diamond structure. Differential scanning calorimetry (DSC) on the same samples confirms the temperatures of precipitation and dissolution. Furthermore the different series (3XXX, 4XX.X, 5XXX, 6XXX, 7XXX) of Al alloys are investigated to look for volume changes related to precipitation.

According to dilatometry measurements on AW3003, the precipitation of Mn between about 300 and 380°C and its dissolution above 450°C are evident in CTE(T).

Isothermal dilatometry experiments at 200°C on Al-Mg (5XXX) alloy show an expansion corresponding to the formation of β''/β' , whereas shrinkage indicates dissolution at 300°C.

Increase in hardness of Al-Mg-Si (6XXX) alloys is attributed to GP zones and β'' phases. In these alloys excess Si precipitates as well which produces increased thermal expansion. The corresponding DSC thermograms show both Mg_2Si and Si precipitation whereas $CTE(T)$ is dominated by Si precipitation. Dilatometry does not reveal the precipitation sequence of Mg_2Si .

DSC and dilatometry tests on Al-Zn-Mg (7XXX) alloys, both show the dissolution of GP(I) zones and the formation and later dissolution of η' and η precipitates.

Dilatometry allows to describe the temperature and time dependence of precipitation of Si, Ge, Al_6Mn , Al_8Mg_5 and of modification of Zn_2Mg . Isothermal dilatometry can be applied to alloys containing those phases in order to reveal the kinetics of precipitation and/or dissolution at constant temperatures which is not possible by calorimetry.

TABLE OF CONTENTS

AKNOWLEDGMENTS	I
KURZFASSUNG	II
ABSTRACT	IV
TABLE OF CONTENTS	VI
1. INTRUDUCTION	1
2 STATEOFART	3
2.1ALUMINIUM ANDALUMINIUM ALLOYS	3
2.1.1CLASSIFICATION OF ALUMINIUM ALLOYS.....	4
2.1.2 DESIGNATION OF WROUGHT ALUMINIUM ALLOYS.....	5
2.1.3 DESIGNATION OF CAST ALUMINIUM ALLOYS.....	6
2.1.4 TEMPER DESIGNATION SYSTEMS.....	6
2.2 STRENGHTENING MECHANISMS.....	8
2.2.1 HEAT TREATMENT OF ALUNINIUM ALLOYS.....	8
2.2.2 STAGES OF AGE HARDENING TREATMENT.....	8
2.2.2.1 SOLUTION HEAT TREATMENT.....	8
2.2.2.2 QUENCHING.....	9
2.2.2.3 AGEING.....	9
2.3 PRECIPITATION HARDENINGAND.....	12
2.3.1 PRECIPITATION SEQUENCE IN 2XXX SERIES.....	12
2.3.2 PRECIPITATION SEQUENCE IN 5XXX SERIES.....	15
2.3.3 PRECIPITATION SEQUENCE IN 6XXX SERIES.....	16
2.3.4 PRECIPITATION SEQUENCE IN 7XXX SERIES.....	18
2.4 NON HEAT TREATABLE ALLOYS.....	20
2.4.1 Al-Si SYSTEM.....	21
2.4.2 Al-Ge SYSTEM.....	21
2.5 THERMAL ANALYSIS METHODS.....	22
2.5.1 DEFINITION.....	22

2.5.2 DIFFERENTIAL SCANNING CALORIMETRY (DSC)	23
2.5.3 DIFFERENTIAL SCANNING CALORIMETRY THERMOGRAMS OF SOME AL ALLOYS.....	24
2.5.4 DILATOMETRY.....	28
2.6 PHYSICAL AND MECHANICAL PROPERTIES OF DIFFERENT ALUMINIUM ALLOYS SYSTEMS.....	28
3 EQUATIONS AND BASIC MODEL APPLIED.....	30
3.1 THERMAL ANALYSES.....	30
3.1.1 VOLUMETRIC THERMAL EXPANSION.....	30
3.1.2 LINEAR THERMAL EXPANSION.....	31
3.2 KINETIC BACKGROUND TO THERMAL ANALYSIS AND CALORIMETRY.....	34
3.2.1 INTRODUCTION.....	34
3.2.2 REACTION RATE.....	35
3.2.3 THE KINETICS OF HOMOGENEOUSE TRANSFORMATION.....	35
3.2.4 THE KINETICS OF HETROGENEOUSE REACTION.....	35
3.2.5 KINETIC INTERFACE.....	36
3.2.6 CALORIMETRIC METHODS AND INTERPRETING DSC CURVES.....	36
3.3 BASIC CONCEPTS IN THERMODZNAMICS.....	38
3.3.1 PHASE TRANSFORMATIONS.....	38
3.3.2 EQUILIBRIUME.....	38
3.4 PARTICLE PRECIPITATION.....	39
3.4.1 NUCLIATION.....	39
3.4.2 GROWTH RATE.....	40
3.4.3 GROWTH.....	40
3.4.3.1 OSTWALD RIPENING.....	41
4 DESCRIPTION OF METHODOLOGY.....	42
4.1 MATERIALS.....	42
4.1.1 Al-Ge SYSTEM.....	42

4.1.2 Al-Ge-Si SYSTEM.....	43
4.1.3 Al-Mn ALLOYS (3XXX SERIES).....	46
4.1.4 Al-Si ALLOYS (4XXX SERIES).....	48
4.1.5 Al-Mg ALLOYS (5XXX SERIES).....	50
4.1.6 Al-Mg-Si ALLOYS (6XXX SERIES).....	51
4.1.7 Al-Zn-Mg ALLOYS (7XXX SERIES)	53
4.2 EXPERIMENTAL METHODS.....	54
4.2.1 HARDNESS MEASUREMENTS.....	54
4.2.2 GENERAL DESCRIPTION OF DIFFERENTIAL SCANNING CALORIMETRY	
DSC2920CE.....	54
4.2.2.1 CALIBRATION OF DSC.....	56
4.2.2.1.1 BASE LINE SLOPE AND OFFSET CALIBRATION.....	56
4.2.2.1.2 CELL CONSTANT CALIBRATION.....	56
4.2.2.1.3 TEMPERATURE CALIBRATION.....	57
4.2.2.2 BASE LINE CORRECTION IN CALORIMETRY.....	57
4.2.2.3 PROCEDURE OF DSC TESTS.....	57
4.2.2.4 THE HEAT TREATMENT BEFORE DSC.....	58
4.2.3 GENERAL DESCRIPTION OF TMA 2940.....	61
4.2.3.1 CALIBRATION OF TMA.....	62
4.2.3.2 PROCEDURE OF DILATOMETRY TEST.....	62
5 EXPERIMENTAL RESULTS.....	64
5.1 METALLOGRAPHY OF SAMPLES.....	64
5.1.1 Al-Ge AND Al-Ge-Si ALLOYS.....	64
5.1.2 Al-Mn ALLOYS (3XXX SERIES).....	64
5.1.3 Al-Si ALLOYS (4XX.X SERIES).....	64
5.1.4 Al-Mg ALLOYS (5XXX SERIES).....	65
5.1.5 Al-Mg-Si ALLOYS (6XXX SERIES).....	65
5.1.6 Al-Zn-Mg ALLOYS (7XXX SERIES).....	65
5.2 HARDNESS OF SAMPLES.....	65

5.2.1 AlGe,AlGe ₃ ALLOYS.....	65
5.2.2 Al-Mg-Si 6XXX SERIES (6016CC,6016DC).....	66
5.2.3 Al-Zn-Mg ALLOYS (7XXX SERIES).....	66
5.3 CALORIMETRY.....	66
5.3.1 DIFFERENTIAL SCANNING CALORIMETRY OF AlGe AND AlGe ₃ ALLOYS.	66
5.3.2 DIFFERENTIAL SCANNING CALORIMETRY OF AlSi ₁ Ge ₅ AND AlSi ₁₁ Ge ₅ ALLOYS.....	66
5.3.3 DIFFERENTIAL SCANNING CALORIMETRY OF AlSi _{1.7} AND AlSi ₁₂	67
5.3.4 DIFFERENTIAL SCANNING CALORIMETRY OF Al-Mg-Si ALLOYS.....	67
5.3.5 DIFFERENTIAL SCANNING CALORIMETRY OF Al-Zn-Mg ALLOYS.....	68
5.4 DILATOMETRY.....	68
5.4.1 DILATOMETRY OF AlGe, AlGe ₃ , AlSi ₁ Ge ₅ AND AlSi ₁₁ Ge ₅ ALLOYS	68
5.4.2 DILATOMETRY OF Al-Mn ALLOY.....	69
5.4.3 DILATOMETRY OF AlSi ALLOYS.....	69
5.4.4 DILATOMETRY OF Al-Mg ALLOYS.....	70
5.4.5 DILATOMETRY OF Al-Mg-Si ALLOYS.....	70
5.4.6 DILATOMETRY OF Al-Zn-Mg ALLOY.....	70
5.5 METALLOGRAPHY PICTURES	71
5.6 HARDNESS GRAPHS.....	87
5.7 DSC THERMOGRAMS.....	89
5.8 DILATOMETRY GRAPHS.....	93
6 DISCUSSION OF RESULTS.....	103
6.1 Al-Ge AND Al-Ge-Si ALLOYS.....	103
6.2 Al-Mn ALLOY.....	107
6.3 Al-Si ALLOY.....	108
6.4 Al-Mg ALLOY.....	110
6.5 Al-Mg-Si ALLOYS.....	111
6.6 Al-Zn-Mg ALLOY.....	114
7 CONCLUSIONS.....	116

7.1 Al-Ge AND Al-Ge-Si ALLOYS.....	116
7.2 Al-Mn ALLOY.....	117
7.3 Al-Si ALLOY.....	117
7.4 Al-Mg ALLOY.....	117
7.5 Al-Mg-Si ALLOYS.....	118
7.6 Al-Zn-Mg ALLOY.....	119
7.7 IDENTIFICATION OF PRECIPITATION.....	119

1 Introduction

Aluminium and its alloys are used in many aspects of modern life, from Soda cans and household foils to rigid containers, automotive and aircraft structures. Aluminium alloys have a wide range of applications due to the large variety in mechanical properties. As is well known, the properties of an aluminium alloy are greatly influenced by its internal structure such as the grain size, and the presence of various intermetallic phases, their shape, size and distribution.

One important example of application is within the transportation sector where Aluminum alloys are used due to their high specific stiffness and strength (divided by density). Other important applications are architecture (decorative aspects), packaging (corrosion resistance and non-toxic) and heat exchangers (high thermal conductivity and corrosion resistance), etc. Aluminum wrought alloys are being used more extensively nowadays as structural and sheet materials for vehicle bodies, as automobile manufacturers strive for improved fuel economy by reducing vehicle weight. Aluminium alloy systems are characterized by good workability that enables these alloys to be economically rolled, extruded or forged into useful shapes. Mechanical properties such as strength are altered significantly with cold working, annealing, and/or precipitation hardening. Heat-treatable Aluminium alloys contain one or more soluble constituent such as copper, lithium, magnesium, silicon and zinc that individually or in combinations, can form phases that strengthen the alloy. Microstructure development is highly dependent on all of the processing steps the alloy experiences. Ultimately, the macroscopic properties of the alloy depend strongly on the microstructure. Therefore, a quantitative understanding of the microstructural changes that occur during thermal and mechanical processing is fundamental to predict the properties.

Thermal expansion measurements have wide applications in engineering discipline in design and manufacturing. Successful design and manufacturing of systems that are exposed to changing temperatures needs accurate thermal expansion values in addition to their behaviour at elevated temperatures. The work presented here is concerned with the measurement of thermal expansion. The capacitance dilatometry is one of the most sensitive and therefore most common methods to measure these quantities. With this method it is possible to detect relative length changes in micron. That is our hypothesis to use dilatometry to study precipitation kinetics.

The focus of this work is to study the precipitation in Al-Ge-Si, Al-Si, Al-Si-Mg and Al-Zn-Mg alloys. Dilatometry is used to identify the formation and dissolution of phases due to the change in atomic volume. Differential scanning calorimetry (DSC) on the same samples is carried out to

confirm the temperatures of precipitation and dissolution. Chapter 2 describes the state of art of the investigated Aluminium alloys as well as the classification of Al alloys, phase diagrams of Al alloys, DSC, dilatometry tests and precipitation sequence. Chapter 3 gives equation and basic models applied. Chapter 4 describes the methodology as well as equipments. Chapter 5 comprises the results of tests according to structure of methodology. At the end, discussion and conclusions are presented in chapter 6 and 7, respectively.

2 State of art

2.1 Aluminum and aluminium alloys

Aluminum is the most consumed non-ferrous metal in the world, with current annual consumption at 24 million tons (2% of steel). About 75% of this total volume, equivalent to 18 million tons, is “primary aluminium”(that is, aluminium extracted from ore, as opposed to secondary aluminium which is derived from scrap metal processing) [1]. Aluminum alloys are characterized by high stiffness and strength to weight ratio, low specific density, good corrosion resistance, adequate formability, electrical and thermal conductivity, harmlessness for human health, excellent recyclability and moderate to high fracture toughness. In the transportation industry, the constant need to diminish the CO₂ emissions provides an impetus for weight reductions favoring the use of aluminium rather than steel but the higher price limits its market. Still aluminum is ranked among the most important materials of presence and future. Life today can scarcely be imaged without aluminium with its wide range of applications on account of its outstanding properties [2].

It is used in all the essential engineering fields, as transport, buildings and in structural engineering (The main reason for the use of aluminium for buildings and in structural engineering is its good corrosion behaviour. No coating is necessary under most atmospheric conditions), electrical engineering, electronics, machinery, equipment and for packing. Figure 2.1 shows consumption of aluminium and indicates markets for rolled aluminium products [3].

Aluminium constitutes numerous alloys with various elements such as magnesium, manganese, silicon, zinc, copper, iron and lithium. The basic effects of alloying elements on the properties of aluminium have been identified in the early twentieth century leading to the establishment of the system of the commercial aluminium alloys still used today. With varied composition and suitable combinations of heat treatments, and mechanical working, products and semi products of standard and special alloys with a wide range of mechanical, technological, and chemical properties can be produced. The main groups of aluminium alloys which are the most often used in practice along with technically pure aluminium are AlCu, AlMg, AlMgMn, AlMgSi, AlZnMg, and AlZnMgCu alloys [3].

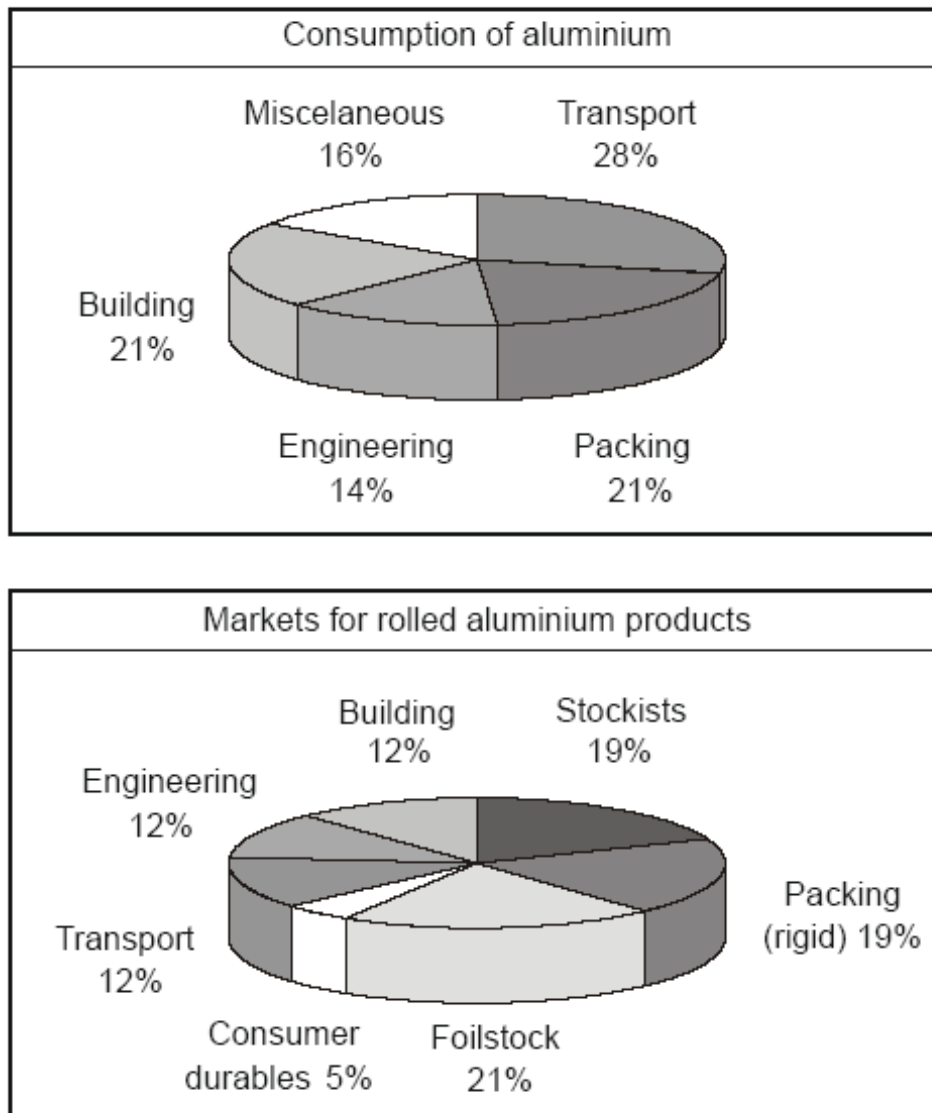


Figure 2.1. Consumption of aluminum in various industrial branches and markets for rolled aluminum products in Europe [3].

2.2.1 Classification of aluminium alloys

Aluminum alloys are divided into two major categories: aluminium casting alloys and aluminium wrought alloys. Aluminum casting alloys are the most versatile of all common foundry alloys and generally have the highest castability ratings. Aluminum casting alloys have the following favorable characteristics: excellent castability, low melting temperature, low gas solubility, high strength to weight ratio, good machinability and high thermal and electrical conductivity. The word "wrought" indicates that certain aluminium alloys are available primarily

in the form of worked products such as sheet, foil, plate, and extruded rods, bars and wires. Aluminium wrought alloys are have been subjected to plastic deformation by a hot or cold working process (such as rolling, extruding, drawing). Aluminium alloys are classified into two main categories, non-heat treatable and heat-treatable alloys. The 1XXX, 3XXX and 5XXX series alloys are non-heat-treatable, and thus are work hardened by cold-working processes, usually by cold rolling. Heat-treatable aluminum alloys contain one or more soluble constituents such as copper, lithium, magnesium, + silicon or +zinc, with decreasing solubility at decreasing temperature, which can form precipitates that strengthen the alloy. The 2XXX, 6XXX, and 7XXX series alloys are heat-treatable.

2.1.2 Designation of wrought Aluminum alloys

The system of designation of the Aluminum Association (AA) in the USA is today the most generally used system and adopted by Europe as well by the acronym AW. It makes use of a 4digit number for the designation of an alloy. The first digit indicates the alloying group [4].

1XXX Series: Aluminum of 99.00% or higher purity, where Si and Fe are the most common impurities. The total amount of impurities must be less than 1%.

2XXX Series: Main alloying element is Cu (1.8-6.8%), Mg (0.2-1.8%), Mn (0.2-1.2%) and Si (0.1-1.3%) is also usually added.

3XXX Series: Main alloying element is Mn (0.3-1.5%). Mg (0.2-1.3%) and Cu (0.05-0.25%) are usually added.

4XXX Series: The major alloying element of this group is silicon.

5XXX Series: Main alloying element is Mg (0.5-5.6%). Mn (0.05-1.1%) and Cr (0.05-0.35%) are usually added.

6XXX Series: Main alloying elements are Mg (0.35-1.4%) and Si (0.2-1.8%). Other common elements are Cu (0.15-1.2%), Mn (0.05-1.1%), Cr (0.04-0.35%) and Fe (0.1-0.3%).

7XXX Series: Main alloying elements are Zn (0.8-8.2%) and Mg (0.8-3.4%), frequently Cu (0.3-2.6%). Other common elements, Cr (0.06-0.35%), Mn (0.05-0.8%), Zr (0.08-0.2%) and Ti (0.01-0.1%) are also usually added.

8XXX Series: This series designations are for miscellaneous types of alloying elements including lithium and some tin.

9XXX Series: Designations are not used and reserved for future use.

The 1xxx, 3xxx and 5xxx series are so called non-heat-treatable alloys; they gain their strength by alloying (solution strengthening e.g. increasing content of Mg) and work hardening. The 2xxx, 6xxx and 7xxx series are heat-treatable alloys, which gain their strength by precipitation hardening as the main mechanism. The 4xxx and 8xxx series of alloys cannot be characterised so easily. All three methods of hardening may be found in these groups depending on the type of alloys [1].

2.1.3 Designation of cast Aluminium alloys

Aluminium Association (AA) in the USA uses a four-digit numerical system to identify aluminium and aluminium alloys in the form of castings and foundry ingot. In Europe, designated AC with 5 digits is introduced maintaining the same heading figures.

1xx.x Series: Aluminium, 99.00% or greater

2xx.x Series: Main alloying element is Copper, but other alloying elements are specified.

3xx.x Series: Main alloying element is silicon, but copper and magnesium as age hardening elements are also usually added.

4xx.x Series: Main alloying element is silicon (without age hardening)

5xx.x Series: Main alloying element is magnesium.

6xx.x Series: Unused series.

7xx.x Series: Main alloying elements are zinc and Mg, but copper and other alloying elements may be specified.

8xx.x Series: Main alloying element is tin.

9xx.x Series: Other element.

2.1.4. Temper designation system [5,6]

A heat treatment and temper designation system has been developed by the Aluminum Association to describe the processing of wrought and cast (heat treatable and non-heat treatable) aluminium alloys except ingots. The basic temper designations are as follows:

F as fabricated. Applies to products of shaping processes in which no special control over thermal conditions or strain hardening is employed. For wrought products, there are the minimum strength values in kp/mm^2 added.

0 annealed (wrought products only). Applies to wrought products, which are fully annealed to obtain the lowest strength condition with high ductility.

H strain hardened by cold work (wrought products only). Applies to products which have their strength increased by strain hardening with or without thermal treatments to produce some reduction in strength. Two or more digits in non-heat treatable alloys always follow the H.

T Heat treated to a stable condition, excluding annealing [7].

Applies to products which are thermally treated with or without strain hardening, to produce stable tempers. In heat treatable alloys one or more digits always follow T:

T1 Cooled unspecified from an elevated temperature forming process (partial solution) followed by natural ageing.

T2 Cooled unspecified from an elevated temperature forming process, cold worked and naturally aged.

T3 Solution heat treated, quenched, cold worked and naturally aged.

T4 solution heat-treated, quenched and naturally aged to a substantially stable condition. Applies to products that are not cold worked after solution heat- treatment.

T5 Cooled from elevated forming temperature (T1) and then artificially aged.

T6 solution heat-treated, quenched (T4) and then artificially aged. Applies to products, which are not cold worked after solution heat-treatment.

T7 Solution heat treated, quenched and overaged.

T8 Solution heat treated, quenched, cold worked and then artificially aged (amount of cold work in % indicated by subsequent digit).

T9 Solution heat treated, quenched, artificially aged and then cold worked.

T10 Cooled from an elevated temperature forming process, cold worked and then artificially aged.

W Unstable temper applied for alloys that age spontaneously at room temperature after solution heat treatment. Only specific if followed by the time of natural aging which distinguish the condition from T4.

2.2 Strengthening Mechanisms

The main objective in the design of aluminum alloys is to increase strength, ductility and resistance to wear, creep and fatigue. Effects on these properties are specific to different combinations of alloying elements, thermomechanical history, heat treatment or cold working process [9].

2.2.1 Heat treatment of Aluminum alloy

Pure aluminium itself is a metal with relatively low strength. Aluminium in its purest form has a tensile strength of around 40 N/mm² and a proof strength of about 10 N/mm² at room temperature*. For most technical applications this is too low. Alloying and Controlled heat treatment can significantly influence properties such as strength, ductility, fracture toughness, thermal stability, residual stresses, dimensional stability, and resistance to corrosion and stress corrosion cracking. The main heat treatment procedures are homogenization, annealing, and precipitation hardening involving solution heat treatment, quenching, and ageing [5].

Wrought aluminium alloys that obtain their strength through a combination of precipitation and solid solution are called heat treatable. Heat-treatable alloys are strengthened by solution heat treatment and controlled aging, and include the 2XXX, some 4XXX, 6XXX, and 7XXX series alloys. The other alloys obtain their strength through cold deformation and are classified as non-heat treatable or also as work hardening alloys. Non-heat-treatable alloys are those that derive strength from solid solution or dispersion hardening and are further strengthened by strain hardening. They include the 1XXX, 3XXX, 4XXX, and 5XXX series alloys. Elements in solid solution influence the work hardening for example by decreasing the mobility of dislocations, that makes them a more effective barrier which increases the strength even further [8].

2.2.2 Stages of Age Harding Treatment

Such heat treatments usually include 3 main stages, named solution heat treatment, quenching and ageing. These stages are described below considering the Al-Cu phase diagram.

2.2.2.1 Solution Heat Treatment

Consider for instance Al-Cu phase diagram in figure 2-2. If an alloy with composition 4wt%Cu is heated above the solubility line, to a temperature T_1 , the θ -phase will dissolve and Cu uniformly disperse into the homogeneous solid α solution (matrix). Upon slow cooling, the θ -phase would nucleate below the solubility line and grow to form an equilibrium $\alpha+\theta$ structure.

* The fcc structure with high stacking fault energy is characterized by an atomic volume of $16.59 \cdot 10^{-3} \text{ (nm)}^3$

However, if the alloy with 4wt%Cu is heated to temperature, T_1 , and subsequently quenched in water, the dispersed Cu atoms are trapped in the α -solution. The solution α -phase is said to be supersaturated, because it contains more Cu at room temperature than the solubility limit. This process is called solution quenching treatment. Therefore solution heat treatment is done at a higher temperature within the single-phase region, so as to dissolve the alloying elements.

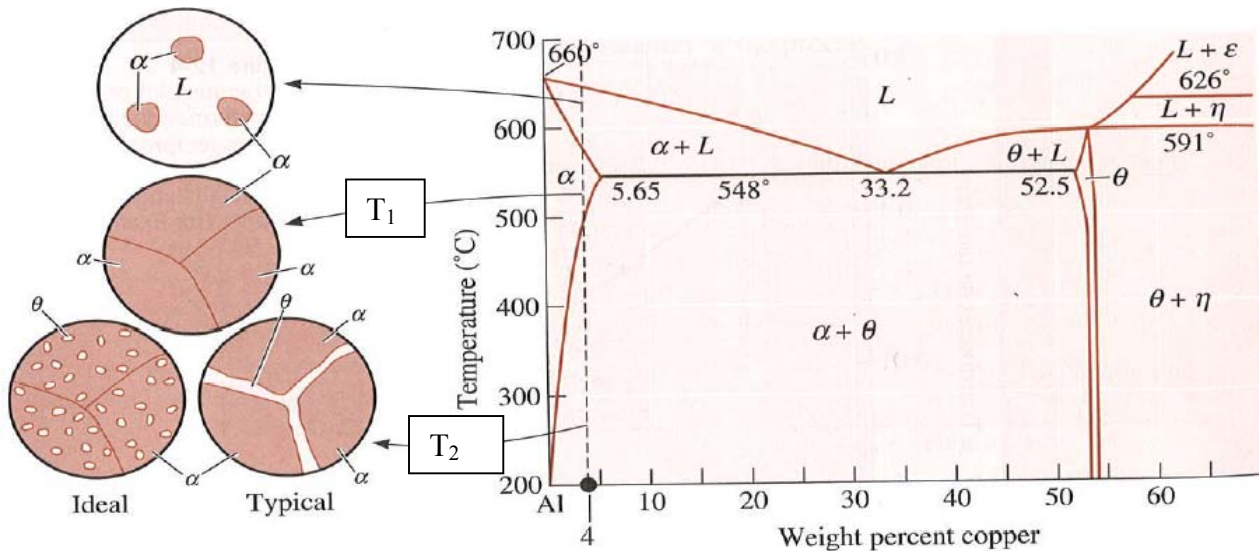


Figure 2.2 The Aluminium –Copper phase diagram and the microstructure that may develop during cooling of an Al-4% Cu alloy [10].

2.2.2.2 Quenching

Quenching is done to form a supersaturated solid solution (SSSS) of Cu in α , and effectively 'freezes in' the non-equilibrium α – phase structure. Quenching also 'traps' a large amount of vacancies that are created as a result of high temperatures, which reduces the time for diffusion. Equilibrium vacancy concentration increases exponentially with temperature so that when the alloy is quenched, a super-saturation of vacancies is also frozen into the structure. This has very important implications during any subsequent ageing process.

2.2.2.3. Ageing

The main requirement for an alloy system to respond to age hardening is a significant decrease in solid solubility of one or more of the alloying elements with decreasing temperature. Ageing is the controlled decomposition of the supersaturated solid solution to form finely dispersed precipitates in heat-treatable alloys. The SSSS is very unstable and if, left alone, the excess Cu will precipitate within the α -phase. This can occur at any temperature below the solvus, even at room temperature. Upon ageing, a SSSS will tend to transform towards the equilibrium structure. However, before equilibrium is attained, a number of intermediate stages (phases) typically

occurs [11]. During ageing, precipitation of different phases other than θ (see Figure 2-3) occurs, the so-called metastable phases. These are the precipitates that lead to the large strengthening effects termed precipitation hardening. All the precipitate transformations taking place in the alloy from the SSSS until the equilibrium condition is reached are referred to as the precipitation sequence. A typical decomposition sequence is presented in Figure 2-4.

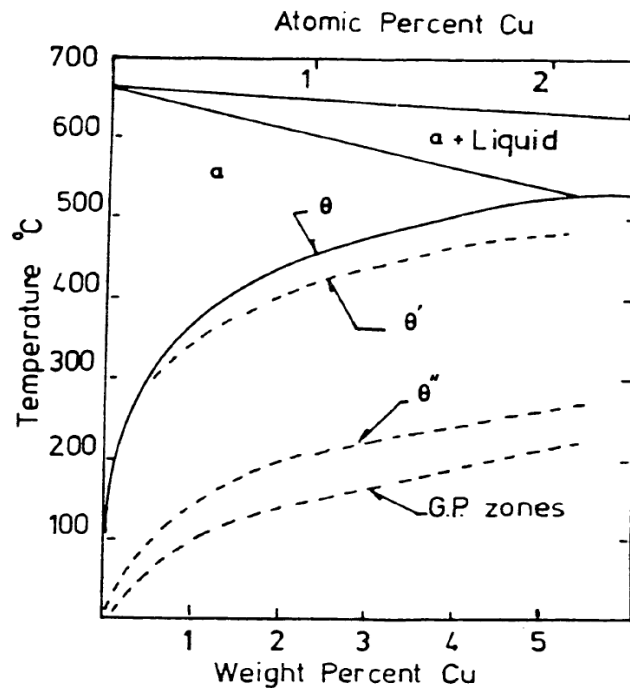
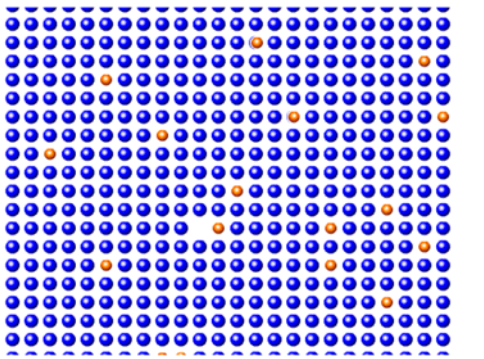
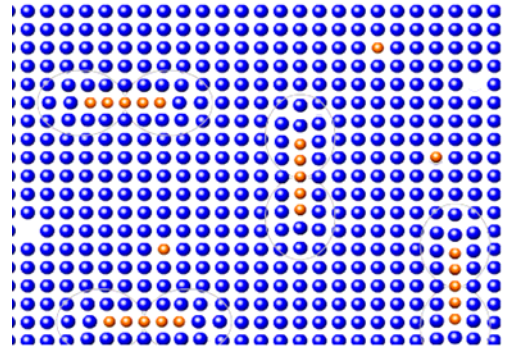


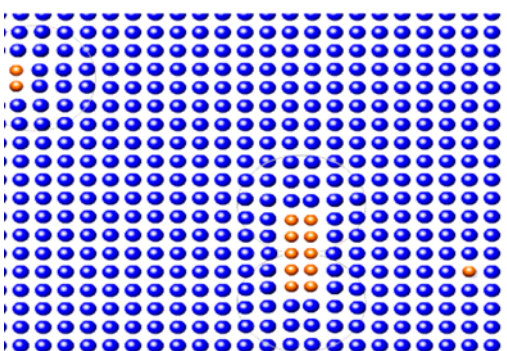
Figure 2-3 Phase diagram illustrating the formation of metastable and stable precipitates in a Al-Cu alloy. Broken lines indicate the limits of metastable precipitate phases [11].



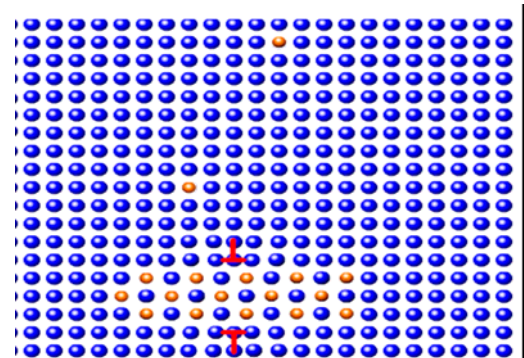
SSSS of B in A, having been formed by quenching from the solution treatment temperature. Note also the presence of vacancies, which have been ‘frozen in’ during the quench.



GP zones: Diffusion during ageing results in localized concentrations of B atoms on specific planes of the A lattice. These are known as GP (Guinier-Preston) zones. In some systems GP zones are disk shaped, while in others they can be rods, needles or spheres.

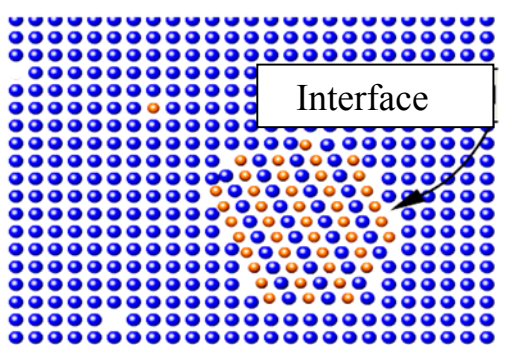


Intermediate Stage 2: When GP zones became unstable a coherent intermediate phase nucleates. The A atoms around this plane must then distort even further to accommodate the new phase leading to coherency strain.



Intermediate stage 3:

As precipitates become larger, some of the coherency strain may be relieved by the formation of dislocations at the interface. Such precipitates are known as ‘semi-coherent’



Equilibrium Phase: Is formed after sufficient ageing. This has a different crystal structure from the matrix (‘A’ atoms) and is normally incoherent with it. There is however a new phase boundary between the matrix and the precipitate.



Figure 2-4 A general model for the decomposition of a SSSS [11] of B in A.

2.3 Precipitation Hardening Alloys

The effect of precipitation hardening was first discovered in the Al-Cu system and used practically by Wilm in 1906. The effect is caused by the fact, that one or more suitable elements are able to form particles, so called intermetallic compounds, with each other or together with the matrix material aluminium. They also constitute lattice imperfections and depending on the size of these particles and their uniform distribution they cause a remarkable increase in strength. The whole process begins with a solution heat-treatment i.e. all alloying elements are in solution (solid solution), after that a quenching is necessary to also get a uniform distribution of all elements and super saturation of vacancy at ambient temperature. After that, the elements involved begin to move in the aluminium matrix, they unify to intermetallic compounds and grow. This happens at room temperature (natural ageing) but more efficiency at elevated temperatures (artificial ageing) [12]. Precipitation hardening can be applied only to those groups of alloys, which are heat treatable (i.e. 2000, 6000 and 7000 wrought series).

An aluminium alloy that responds to precipitation hardening must contain certain of soluble alloying elements that exceed the solid solubility limit at room temperature. The precipitated phases must have a structure different from the solid solution. Careful control of this precipitation reaction is essential, otherwise the hardening constituents and the interparticle distance will become too large and contribute little to the strengthening [13].

2.3.1. Precipitation Sequence in 2xxx series

An Al-Cu binary alloy is one of the most famous age hardenable alloys. Copper is soluble to a certain extent in solid aluminum and its solid solubility decreases with decreasing temperature. The solubility of copper in aluminum usually is reported as 0.25 to 0.30Wt % at room temperature theoretical consideration however point to a lower value 0.08 to 0.12 %. According to Al-Cu binary phase diagram a eutectic is formed at 33Wt% copper between Al and Al₂Cu which is the first phase in the aluminum rich regions (figure 2.5) [20]. The atomic volume of Cu with fcc Cu is $11.80 \cdot 10^{-3} \text{ (nm)}^3$ /atom, 28.8% smaller than that of Al.

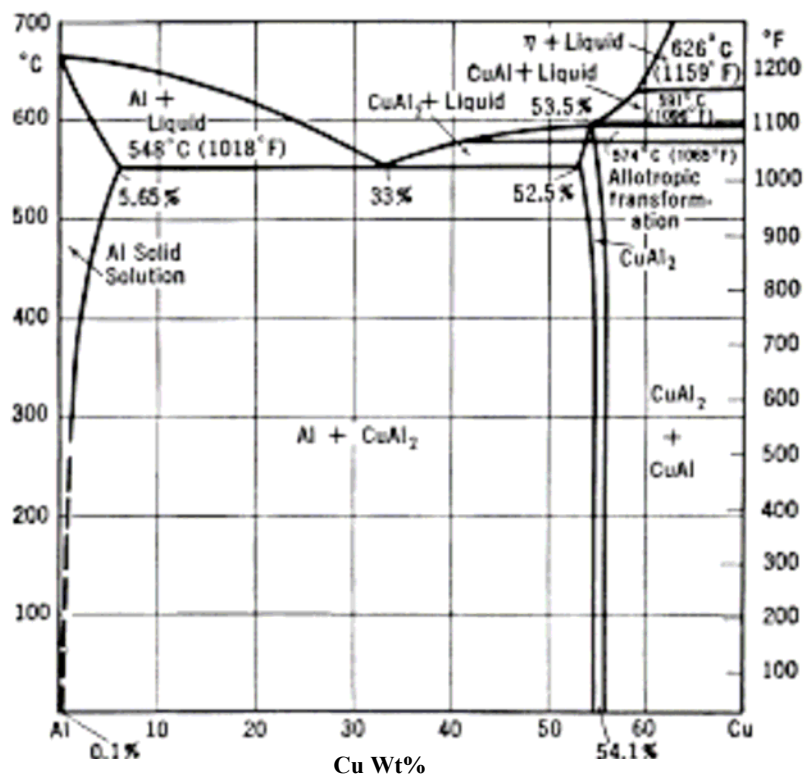


Figure 2-5 system Al-Cu aluminium end of the equilibrium diagram [20].

Precipitation sequence of the alloy described in table 2.1 is known as

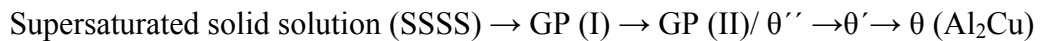


Table 2.1 Precipitation sequence in Al-Cu alloys during ageing [21]

Phase	Composition	Lattice parameter (nm)	Unit cell structure
GPI	Al_9Cu , Al_7Cu , Al_5Cu , Al_3Cu	—————	fcc
GPII (θ'')	(Al_3Cu)	θ'' plates of a few atomic layers, (1 nm)	fcc
θ'	(Al_2Cu)	$a=0.404$ nm, $c=0.58$ nm	tetragonal structure
θ	(Al_2Cu) vol /atom= $0.015\text{nm}^3/\text{atom}$ =90 % of vol /atom of Al	$a=0.607\text{nm}$ and $c=0.487\text{nm}$	Tetragonal structure (12atom/unit cell) [19].

The structure of these phases is shown in figure 2.6.

a) Guinier–Preston (GP) zones form in many alloys in the early stages of phase separation during the decomposition of supersaturated solid solutions. They have different morphologies (platelets, spheres, needles) depending on the difference in atomic diameters of solute and solvent elements [14]. GP zones in Al–Cu alloys still attract much interest and definitive conclusions on their structure, formation and evolution have not yet been reached [14,15,16,17]. At present it is widely believed that GP zones become discs of Cu atoms, of 4–20 nm in diameter, on

substitutional sites on $\{100\}$ planes in the fcc Al lattice. Because of the distinctly smaller size of Cu atoms ($V_{\text{at Al}} = 16.59 \cdot 10^{-3} \text{ nm}^3/\text{atom}$ and $V_{\text{at Cu}} = 11.80 \cdot 10^{-3} \text{ nm}^3/\text{atom}$) the matrix planes surrounding GP zones collapse towards the Cu layers [18].

b) θ'' (Fig. 2.6(b)) phase with formal stoichiometry CuAl_3 , consists of layers (discs) of Cu atoms in substitutional sites on $\{100\}$ planes of the fcc Al lattice separated by three planes of Al atoms in a sequential stacking $\{\text{CuAlAlAl}\}$ [18]

c) θ' phase (Fig. 2.6(c)) is a tetragonal distortion of the fluorite structure with axes aligned along those of the host lattice and is incoherent with it along the θ' phase c -axis

d) θ phase (Fig. 2.6(d)), the ultimately stable structure, is a more elaborate distortion of the fluorite structure, and is wholly incoherent with the host lattice. The structure is tetragonal, with one distinguishable Cu and Al atom per unit cell [18].

Addition of some trace elements to the binary alloy changes the morphology of precipitates. Small amount of Mg addition results in finely dispersed θ' phase and produces the needle like meta stable S' and stable S (Al_2CuMg) phase.

Supersaturated solid solution (SSSS) \rightarrow GP zones $\rightarrow S'' \rightarrow S' \rightarrow S$ (Al_2CuMg)

Where SSSS and GP zones are as defined previously, S'' and S' are the transition precursors to equilibrium S (Al_2CuMg)

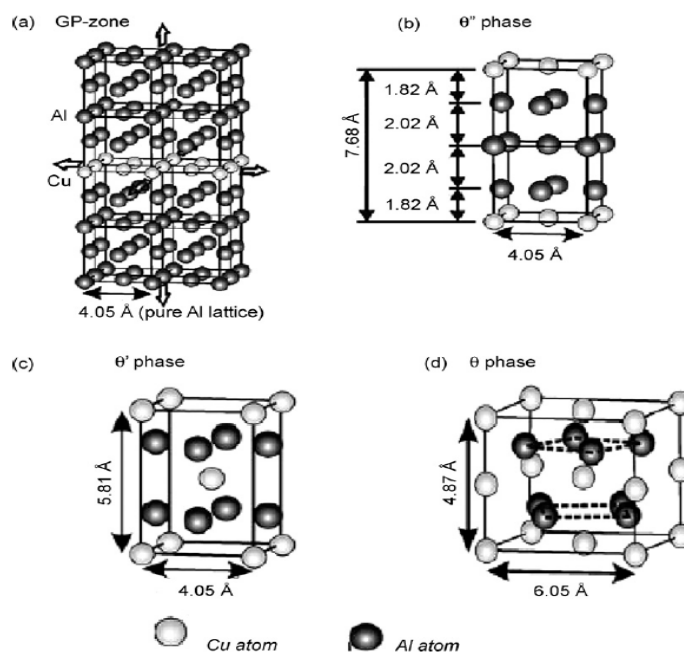


Figure 2-6 The crystal structures of the (a) GP zones on $\{111\}$, (b) θ'' phase, (c) θ' phase and (d) θ phase [17], all look $\parallel \{100\}$ -

The precipitation sequences for the Al-Cu-Mg systems and their equilibrium precipitates together with their lattice parameter are summarized in Table 2.2

Table 2.2 Precipitation Phases in Al-Cu –Mg alloys [21]

Phase	Compound	Lattice parameter (nm)	Unit cell structure
GPB	GPB zone to be a short-range ordering of Cu and Mg solute atoms.	-----	fcc
S''	$\text{Al}_5(\text{Cu,Mg})_3$	$a = 0.405 \text{ nm}, b = 1.62 \text{ nm}$ and $c = 0.405 \text{ nm}$	orthorhombic structure
S'	(CuMgAl_2)	$a = 0.404 \text{ nm}, b = 0.925 \text{ nm}, c = 0.718 \text{ nm}$	orthorhombic structure
S	(CuMgAl_2) vol/atom=0.016nm ³ /atom the same as Al	$a = 0.400 \text{ nm}, b = 0.923 \text{ nm}, c = 0.714 \text{ nm}$	orthorhombic structure (16 atom/unit cell)

2.3.2. Precipitation Sequence in 5xxx series

Magnesium is the major constituent in the aluminium magnesium group of alloys, which achieve high strength with good ductility through cold work together with excellent corrosion resistance and weldability. The phase diagram of Al-Mg (figure 2.7) alloy shows an eutectic liquid→Al+Mg₅Al₈ at 33Wt%Mg 450°C. Mg₅Al₈ is very brittle below 327°C, but shows some plasticity at higher temperature [20]. Most work on the precipitation in Al-Mg indicates the following precipitation sequence

Supersaturated solid solution (SSSS) → GP zones → β'' → β' → β [36].

The precipitation sequences for the Al-Mg systems and their equilibrium precipitates together with their lattice parameter are summarized in table 2.3.

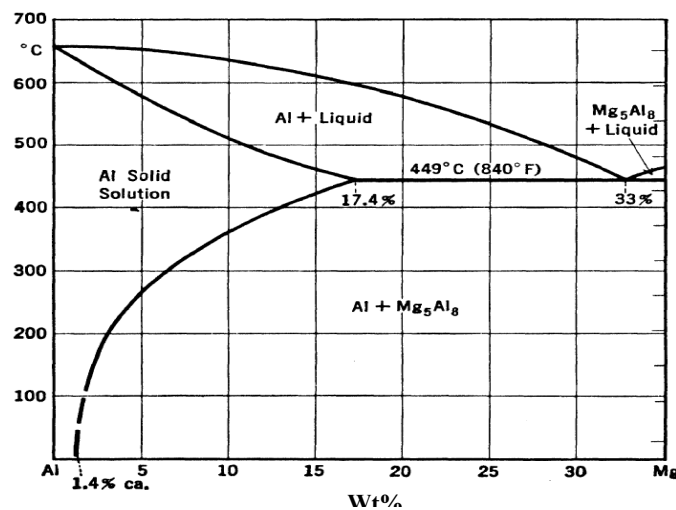


Figure 2-7 Aluminium end of the Al-Mg equilibrium diagram. Showing the solid solubility of magnesium in aluminium [20].

Table 2.3 Precipitation Phases in Al–Mg alloys.[39]

Phase	Compound	Lattice parameter (nm)	Unit cell structure
GP Zones	Clusters with higher Mg content than the surrounding matrix	-----	Plate-shaped clusters fcc
β''	Al_3Mg	-----	L_2 structure. ordered phase approximately spherical coherent
β'	Al_3Mg_2	$a = 1.002$ and $c = 1.636$	Semi coherent hexagonal
β	$\text{Al}_8\text{Mg}_5 (\text{Al}_3\text{Mg}_2)$ 0.019-0.02nm ³ /atom 1.14-1.2 vol./atom of Al	$a = 2.82$ -2.86	Complex FCC structure

Assuming that the unit cell of Al_8Mg_5 contains 1166-1172 atoms [53]. Volume of 0.019 to 0.02 nm³/atom i.e. 14-20% bigger than that Al.

2.3.3. Precipitation Sequence in 6xxx series

Silicon is the second most abundant impurity of aluminium, originating from the silica or the silicates in the bauxite. It is also one of the most common additions to aluminium alloys to which it imparts fluidity in casting and welding and high mechanical properties through the formation of Mg_2Si compounds that make the alloys heat treatable. The quasi-binary Al- Mg_2Si system is a simple eutectic one in which the two phases in equilibrium are Al and Mg_2Si [53].

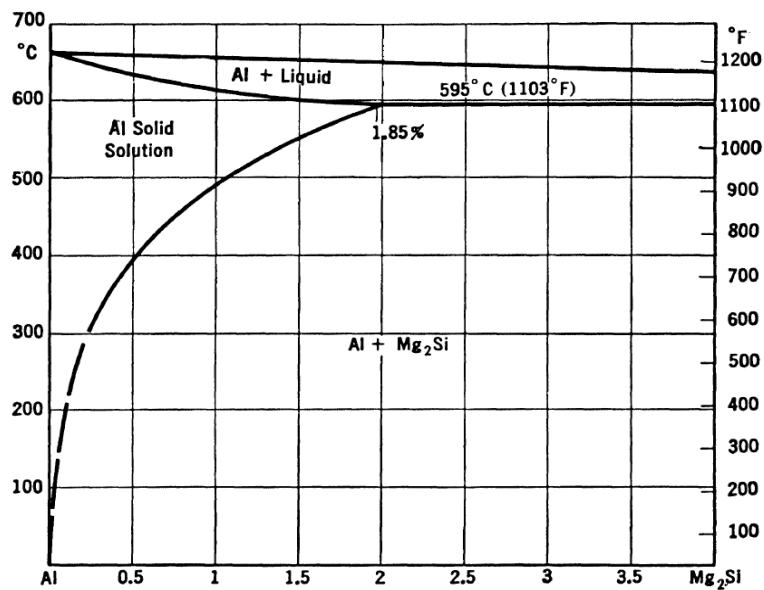


Figure 2.8 System Al-Mg-Si, quasi-binary section Al-Mg₂Si, showing the solid solubility of Mg₂Si in aluminium [53].

The aluminium-magnesium-silicon system is the basis for a major class of heat treatable alloys used for both wrought and cast products. Aluminium-silicon alloys that do not contain copper additions are used when good corrosion resistance is needed. Magnesium and silicon can form the intermetallic-hardening phase Mg_2Si which precipitates in the α aluminium matrix (see figure 2.9) and increases the yield strength [22]. Addition of Cu to the 6XXX series alloys improves mechanical properties due to finer matrix precipitation of the β' -phase [23] and it was found by Edwards, Perovic and Cayron [24] that Cu may also be incorporated in this phase. Copper can act as a substitute for magnesium. Precipitation sequences in Al-Mg-Si alloys and structure of the phases with and without additional Cu or Si are listed in table 2.4 and 2.5 respectively.

For Al-Cu-Mg-Si alloys, a model of structural phase transitions was proposed by Cayron [24] to explain the common substructure of the Q, QC and QP phases.

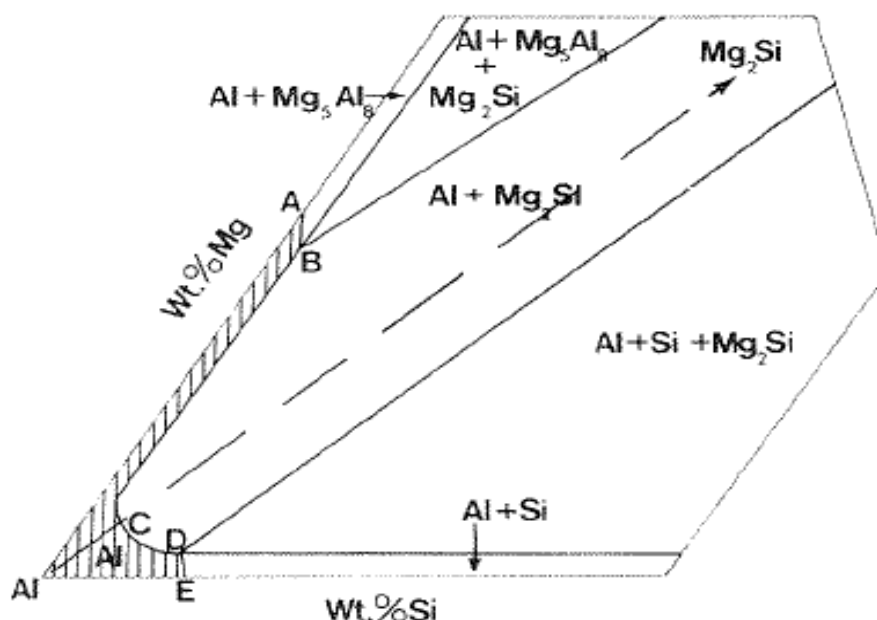


Figure 2-9 Aluminium corner of the aluminium –magnesium- silicon phase diagram distribution in solid state at 549-577°C [20].

Table 2.4 precipitation sequence in Al-Mg-Si alloys [25]

Phase	Compound	Lattice parameter (nm)	Unit cell structure
GP-I	$Mg_xAl_{5-x}Si_6$	$a=1.48, b=0.405, c=0.648,$ $\beta=105.3 \text{ deg}$	Monoclinic
GP-II (β'')	Mg_5Si_6	$a=1.516, b=0.405, c=0.674,$ $\beta=105.3 \text{ deg}$	Monoclinic
β'	$Mg_{1.8}Si$	$a=b=0.715, c=0.405, \gamma=120 \text{ deg}$	Hexagonal
β	Mg_2Si Vol./atom=0.021-0.022nm ³ /atom =1.27-1.33 of vol /atom of Al	$a=0.635-0.640$	fcc (12 atoms /unit cell) [19]
β' (typeC)	$MgSi_{>1}$	$a=b=1.03, c=0.405, \gamma=120 \text{ deg}$	Hexagonal
U1(type A)	$MgAl_2Si_2$ Si:Al:Mg=5:4:1	$a=b=0.405, c=0.674, \gamma=120 \text{ deg}$	Hexagonal
U2(type B)	$MgAlSi$ Si:Al:Mg=5:4:2	$a=0.675, b=0.405, c=0.794$	Orthorhombic
Si	Si Vol./atom=0.021nm ³ /atom =1.27 of vol./atom of Al	$a=0.639$	Cubic (diamond type)
Si	Vol./atom=0.0152 nm ³ /atom = -8.4% vol./atom of Al	0.393 [55]	fcc
Mg	Vol./atom=0.023nm ³ /atom =1.39 vol./atom of Al	$r=0.172$ [118]	Hexagonal

Table 2.5 Precipitation sequences in 6XXX-series alloys with addition Cu or excess Si [26]

Alloys	Phase	Mg/Si(at%)	Lattice parameter (nm)	Unit cell structure
Al-Mg-Si	β''	1.0-1.7	$a=0.152, b=0.405, c=0.67,$ $\gamma=120 \text{ deg}$	Monoclinic
	β'	1.7	$a=0.705, c=0.405$	HCP
	β	Mg_2Si	$a=0.642$	FCC
Al-Cu-Mg-Si	QP		$a=0.393, c=0.405$	HCP
	QC	1.4	$a=0.670, c=0.405$	HCP
	Q	$Cu_2Mg_8Si_6Al_5$	$a=1.04, c=0.405$	HCP
Al-Mg-Si	TypeA	0.28	$a=0.405, c=0.670$	HCP
	TypeB	0.40	$a=0.67, b=0.79, c=0.405$	Orthorhombic
	TypeC	0.83	$a=1.04, c=0.405$	HCP

The identification and interpretation of the DSC peaks and valleys based on literature are given table 2.6.

2.3.4. Precipitation Sequence in 7xxx series

The aluminium alloy 7000 series can be divided into two main groups, medium strength weldable (Al-Zn-Mg) and high strength non-weldable (Al-Zn-Mg-Cu). The first group has

very little or no Cu [27]. The addition of Cu to Al-Zn-Mg alloys progressively reduces their weldability. In quaternary Al-Zn-Mg-Cu alloys, the phases $MgZn_2$ and $AlMgCu$ form an isomorphous series with Al and Cu substituting for Zn in $MgZn_2$ [28]. Part of the Zn in the precipitates may be replaced by Cu and/or Al, so that their actual composition is closer to $Mg(Zn,Cu,Al)_2$ [26].

Table 2.6 Temperatures of DSC peaks corresponding to different phase transformations in AlMgSi alloys

Phase transformation	Temperature
GP zones precipitation	160°C [97,98,101,102]
GP zones dissolution	200-220°C [85,97,102,,99]
β'' precipitation	260°C [98,100,101,102,104,105]
β'' dissolution	265°C [97,99]
β' precipitation	290-310°C [37,99,100,105]
β' dissolution	380-420°C [101,102,103,104]
Si 1 st precipitation peak	200-270°C [85,99,101,105]
Si 2 nd precipitation peak	270°C
Si 2 nd precipitation peak	450°C
Si dissolution	520°C [99]
Mg_2Si precipitation	460-470°C [37,85,100,103,105]
Mg_2Si dissolution	500-510°C [99,103,105]

In commercial Al-Zn-Mg-Cu alloys, several intermetallic phases between 400 °C and the solidus can occur during solidification, which are called S, T and η . It is noted that S, T and η are intermetallics with extended composition ranges [30]. It is well known that type and intrinsic character of coarse particles will differ in different alloys or in one alloy at differently solidified and homogenized conditions. For instance, in the as cast 7055 alloy, three kinds of highly mixed particles as T-(AlCuZn)₄₉Mg₃₂, η - (AlCuZn)₂₋₃Mg and S-Al₂CuMg were identified. After the isothermal treatment at 455 °C, the Al-rich η phase tends to disappear [29]. Figures 2.10, 2.11 show phase diagrams of Al-Zn-Mg alloys with phase distribution in solid. Precipitation sequences in this alloys are listed in table 2.7.

Table 2.7 Precipitation sequences in Al-Zn-Mg alloys [31]

Phase	Compound	Lattice parameter (nm)	Unit cell structure
GP Zone		$a=b=0.497, c=0.554,$ $\gamma=120^\circ$	Monoclinic
η'		$a=0.496, c=0.868$	Hexagonal
η	$MgZn_2$ Vol/atom=0.0487nm ³ /atom =3 x vol /atom of Al	$a=0.515-0.522$ $c=0.849-0.856$	Hexagonal

2.4.1 Al-Si system

As shown in figure 2.12 Si solubility decreases from 1.65 wt% at the eutectic temperature to less than 0.01 wt% at room temperature. Quenched in supersaturated Si precipitates in diamond structure. Table 2.8 shows difference between atomic volume of Si in Al fcc and atomic volume of Si in diamond structure.

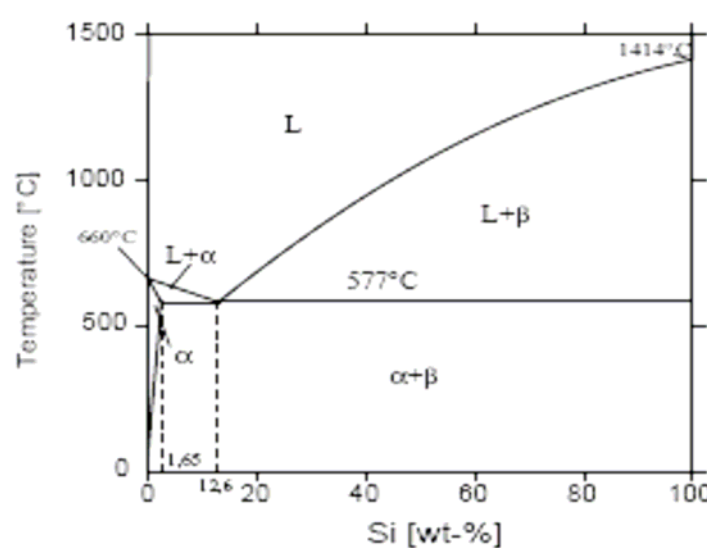


Figure 2-12. Equilibrium diagram of Al-Si system [20].

2.4.2 Al-Ge system

As shown in Al-Ge phase diagram (see figure 4.1 in chapter 4) and table 4.1 Ge solubility decreases from 5.2 wt% at eutectic temperature to less than 0.11 wt% at room temperature. Quenched in supersaturated Ge precipitates in diamond structure. Table 2.8 shows difference between atomic volume of Ge in Al fcc and atomic volume of Ge in diamond structure.

Table 2.8 Crystallographic data of fcc Al-base solid solutions and diamond cubic structure [55]

	Covalent (dc)			Metallic (fcc)			
	a (nm)	b (nm)	$V10^{-3} \text{ (nm)}^3$	a (nm)	b (nm)	$V10^{-3} \text{ (nm)}^3$	$(V_{dc}-V_{fcc})/V_{Al}$
Al	-----	-----	-----	0.405	0.286	16.59	-----
Si	0.542	0.235	19.87	0.393	0.278	15.16	28%
Ge	0.565	0.245	22.5	0.415	0.292	17.55	30%

a: lattice parameters b: smallest atomic distance, V: volume per atom

2.5 Thermal analysis methods [114,115,116,117]

2.5.1 Definition:

Thermal analysis refers to a variety of techniques in which a physical property of a sample is continuously measured as a function of temperature, while the sample is subjected to a pre-determined temperature profile.

Thermal analysis techniques are used in virtually every area of modern science and technology. The basic information that these techniques provide, such as crystallinity, specific heat and expansion, are important for materials research and for development of new products. Thermal analysis techniques also find their increasing use in the area of quality control and assurance, where demanding requirements must be met in the increasingly competitive world.

• Major Techniques:

- Thermal Gravimetric Analysis (TGA)
 - a. Differential Thermal Analysis (DTA)
 - b. Isothermal Calorimetry
- Differential Scanning Calorimetry (DSC)
- Dynamic Mechanical Analysis (DMA)
- c. Thermo-mechanical Analysis (TMA)
- d. Dilatometry (DL)

In this work we used DSC and DL (TMA equipment can be used as DL)

2.5.2 Differential scanning calorimetry (DSC)

Differential scanning calorimetry (DSC) is a technique for measuring the energy necessary to establish a nearly zero temperature difference between a substance and an inert reference material, as the two specimens are subjected to identical temperature regimes in an environment heated or cooled at a controlled rate. By means of DSC, exothermic and endothermic reactions of phase transformation can be detected.

There are two types of DSC systems in common use (Fig. 2.12). Power-compensation DSC and heat flux DSC. In power-compensation DSC the temperatures of the sample and the reference are controlled independently using separate, identical furnaces. The temperatures of the sample and reference are made identical by varying the power input to the two furnaces; the energy required to do this is a measure of the enthalpy or heat capacity changes in the sample relative to the reference. In heat flux DSC, the sample and reference are connected by a low resistance heat flow path (a metal disc). The assembly is enclosed in a single furnace. Enthalpy or heat capacity changes in the sample cause a difference in its temperature relative to the reference. The temperature difference is recorded and related to enthalpy change in the sample. The basic principle underlying this technique is that, when the sample undergoes a physical transformation such as phase transitions, more (or less) heat will be needed to flow to the reference to maintain both at the same temperature. Whether more or less heat must flow to the sample depends on whether the process is exothermic or endothermic. Differential scanning calorimetry can be used to measure a number of characteristic parameters of a sample. Using this technique it is possible to observe fusion, phase transformations, crystallization events, reaction kinetics [33].

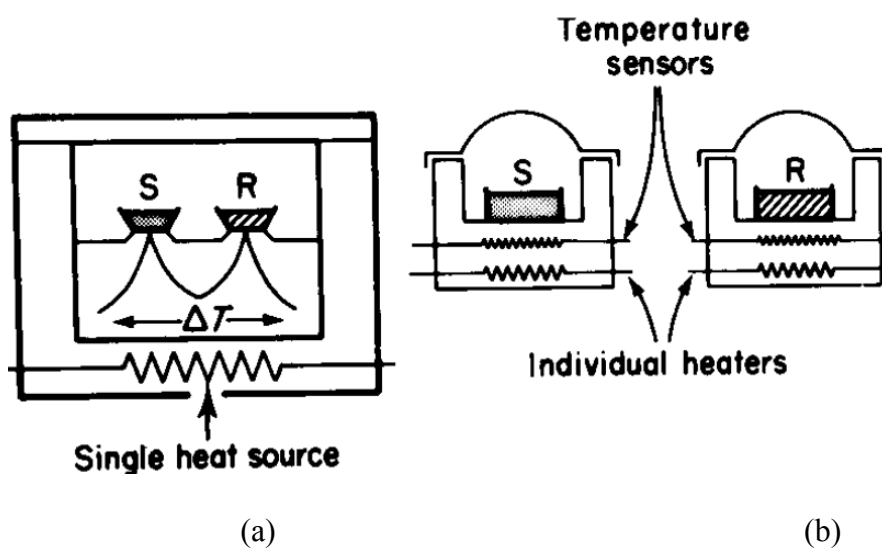


Figure 2-12 (a) Heat flux DSC; (b) power compensation DSC [33].

2.5.3 Differential scanning calorimetry (DSC) thermograms of some Al alloys.

Figure 2.13 shows a DSC thermogram of Al-Cu-Mg-Mn alloy. Peak I refers to formation of clusters, peak II is dissolution of clusters and GPB2/S'', peak III is formation of S precipitate (formation of S phase occurs at temperatures higher than 190°C, where clusters form and peak IV refers to dissolution of S precipitates [34]. Figure 2.14 shows the DSC thermogram of the AW2324 alloy in three different conditions [21]. Five main effects may be identified in these thermograms. Peak A is due to the formation of co-clusters, an endothermic effect B may be attributed to Cu-Mg co-cluster dissolution (with possibly some GPB2 dissolution), an exothermic effect C (containing two overlapping reactions) is attributed to the formation of S phase precipitates, a broad endothermic effect, D, is identified as progressive dissolution of the S precipitates, an endothermic sharp peak, E, is believed to be due to the (partial) melting of S+θ eutectics.

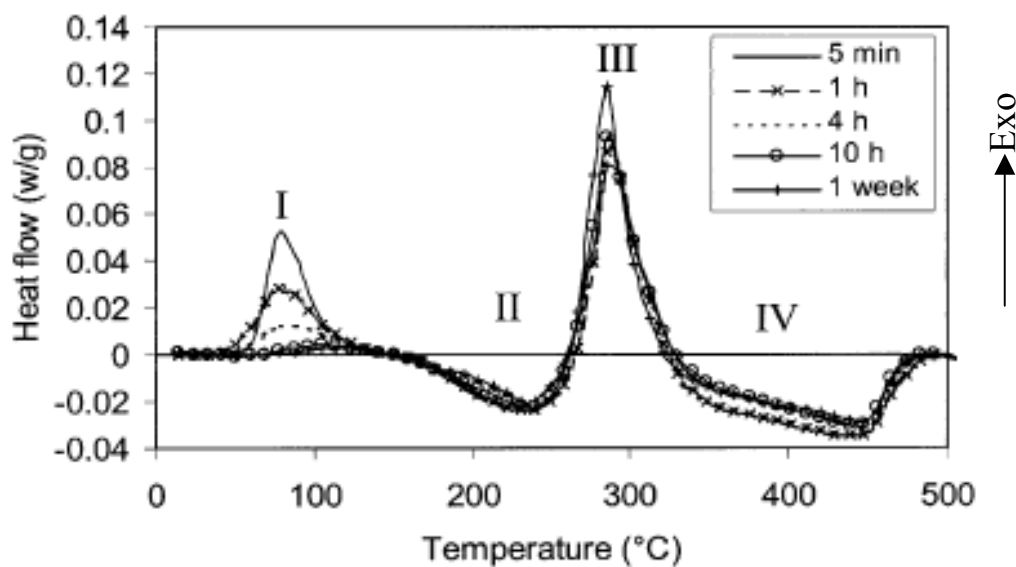


Figure 2.13 DSC thermograms of solution treated and quenched Al-2.81Cu-1.05Mg-0.41Mn (wt%) alloy after aging for several intervals at 25°C [34].

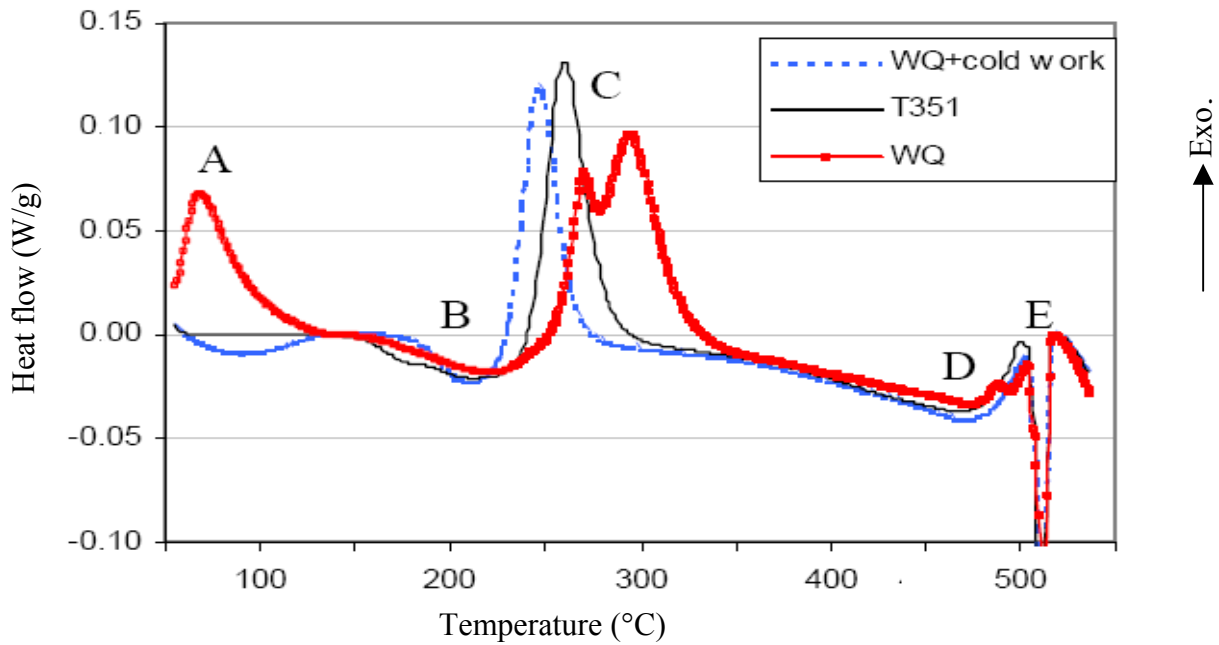


Figure 2.14 DSC thermogram of the AW2324 alloy in T351*, WQ and WQ+ cold worked conditions [21].

Figure 2.15 shows DSC thermogram of Al-Mg samples, which are aged at room temperature for 2 years. The composition of samples are given in table 2.9

In the DSC thermograms presented in these alloys, generally only events B (dissolution of GP zones and β''), C (formation of β') and F (dissolution of β' and β) can be observed clearly. In the second half of event C some evidence of event E (transformation $\beta' \rightarrow \beta$) can be observed for some

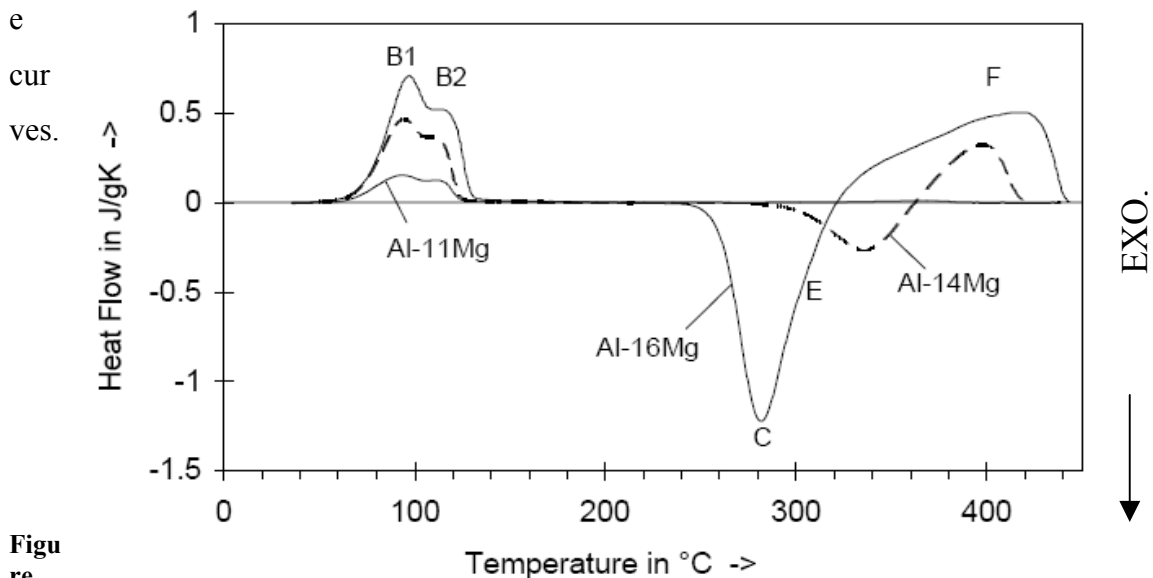


Figure 2.15 DSC thermograms of the Al-11Mg, the Al-14Mg and the Al-16Mg alloy aged at room temperature for 2 years. Heating rate is 20 °C/min [36].

*T351 Solution treated at 495°C, quenched, stretched 1.5-3%, and aged at room temperature for several months

Table 2.9 Composition of the Al-Mg alloys

Alloy	Mg (at%)	Mg (wt%)	Al
Al-11Mg	11.1	10.1	balance
Al-14Mg	13.7	12.5	balance
Al-16Mg	15.8	14.5	balance

DSC thermograms of AW6005 are shown in figure 2.16. A total of seven enthalpic signals are identified in the DSC thermogram: The small exothermic peak centering around 80°C (effect 1) is best accounted for by low temperature clustering activities. There appears to be another weak exothermic signal between 122 and 212°C (effect 2) which, in 6XXX alloys in this temperature range, implies formation of GP-I zones. The very small endothermic signal at approximately 215°C (effect 3) is produced by the dissolution of the few clusters which have formed below 120°C. The major exothermic peak which follows right after and lasts until 275°C (effect 4) is clearly linked with the precipitation of β'' . The neighbouring exothermic peak between approximately 275 and 340°C (effect 5) is produced by the transformation of β'' to β' . The last two peaks are exothermic and endothermic (effects 6 and 7) and are associated with the precipitation and dissolution of the equilibrium Mg_2Si phase, respectively [106,107,108].

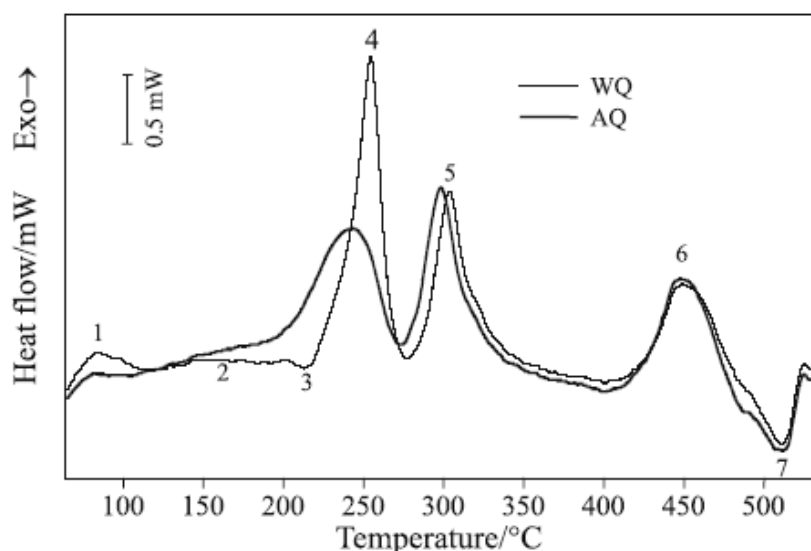


Figure 2.16 DSC thermogram of AW6005 disc samples quenched in water (WQ) and in air (AQ) after the solution treatment [106].

Figure 2.17 shows the DSC thermogram of Al-Zn-Mg alloy. The first endothermic peak (A) can be attributed to the reversion of GP zones formed during natural ageing [109,110]. When the

temperature reaches approximately 120°C, η' precipitate, which results in the exothermic peak (B) in the thermogram. At higher temperatures we can observe two other exothermic peaks (C and D), the first corresponding to the $\eta' \rightarrow \eta$ transformation, and the second probably to the precipitation of T phase, the alloy being in the (Al + η + T) region of the phase diagram [38]. The higher heating rate (Fig.2,17b) increases the enthalpy rate and displaces the thermal effects to higher temperatures compared with Fig.2.17a.

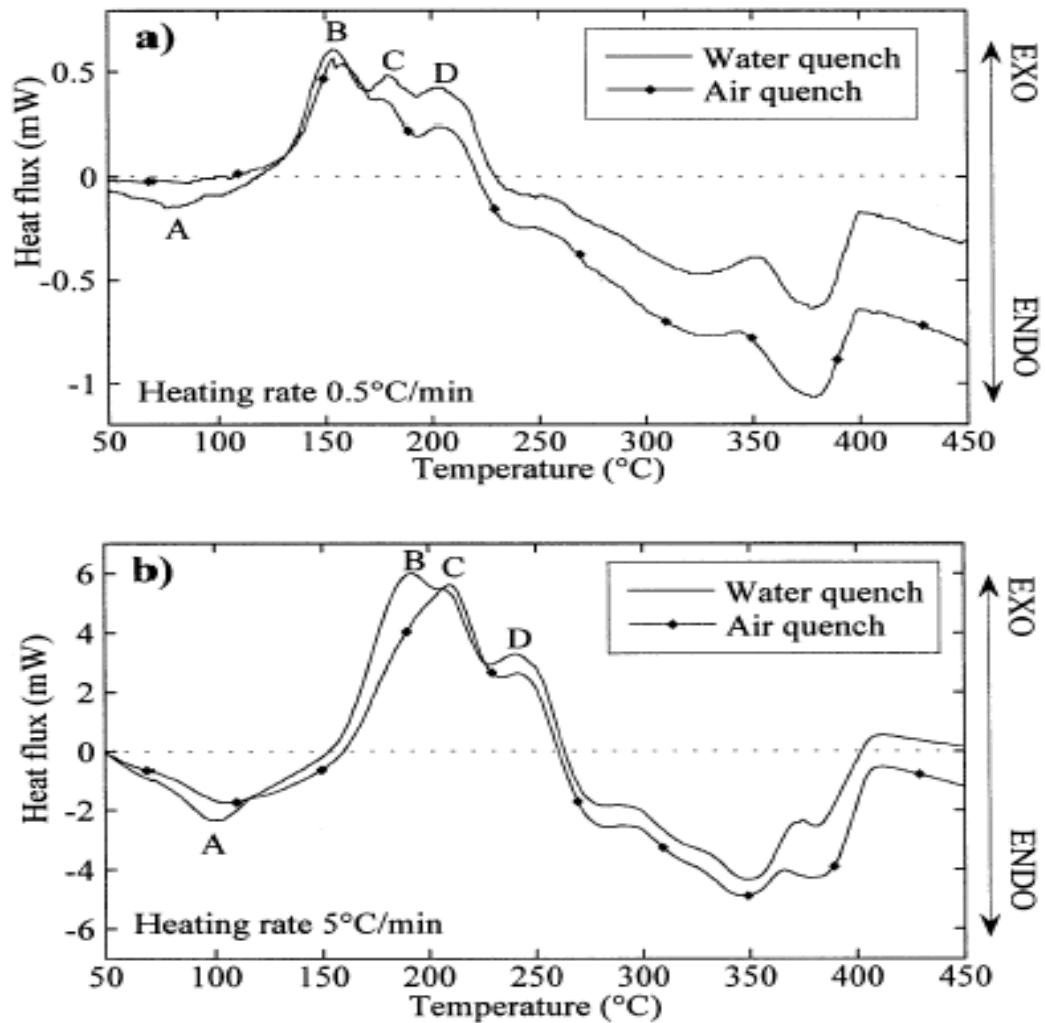


Fig 2.17 DSC thermograms after solution treatment, water or air quench and 3 days natural ageing. On an Al-Zn-Mg alloy (a) 0.5 K/min heating rate; (b) 5K/min heating rate.[38].

2.5.4 Dilatometry

The dilatometric method utilises either transformation strains or thermal strains; the basic data obtained are in the form of curves of length changes against time and temperature [33].

TMA is a technique used in measuring the dimensional changes in materials as a function of temperature or as a function of time isothermally. Stress can be applied to the sample during the analysis. Many important material properties like elastic modulus, melting temperature etc. depend on the atomic interactions and atomic bonding that can be explained using the potential energy. A basic explanation for thermal expansion assumes central forces between pairs of interacting atoms in the case of solids (see figure 2.18). The coefficient of linear expansion, also known as expansivity, is the ratio of the change in length per K to the length at 0 °C. The thermal expansion is a consequence of the nature of interatomic forces, and solid-state theory predicts a simple relationship between specific heat capacity at constant volume (C_V) and the coefficient of linear expansion [33].

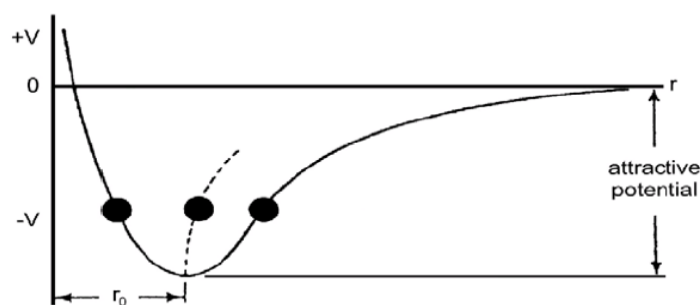


Fig 2.18. Vibration of atoms within an attractive potential. The average interatomic spacing r_0 increases with rising temperature [40].

Applications of TMA:

- a) Determination of linear expansion coefficient
- b) Evaluation of material anisotropy
- c) Determination of phase transition
- d) Determination of melting point
- e) Creep tests

2.6 Physical and mechanical properties of different Aluminium alloy systems

Figure 2.19 shows the qualitative relationship between the properties and characteristics of the various alloy groupings.

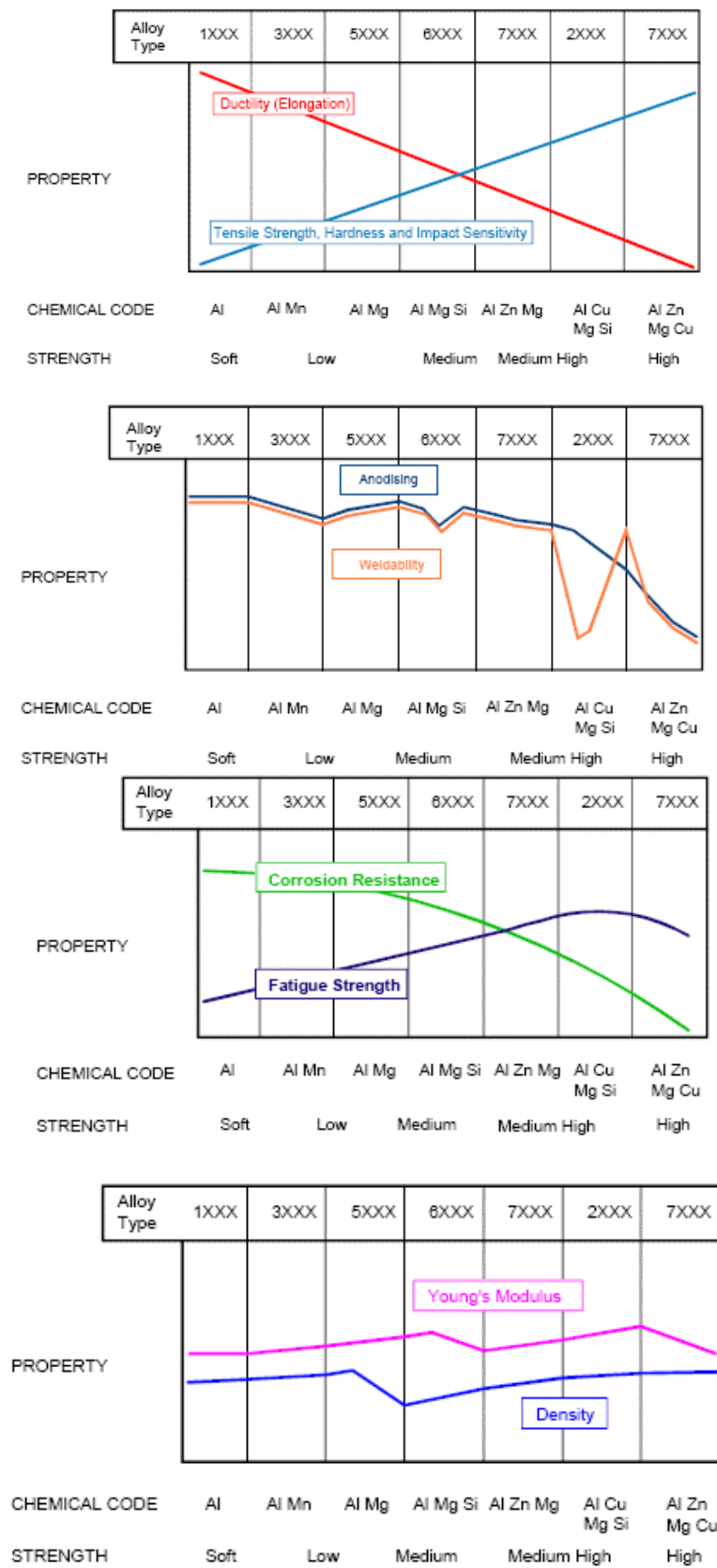


Figure 2-19 Qualitative comparison of some properties of different Al alloy systems [13].

3 Equation and basic model applied

3.1 Thermal analysis

The thermal properties such as thermal expansion behaviour, and thermal conductivity are important in electronic packaging, and automotive applications. The dimensions of most substances increase when they are heated at constant pressure. This is the phenomenon properly called thermal expansion. Different materials also expand at different rates. Over small temperature ranges, the thermal expansion of uniform linear objects is proportional to a temperature change [41]. The coefficient of thermal expansion is non-linear over the range from minus 200 to plus 600°C but for practical purposes is assumed to be constant between the temperature range from 20 to 100°C. The coefficient of thermal expansion of alloys is affected by the nature of their constituents. For example, the presence of silicon and copper in aluminium alloys reduces expansion while magnesium increases [13]. For common commercially used wrought alloys, the coefficient of expansion varies from 23.5×10^{-6} /K for 4.6% Cu aluminium alloy to 24.5×10^{-6} /K for 4.5 % Mg aluminium alloy, i.e. twice that of steel [13].

3.1.1 Volumetric thermal expansion

When a material changes its length equally in all directions with respect to changing temperature, this is called isotropic thermal expansion. If instead of the change in length, the change in volume of a sample is considered, then the volumetric expansion of matter is described by its isotropic expansion coefficient α_v .

$$\alpha_v = \frac{1}{V} \left(\frac{\partial V}{\partial T} \right)_P \quad (3.1)$$

In equation (3.1) V is the volume at a temperature T at constant pressure P . The unit of α_v is K^{-1} and it gives the relative change of volume per Kelvin. The isotropic thermal expansion coefficient has the following thermodynamic relation to the Gibbs free energy G :

$$\alpha_v = \frac{1}{V} \left(\frac{\partial V}{\partial T} \right)_P = \left(-\frac{\partial \ln V}{\partial P} \right)_T \left(\frac{\partial P}{\partial T} \right)_V = K_T \left(\frac{\partial P}{\partial T} \right)_V = K_T \left(\frac{\partial S}{\partial V} \right)_T = K_T \left(\frac{\partial^2 G}{\partial V \partial T} \right) \quad (3.2a)$$

$$\frac{1}{K_T} = V \frac{\partial^2 G}{\partial V^2} \quad (3.2b)$$

In equation (3.2a) S is the entropy. The temperature dependence of the isothermal compressibility K_T is usually neglected compared to the volume derivative of the entropy in evaluation of equation (3.2a). This will be a good approximation for smaller temperature changes. If the free energy and the entropy can be written as a sum of these contributions it is possible to do the same with α_v [66].

3.1.2 Linear thermal expansion

Similar to the volumetric expansion coefficient, we can define the linear thermal expansion coefficient. The linear thermal expansion is defined in the same way as volumetric thermal expansion except that the volume term V is replaced by the length term L . The difference between linear and volumetric thermal expansion coefficients is that, the volumetric thermal expansion coefficient for isotropic polycrystalline materials is three times the linear thermal coefficient with good precision. The strain of a material is defined by

$$\epsilon = \int_{L_0}^L \frac{dL}{L} = \ln\left(\frac{L}{L_0}\right) = \ln\left(1 + \frac{\delta L}{L_0}\right) \quad (3.3)$$

The temperature derivative of (3.3) provides the instantaneous linear coefficient of thermal expansion,

$$\alpha_L(T) = \left(\frac{\partial}{\partial T} \ln L\right)_P = \frac{1}{L} \left(\frac{\partial L}{\partial T}\right)_P \quad (3.4)$$

The average linear coefficient of expansion in the range between T_1 and T_2 is given by

$$\bar{\alpha} = \frac{\left[\frac{(L_2 - L_1)}{L_1}\right]}{(T_2 - T_1)} = \frac{1}{L_1} \frac{\Delta L}{\Delta T} \quad (3.5)$$

There are other ways of representing expansion such as the percentage expansion from T_1 to T_2 is

measured by $\frac{\delta L(T)}{L_0}$. The instantaneous expansion at a temperature is calculated by equation

(3.4). The instantaneous coefficient of thermal expansion (CTE or α) is related to the slope of the tangent of the dimension change ΔL or the length L versus temperature plot at temperature T while the mean coefficient is governed by the slope of the chord between two temperatures,

usually between $T_1=20^\circ\text{C}$ as the reference temperature and a temperature T_2 on the curve (see Fig. 3.1)

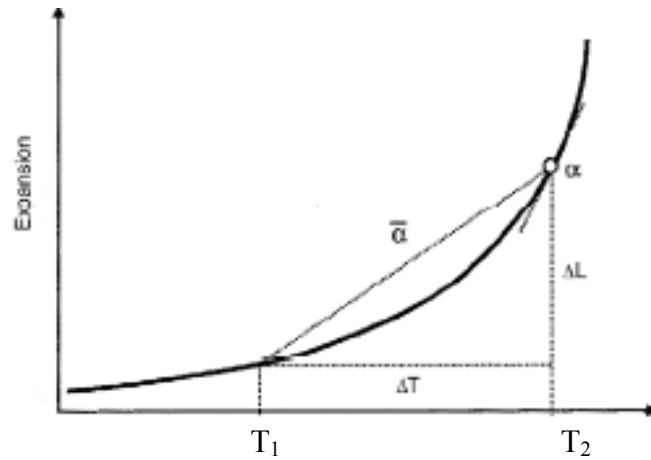


Figure 3.1 Calculation of the instantaneous coefficient of thermal expansion (α_L or CTE) and of the mean coefficient of thermal expansion [42].

Figure 3.2 shows the relative change in lattice parameter ($\Delta a/a_0$) and in linear dimension ($\Delta l/l_0$) for aluminum [40]. Deviation between $\Delta a/a_0$ and $\Delta l/l_0$ occurs near the melting point, because of the formation of a significant number of vacancies that contribute to $\Delta l/l_0$ but do not alter $\Delta a/a_0$. Temperature variation of the CTE for aluminum is also shown in figure 3.2.

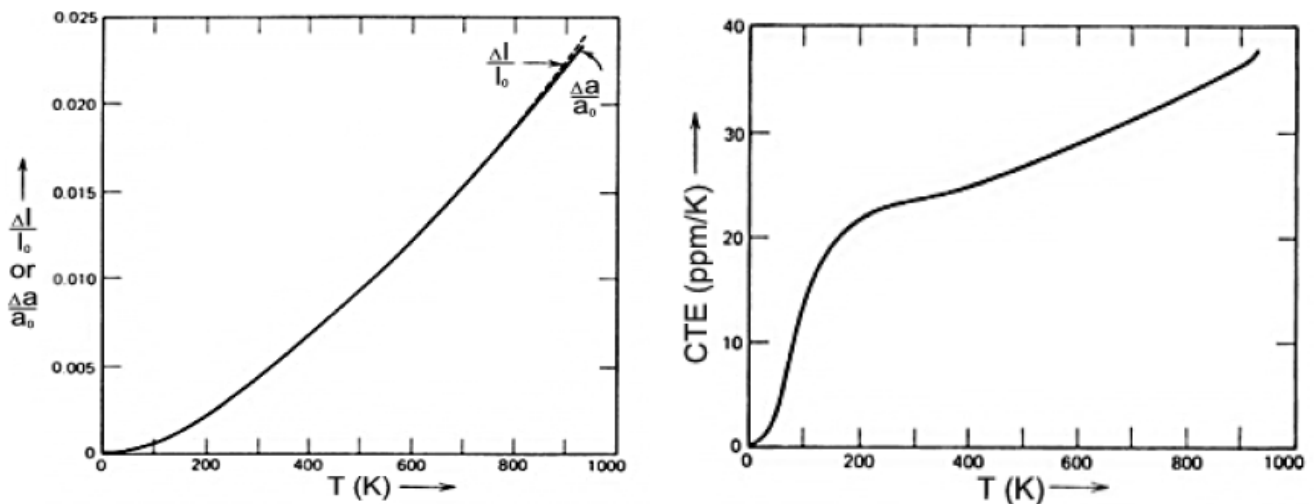


Figure 3.2 (a) relative change in lattice parameter and in linear dimension for aluminium (b) temperature variation of the CTE for aluminium [40]

If the material is isotropic the instantaneous volumetric coefficient of thermal expansion, α_V is three times the instantaneous linear coefficient of thermal expansion, α_L . Subject a cubical object of length L to an infinitesimal change in temperature dT . The new length of the object is

$$L(T + dT) = L(T) + \left(\frac{\partial L}{\partial T}\right)_P dT = L(T)(1 + \alpha_L dT) \quad (3.6)$$

The volume of the object is equal to L^3 , so

$$\begin{aligned} V(T + dT) &= L(T)^3 (1 + \alpha_L dT)^3 \\ &= L(T)^3 (1 + 3\alpha_L dT + 3(\alpha_L dT)^2 + (\alpha_L dT)^3) \end{aligned} \quad (3.7)$$

Since α_L is small, the last two terms are insignificant compared with the linear term $\alpha_L dT$.

$$V(T + dT) = L(T)^3 (1 + 3\alpha_L dT) \quad (3.8)$$

The volume at temperature $T + dT$ is given by

$$V(T + dT) = V(T) + \left(\frac{\partial V}{\partial T}\right) dT = V(T)(1 + \alpha_v dT) \quad (3.9)$$

Comparison of Eq. (3.10) with Eq. (3.9) shows that

$$\alpha_v = 3\alpha_L \quad [92] \quad (3.10)$$

Since thermal expansion is related, on the atomic scale, to atomic vibrations, the chemical or physical bonding interactions between the atoms in the solid are important. A development of the theory of thermal expansion [41] leads to the relation between the coefficient of thermal expansion α and the Young's modulus E (see Fig 3.3).

$$\alpha_L = \frac{\gamma_G \rho C_v}{3E} \quad (3.11)$$

Where γ_G is Grüneisen's constant. Its value varies with the type of material between 0.4 and 4, but for most solids it is near 1. ρ is the density C_v the specific heat (at constant volume joule/mol K) and E the Young's modulus of elasticity. Since ρC_v (volumetric specific heat) is almost constant, the equation shows that α is proportional to $1/E$ [41]. A higher Young's modulus (greater binding energy) corresponds to a lower coefficient of thermal expansion and a smaller degree of asymmetry in the potential curve see figure 2.18. Whereas a large CTE is associated with the greater degree of asymmetry that accompanies a smaller binding energy and thus a lower Young's modulus [40]. For instance diamond with the highest Young's modulus, has one of the lowest coefficients of expansion; elastomers with the lowest moduli expand the most (see Fig. 3.3).

3.2.2 Reaction rate

The rate of a solid state reaction can be written in the general form:

$$\frac{d\alpha}{dt} = g(\alpha)\psi(T) \quad (3.12)$$

Where α is the fraction reacted at time t and T is the absolute temperature. The function $g(\alpha)$ is depending on the actual reaction. The rate function $\psi(T)$ is usually assumed to be given by the Arrhenius law [44,45,46]

$$\psi(T) = \psi_0 \exp\left(\frac{-E_k}{RT}\right) \quad (3.13)$$

Where E_k is the activation energy, ψ_0 the frequency (or pre exponential) factor, and R the gas constant. The fraction reacted is then given by:

$$f(\alpha) = \int_0^t \frac{d\alpha}{g(\alpha)} = \int_0^t \psi(T) dt \quad (3.14)$$

3.2.3 The kinetics of homogeneous transformation

All phase transformations occur in two stages: a nucleation stage, i.e., the formation of critical nuclei of the new phase, and a growth stage of the nuclei, by which these nuclei grow until the material has totally transformed. Homogeneous nucleation takes place when the system does not possess any heterogeneity; where nucleation can occur in a preferential way. The kinetics of homogeneous transformations are conventionally determined from measurements of changes of concentration of one (or more) reactant or product with time, at constant temperature.

3.2.4 The kinetics of heterogeneous reactions

Heterogeneous reactions differ from homogeneous reactions in that the chemically identical constituents of the reactant may possess different reactivities depending upon their location within the sample and the history of each sample preparation. For many reactions involving solids, chemical changes occur preferentially at crystal surfaces, or the regions of direct contact between reactant and product phases (the reaction interface). Each chemical change occurring within this zone of locally enhanced reactivity, where reactant constituents are situated close to the product solid, increases the amount of product phase present. Kinetic analyses thus require

consideration of the systematically changing disposition of the active interface and also, possible influences or controls exerted by rates of diffusion of reactant or product species. [47]

3.2 5 Kinetic interfaces

An interface between two phases possesses an interfacial energy γ , because the atoms at the interface are not in equilibrium positions. The interfacial energy γ [J/m²] is equivalent to surface tension: $F=\gamma$ [N/m]. In case of solid, the interfacial energy depends on the crystallographic plane. The interface between two solid phases α and β can be of two types (see figure 3.4)

(a) Coherent: A register exists between the atomic positions of the two crystal structures.

(b) Incoherent: There is no register between both structures.

Coherent interfaces have a lower interfacial energy than incoherent interfaces $\gamma_{\text{coher}} < \gamma_{\text{incoher}}$

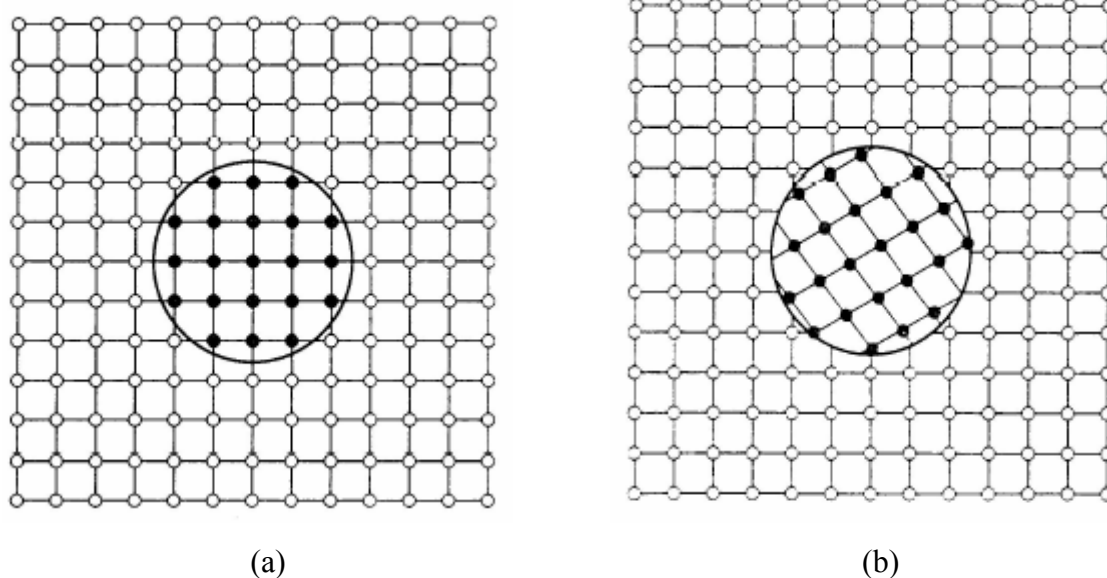


Figure 3.4 (a) coherent (b) incoherent interface structure

3.2 6 Calorimetric methods and interpreting DSC curves

The kinetics and energetics of precipitation can be determined by differential scanning calorimetry (DSC) where the rate of enthalpy is plotted versus temperature $\frac{\partial H}{\partial t}(T) = \dot{H}$ [48].

Each alloy has its own, characteristic DSC curve, with a proper shape and position of the endothermic and exothermic reactions, that could be used for its identification.

When an endothermic reaction starts, the sample requires heat in put (it is represented by a positive enthalpy rate on the axis). The identification of the base line is necessary to evaluate

endo -and exothermic effects. The peak temperature coincides with the temperature at which the reaction rate is maximal. Once the reaction has finished the base line should be reached. DSC gives information on the type and size of the particles that are precipitating or dissolving, indicated by extreme values in the curve $\dot{H}(T)$. The amount of precipitation or dissolution is represented by $\int_{T_1}^{T_2} H dT$. Particle formation and growth may increase with the formation peak.

Dissolution of bigger particles require more heat resulting in a shift of the corresponding peak to higher temperatures. The molar heat of reaction and its sign (exo- or endothermic reaction) characterize the different processes [67]. The fraction of transformation can be measured by

$$\varphi(t) = \frac{A(t)}{A} \quad (3.15)$$

Where φ is the fraction of transformation completed at time “ t_2 ”, $A(t)$ is the area under the DSC curve from the time at which the reaction starts “ t_1 ” up to time “ t_2 ” and A is the total area under the DSC curve.

$$A(t) = \int_{t_1}^{t_2} \Delta C_p dt \quad (3.16)$$

Where ΔC_p is the heat evolved during the reaction actually the total area under the DSC curve, is proportional to the molar heat of reaction ΔH [67].

The table 3.1 shows typical values of the reaction for the most common process in aluminum alloys.

Table 3.1 Typical qualitative reactions involved in various processes in aluminum alloys [67]

Process	Peak type	Peak shape
Melting	Endothermic	Sharp
Phase dissolution	Endothermic	Broad
Solidification	Exothermic	Sharp
Phase precipitation	Exothermic	Broad
Recrystallization	Small exothermic	Broad

The calorimeter measures $\frac{dH}{dt}$, the rate of heat absorption or emission by the sample, as a function of temperature. In the absence of any significant thermal events, the position of the baseline in such a plot is proportional to the specific heat of the sample [49,50,51]. The presence

of an endothermic peak, superimposed on the baseline, indicates the occurrence of a heat absorbing event, such as melting or dissolution of a phase. On the other hand, an exothermic peak occurs as a result of some sort of heat releasing event, such as solidification or precipitation. The area under a peak is proportional to ΔH , the heat absorbed or released by the sample over the temperature range of the peak. ΔH values are obtained from DSC scans by

$$\Delta H = \int_{T_1}^{T_2} H dT \quad (3.17)$$

3.3 Basic concepts in thermodynamics

3.3.1 Phase transformations

To understand the concepts of phase transformations we need to know what a phase is. According to Callister [1999], a phase is “a homogeneous portion of a system that has uniform physical and chemical characteristics”. If more than one phase is present in a system, each one will have its own distinct properties and a boundary separating the phases will exist across which there will be a discontinuous and abrupt change in physical and/or chemical characteristics. This boundary is commonly referred to as the interface and in the case of a phase transformation it is allowed to move.

3.3.2 Equilibrium

Phase transformation occurs, because the initial state of the material under investigation is unstable. The stability of a system is determined by its Gibbs free energy. The Gibbs free energy of a system is defined as

$$G = H - TS \quad (3.18)$$

While

$$H = E + PV \quad (3.19)$$

In which G is free energy, H enthalpy, T temperature in Kelvin, S entropy, E internal energy, P pressure and V is volume of the system. Internal energy is the sum of the total kinetic and potential energy present in the system. Entropy is a measure of the randomness of the system.

A system is in equilibrium, if it is in its most stable state. The laws of thermodynamics dictate that at constant temperature and pressure, a closed system is in stable equilibrium, if it has the minimum amount of Gibbs free energy, i.e. the Gibbs free energy has attained a global

minimum. We say that a system is in metastable equilibrium, if the Gibbs free energy is at a local minimum. In theory, all metastable systems will transform into stable state, if enough time is given above certain diffusivity. A system that is neither stable nor metastable is said to be unstable. Unstable states are only realized for very short periods of time until the system rearranges itself to one of the stable or metastable states. Phase transformations occur because the system always tries to attain the lowest energy state. Therefore any transformation that decreases the Gibbs free energy will occur. Note that through the use of only thermodynamics no claims can be made about the time it takes for metastable states to transform into stable states.

3.4 Precipitation

The creation of a new phase proceeds in three stages: nucleation, growth and coarsening. In reality all three of these processes can take place inside the material at the same time.

3.4.1 Nucleation

To predict the number of nuclei that are produced homogeneously in a system we may use the equation [93]:

$$J = J_0 \exp\left(\frac{-\Delta G_{het}^*}{RT}\right) \exp\left(\frac{-H_d}{RT}\right) \quad (3.20)$$

Where

J_0 = a numerical constant,

ΔG_{het}^* = the energy barrier for nucleation.

If the effect of elastic coherency strains can be ignored (i.e. the increase of Gibbs free energy in the particle due to misfit strain), then according to Myhr and Grong [94]:

$$\Delta G_{het}^* = \frac{(A_0)^3}{(RT)^2 \left(\ln\left(\frac{C_m}{C_e}\right)\right)^2} \quad (3.21)$$

Where

A_0 = a value related to the energy barrier for nucleation,

C_m = the mean solute concentration in the solvent phase,

C_e = the equilibrium solute concentration at the interface.

Combining the last two equations gives us

$$J = J_0 \exp\left[-\left(\frac{A_0}{RT}\right)^3 \left(\frac{1}{\ln\left(\frac{C_m}{C_e}\right)}\right)^2\right] \exp\left(-\frac{H_d}{RT}\right) \quad (3.22)$$

3.4.2 Growth rate

Particle growth/dissolution is governed by a steady-state diffusion field. This means that the rate at which the radius of a spherical particle with radius r grows, is given by

$$\nu = \frac{dr}{dt} = \frac{C_m - C_i}{C_p - C_i} \frac{D}{r} \quad (3.23)$$

in which C_i is the interface solute concentration and C_p is the particle solute concentration. Because the particles are very small we must take capillarity into account, hence

$$C_i = C_e \exp\left(\frac{2\sigma V_m}{rRT}\right) \quad (3.25)$$

in which σ is the interface energy and V_m is the molar volume of the particle. We can deduce the critical radius (i.e. the radius at which a particle reduces its energy by growing) from the above equations by solving $\nu(r) = 0$. We now obtain

$$r^* = \frac{2\sigma V_m}{RT} \left(\ln\left(\frac{C_m}{C_e}\right)\right)^{-1} \quad (3.26)$$

For $r < r^*$ we have $\nu < 0$, so a particle smaller than the critical radius will be unstable and dissolve. On the other hand, for $r > r^*$ we have $\nu > 0$ and thus a particle larger than the critical radius will grow [95].

3.4.3 Growth

The coarsening stage is handled naturally by the described nucleation model. As the solvent phase is depleted of solute and the concentration decreases, the critical radius will increase. This results in smaller particles dissolving and the larger ones growing [95].

The alloying elements travel through the Al-rich phase under the influence of diffusion. Some alloying elements move more easily than others, so each is controlled by its own diffusion equation. Hence, for every $p \in P = \{1, \dots, N_p\}$

$$\frac{\partial C_p(x, t)}{\partial t} = \nabla \cdot (D_p(T) \nabla C_p(x, t)) \quad \text{for } x \in \Omega(t), t \in (0, \infty) \quad (3.27)$$

C_p = the solute concentration at position x and time t

D_p = the diffusion coefficient of alloying element p at temperature T .

We may approximate the diffusion coefficient using the following formula [96].

$$D_p(T) = D_{0,p} \exp\left(\frac{-H_{d,p}}{RT}\right) \quad (3.28)$$

$D_{0,p}$ = a temperature-independent pre-exponential factor

$H_{d,p}$ = the activation energy for diffusion,

R = the gas constant

T = absolute temperature.

3.4.3.1 Ostwald ripening

Ostwald ripening is a physical phenomenon that has been well known for more than a century. This process refers to “the growth of larger particles from those of smaller size which have a higher solubility than the larger ones”.

For particles formed in solution media, there are many chemical equilibria existing between the solid-liquid interfaces under each experimental setting. Because of non-uniformity of particles, concentrations of solutes (or growth nutrients) across the bulk solution vary. The homogenization of these concentration gradients will lead to complete dissolution of smaller particles as a result of the growth of the large particles [112].

This is a spontaneous process that occurs because larger particles are more energetically favored than smaller particles. While the formation of many small particles is kinetically favored, (i.e. they nucleate more easily) large particles are thermodynamically favored. Thus, from a standpoint of kinetics, it is easier to nucleate many small particles. However, small particles have a larger surface area to volume ratio than large particles. Molecules on the surface are energetically less stable than the ones already well ordered and packed in the interior. Large particles, with their greater volume to surface area ratio, represent a lower energy state. Thus, many small particles will attain a lower energy state if transformed into large particles and this is what we see in Ostwald ripening [113].

4 Description of methodology

4.1 Materials

In the current research project, aluminium alloys like AlGe, AlGeSi, series 3XXX, 4XXX, 5XXX, 6XXX, and 7XXX were examined. Experimental and analytical work has been conducted to understand the precipitates and precipitation sequences.

4.1.1 Al-Ge system

Aluminum and germanium form a simple eutectic system with no stable intermetallic phase and limited mutual solubility [52] as shown in figure 4.1.

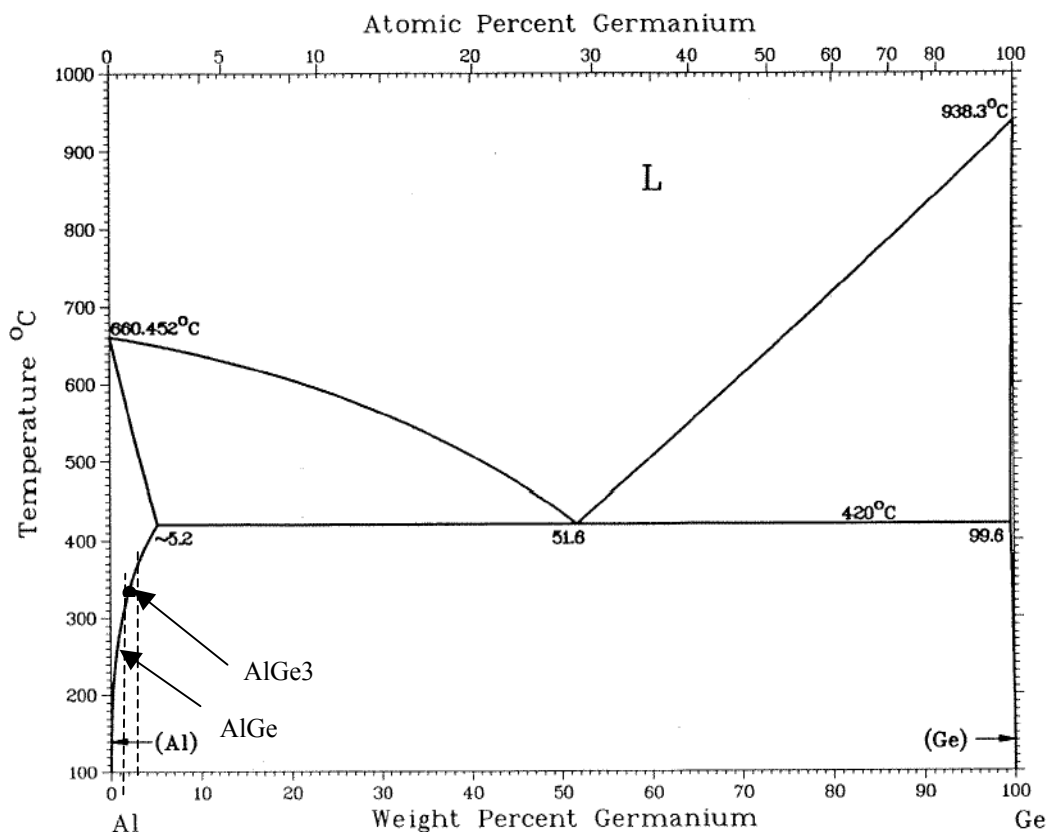


Figure 4.1 System Al-Ge equilibrium diagram [53], where the investigated compositions are marked

Metastable crystalline phases of aluminum and germanium have been investigated extensively, because of the similarities between the aluminum-germanium system and the commercially important aluminum-silicon system, and also because of superconducting properties of AlGe alloys [75]. No compound is formed between aluminium and germanium; an Al-Ge eutectic is formed at 53 to 55 wt% germanium at 424°C. The solid solubilities of germanium in aluminum are given below, Table 4.1

Table 4.1 Solid solubilities of germanium in aluminium at different temperatures [53].

Temperature (°C)	Wt%Ge	at%
424	5	1.9
393	3.5	1.4
295	0.98	0.30
177	0.38	0.14
20	0.30	0.11

4.1.2 Al-Ge-Si system

Ryum [54] found that the “best” ternary heat treatable aluminum alloys often have one alloy element larger than aluminum while the other element should have a smaller atomic radius than aluminum. This “positive negative ” effect will reduce the activation energy for the nucleation of precipitates. As a result a much larger number of precipitates can grow to the critical size for the germanium and silicon rich clusters to transform into the diamond structure. The prerequisite for nucleation of the diamond cubic (d c) phase in aluminium is the solubility of suitable elements in the metallic fcc solid solution. Of the four elements, carbon, silicon, germanium and tin, that may have the d c structure, only silicon and germanium fulfill this requirement. The complete insolubility of the carbon atoms must be due to their small atomic size, and high tendency to form covalent bonds. Tin, owing to its large atomic size, also has no solubility in aluminum and forms the dc structure only at low temperatures ($\leq 13^{\circ}\text{C}$). The formation of the diamond structure is associated with a transformation from metallic to covalent bonding and, consequently, with a change from 12 to 4 nearest neighbours [55].

Germanium and silicon are completely miscible, both are smaller than Al, but Ge is larger than Si. Only two solid phases can be present in this system aluminum solid solution (Al ss) and a GeSi phase which exhibits almost complete solubility with a miscibility gap starting around 500°C as shown in figure 4.2.

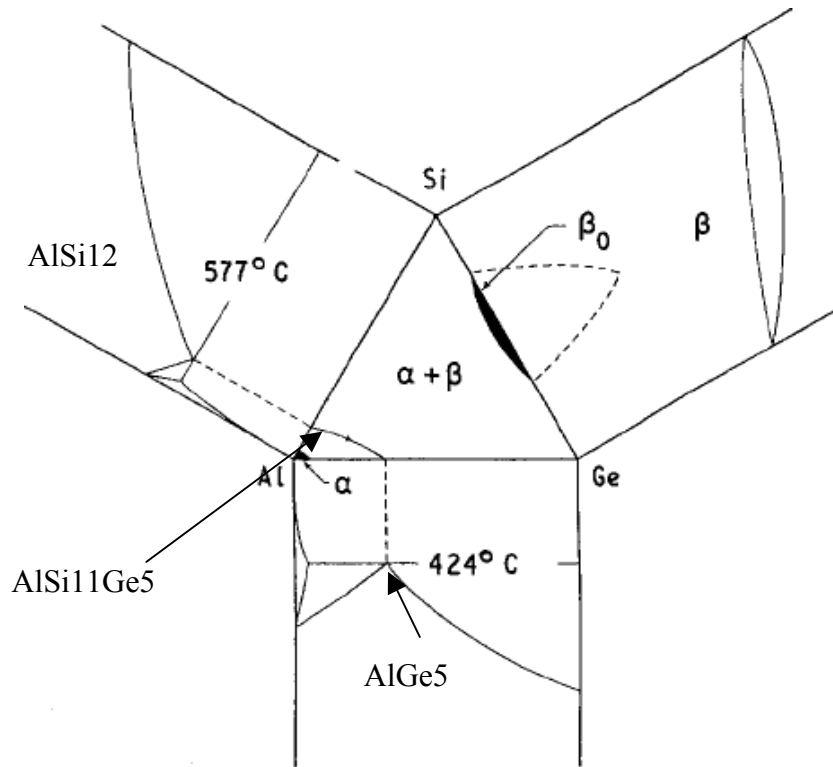


Figure 4.2 Phase diagram Al Si Ge [55].

Different Al-Ge (Si) alloys were produced by laboratory gravity casting at GPM2/INP-Grenoble, France. The homogenizing treatment of the samples after casting were carried out at a temperature of 430°C for 72 hours and then furnace cooled to room temperature. The compositions of the studied materials were determined by EDX analysis and are shown in tables 4.2 and 4.3 a, b, c named these alloys AlGe, AlGe3, AlSi1Ge5, AlSi11Ge5. Figure 4.3a-e show bright field images of Al-Si-Ge near the [110] Al zone axis. The samples were aged at 160° C for 30 min, 2h, 9h, 48h, and 180h, respectively. Precipitates were not detected after aging for 30 min. After 2h the microstructure consisted of a sparse distribution of fine Si-Ge precipitates with black / white strain contrast around them. After 9h the precipitates were still small in size. While samples aged for 48 and 180h showed a progressively coarser microstructure, some seem to become platelets on [111] planes. Throughout this process, the matrix around many of the particles exhibited substantial strain contrast [111].

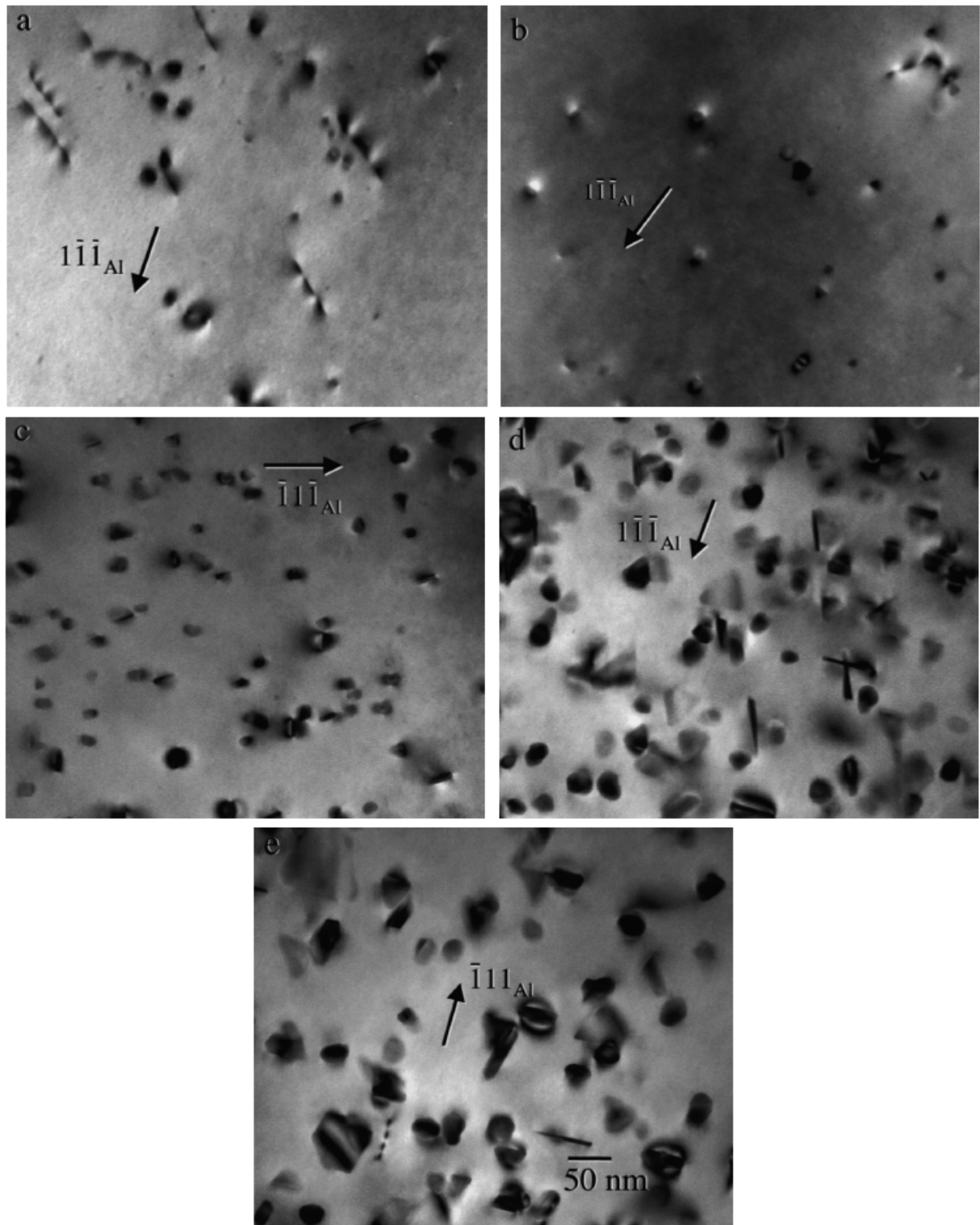


Figure 4.3 Bright field micrographs of Al-1Si-1Ge isothermally aged at 160°C for (a) 30 min, (b) 2 h, (c) 9 h, (d) 48 h, and (e) 180 h [111].

The objective of this part of work is to study the precipitation behavior of Al-Ge and Al-Ge-Si alloys and the effect of natural aging at room temperature of these alloys and compared with each other.

Table 4.2 composition of Al-Ge*

AlGe	Al	Ge	Fe	
Wt%	97.90	1.9	0.2	
At%	99.18	0.71	0.11	

AlGe ₃	Al	Ge	Si	Fe
Wt%	96.60	3.0	0.2	0.2
At%	98.57	1.1	0.19	0.11

Table 4.3 composition of Al-Ge-Si system*

AlSi ₁ Ge ₅	Al	Ge	Si	Fe
Wt%	94.1	4.3	1.3	0.3
At%	96.94	1.6	1.3	1.4

*AlSi ₁₁ Ge ₅	Al	Ge	Si	Fe
Wt%	83,90	4.4	11.4	0.3
At%	86.83	1.7	11.3	0.14

4.1.3 Al-Mn Alloys (3XXX series)

The 3000-group alloys contain manganese as the major alloying element. The manganese will normally exist as finely dispersed intermetallic particles in the material giving a slight to moderate increase in strength. The corrosion properties are excellent and so is the formability. The alloys are often used as drawn tubes and fins in heat exchangers. The solubilities of manganese in aluminum at various temperatures are reported in table 4.4. Figure 4.3 shows in detail the aluminum end of the diagram with the solid solubilities of manganese in aluminum. Al₁₂Mn is quoted as an initial precipitation phase [53] with a bcc structure yielding the same atomic volume as pure Al.

* Samples taken from the “top” of the casting analysed after the homogenization

Table 4.4 Solid solubilities of manganese in aluminium at different temperatures [53].

Temperature (°C)	Wt%Mn	at%
658	1.82	0.9
626	1.35	0.74
570	0.78	0.38
500	0.36	0.17
20	0.05	0.02

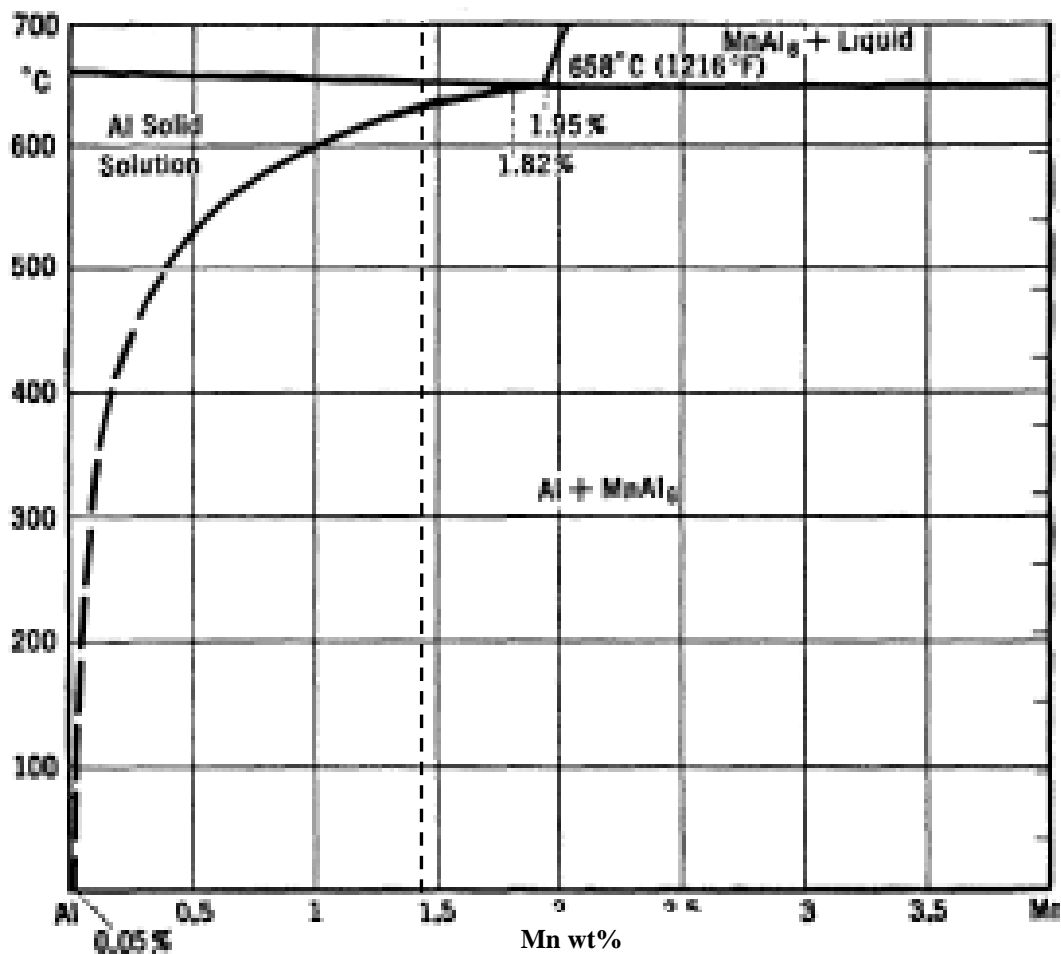


Figure 4.3 System Al-Mn detail of the aluminium end of the equilibrium diagram showing the solid solubility of manganese in aluminium [53] and the composition of investigated alloy.

Chemical composition of the alloy used in the present study is depicted in Table 4.5. Designation of this alloy is AW3003 investigated in strip casting condition.

Table 4.5 Composition of Al-Mn alloy

	Al	Mn	Si	Fe
Wt%	96.50	1.40	1.35	0.75
At%	97.65	0.68	1.31	0.35

4.1.4 Al-Si Alloys 4XXX series

There is a limited solid solubility of silicon in aluminium, as given in Table 4.6. The solid solubilities at different temperatures are reported in detail in the equilibrium diagram Figure 4.4 [53].

In binary Al-Si alloys, Si forms very small coherent [56] clusters, the nature of which depends on Si content [57]. Eutectic Si segregates in diamond structure forming interconnected platelets [71]. Si segregates as polyedric crystals in hypereutectic alloys before the eutectic solidifies. The condensation of excess vacancies into dislocation loops aids the nucleation of Si clusters from solid solution [58, 59]. Si precipitates in a diamond structure without any intermediate stages from these clusters. The new phase forms as rods or triangular plates on several planes of the aluminium matrix [55]. Nuclei are very small and vacancies play an important role during the transformation from the coherent clusters into incoherent particles, which occurs at a cluster diameter less than 2nm.

Table 4.6 Solid solubilities of silicon in aluminium at different temperatures [53].

Temperature (°C)	Wt%Si	at%
577	1.65	1.7
550	1.30	1.24
500	0.80	0.81
450	0.48	0.46
400	0.29	0.27
350	0.17	0.16
300	0.10	0.11
200	0.05	0.05

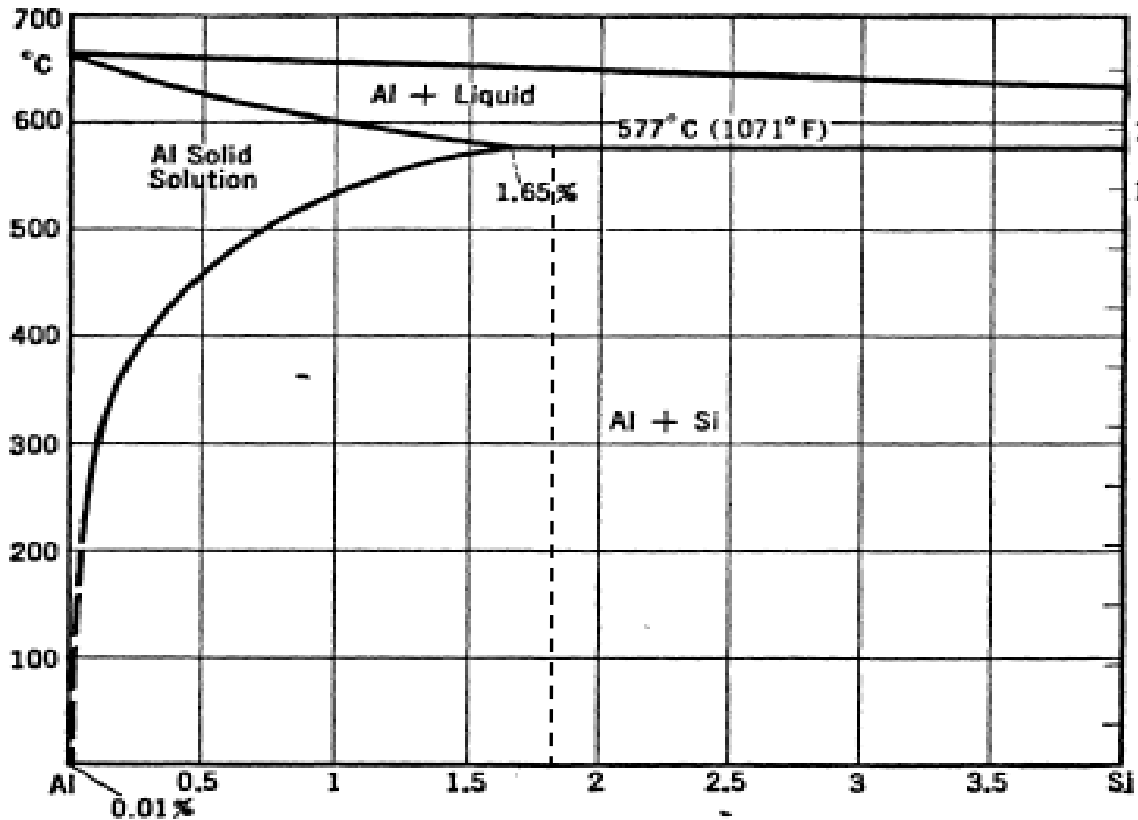


Figure 4.4 System Al-Si, detail of the aluminium end of the equilibrium diagram, showing the solid solubility of silicon in aluminium [53] and the composition of AlSi1.7.

The different AlSi-alloy samples were produced using squeeze casting by LKR, Ranshofen Austria. The compositions of the studied materials are given in Table 4.7, 4.8 which named Al low Si alloy (AlSi1.7) Al high Si alloy (AlSi12)

Table 4.7 composition of Al-low Si alloy (AlSi1.7)

	Al	Si
Wt%	98.26	1.74
At%	98.38	1.62

Table 4.8 composition of Al-high Si alloy (AlSi12)

	Al	Si
Wt%	88.13	11.87
At%	88.62	11.38

4.1.5 Al-Mg Alloys (5XXX series)

Magnesium forms a complicated system with Al, as depicted in figure 2.7. Mg has a very high solubility in aluminium (up to 17.4 Wt% at the eutectic temperature 450°C). Its solubility decreases to approximately 1.7 Wt% at room temperature but the rate of decomposition of the supersaturated solid solution is very low [28]. Solid solubilities of magnesium in aluminium are reported in Table 4.9

Table 4.9 Solid solubilities of magnesium in aluminium in different temperatures [53]

Temperature (°C)	Wt%	at%
449	17.4	18.93
400	13.5	14.30
350	9.90	10.88
300	6.70	7.21
250	4.40	4.86
200	3.10	3.43
150	2.30	2.55
100	1.90	2.10

Binary Al-Mg alloys show an abnormally small response to aging. Precipitation may occur, but no hardening is observed until the Mg content exceeds 5%. In cold worked alloys, rod-shaped precipitates of Al_3Mg_2 (β phase) are nucleated on dislocations but have no significant strengthening effect. However, in alloys with Mg content higher than 4%, cold working may result in precipitation at grain boundaries [28]. No wrought 5XXX alloys exploits precipitation hardening to obtain higher levels of strength. Casting alloys with a high Mg content can exhibit some degree of age hardening behaviour when subjected to the right thermal conditions [60]. The nucleation and growth of the β phase on grain boundaries in certain Al-Mg ($> 3\%$ Mg) alloys at ambient temperatures reduce ductility and resistance to stress corrosion cracking [28].

Chemical composition of the hot rolled alloy used in the present study in this part is depicted in Table 4.10 designation of this alloy is AW5083.

Table 4.10 Composition of AW5083

	Al	Si	Mn	Mg	Fe	Cr
Wt%	93.93	0.24	0.59	4.74	0.35	0.10
At%	93.87	0.22	0.30	5.40	0.16	0.05

4.1.6 Al-Mg-Si Alloys (6XXX series)

Magnesium is often added to Al-Si alloys to form the pseudo binary Al-Mg₂Si (Mg:Si =1.73) for strengthening by the formation of Mg₂Si precipitates. In alloys, with excess of Si, Mg₂Si content can be found by [61].

$$\text{Wt}\% \text{Mg}_2\text{Si} = 1.578 (\text{Wt}\% \text{Mg}) \quad (4.1)$$

The pseudo binary system, which is presented in figure 4.5 has an eutectic at 595°C and a maximum solid solubility of 1.85Wt% Mg₂Si. Si available for Mg₂Si formation is affected by the presence of Mn and Fe in the alloy and expressed by [62]

$$\text{Si}(\text{available for Mg}_2\text{Si}) = \text{Wt}\% \text{Si} - \frac{1}{4} (\text{Wt}\% \text{Fe} + \text{Wt}\% \text{Mn}) \quad (4.2)$$

Excess Si reduces the solubility of Mg₂Si, enhances the rate of precipitation and increases the density of GP zones. GP zones are fine plates having a thickness of one atomic layer, and a length of about 30 nm [63] and are formed randomly in the matrix and also heterogeneously on matrix dislocations [64,65].

Two types Al–Mg–Si alloys (with an excess of silicon) supplied by “AMAG rolling” were examined. The two material types were manufactured by two different processes, Directly-Cast (DC) and strip Cast (CC). Composition of these two alloys are given in Table 4.11, 4.12 designated Al6016DC and Al6016CC. Both contain excess Si not bounded by Mg₂Si nor by Fe aluminides.

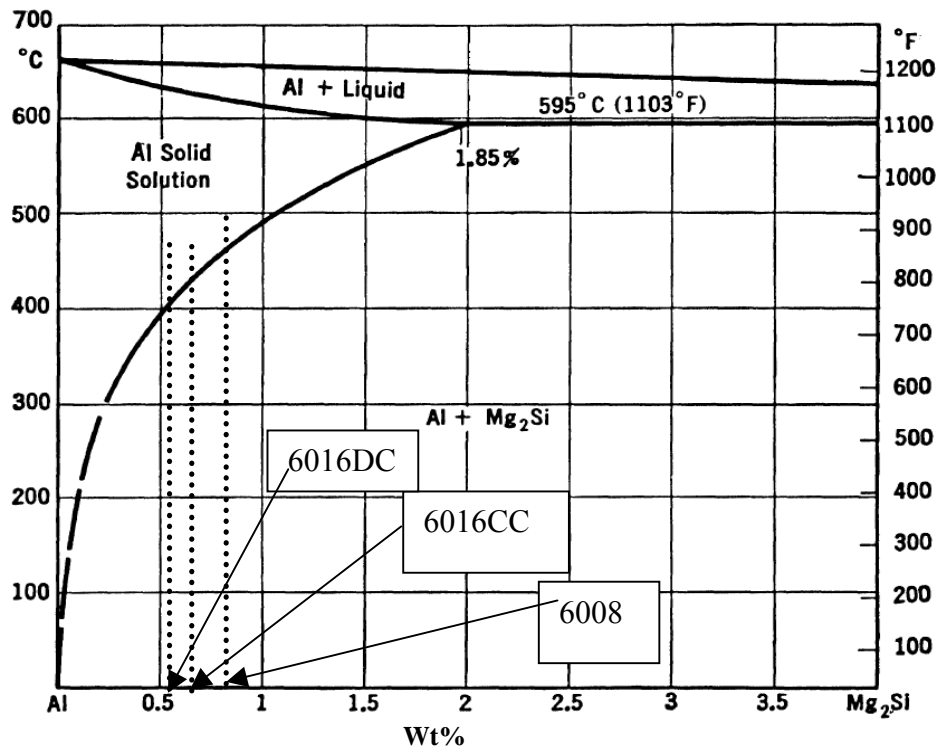


Figure 4.5 System Al-Mg-Si, quasi-binary section Al-Mg₂Si, showing the solid solubility of Mg₂Si in aluminium [53].

Table 4.11 Composition of AW6016DC

	Al	Si	Mg	Mn	Cu	Fe	Mg ₂ Si	Si ^{ex}
Wt%	98.25	1.08	0.34	0.07	0.07	0.19	0.54	0.84
At%	98.45	1.03	0.38	0.03	0.03	0.08	-----	-----

Table 4.12 Composition of AW6016CC

	Al	Si	Mg	Mn	Cu	Fe	Mg ₂ Si	Si ^{ex}
Wt%	98.18	1.02	0.43	0.08	0.03	0.26	0.68	0.71
At%	98.40	0.97	0.46	0.03	0.01	0.13	-----	-----

The third type, 6008 alloy was taken from extruded profiles. The composition of this alloy is depicted in Table 4.13, which presents higher Mg₂Si precipitation but less excess Si.

Table 4.13 Composition of AW6008

	Al	Si	Mg	Mn	Cu	Fe	V	Mg ₂ Si	Si ^{ex}
Wt%	98.25	0,57	0,55	0,26	0,07	0,19	0.11	0.87	0.20
At%	98.59	0.54	0.60	0.11	0.03	0.08	0.05	-----	-----

4.1.7 Al-Zn-Mg- Alloys (7XXX series)

The wrought alloy systems of Al–Zn–Mg, with addition of Cu, comprise the highest strength aluminium alloys. This alloy system offers the best combination of strength, fracture toughness, and corrosion resistance over many other aluminium system. The equilibrium phases in the Al–Mg–Zn alloys are MgZn₂ (η), Mg₃Zn₃Al₂ (T) and Mg₅Al₃ (β). If the quantity (at%) of Zn>Mg, than the precipitation sequence to MgZn₂ is predominant. If there is more Mg than Zn, then the sequence to the equilibrium precipitate Mg₃Zn₃Al₂ (T) predominates. If Cu is added, the order of alloying element quantity is generally Zn>Mg>Cu. If Cu>Mg, then the sequence to the S phase (Al₂CuMg) predominates.

The alloy selected for this part of study is AW7349 alloy. Samples were taken from cylindrical billets in as cast condition and homogenized for 470°C/14h followed by 478°C/24h [74]. Chemical composition of the alloy is shown in Table 4.14.

The various phases, which precipitate in this system are shown in table 4.15.

Table 4.14 Composition of AW7349 (1C-A)

	Al	Si	Zn	Mg	Cu	Sc	Zr	Cr	Fe
Wt%	86.30	0.08	8.31	3.12	1.49	0.37	0.10	0.14	0.42
At%	91.46	0.06	3,64	3,66	0,66	0,23	0.03	0,06	0,20

Table 4.15 Various phases which may at maximum precipitate in AW7349 (1C-A)

	MgZn ₂	Al ₂ CuMg	Mg ^{ex}	or	Al ₂ Mg ₃ Zn ₃	Al ₂ Cu
At%	5.5	2.6	1.2		9.7	2

4.2. Experimental methods

Three principal experimental methods were used in this study. Hardness measurement, differential scanning calorimetry (DSC) and dilatometry.

4.2.1. Hardness measurements

Hardness measurements generally gives an idea of the age hardening behavior of an alloy at a particular temperature. In this method a small indenter is forced into the surface of the material to be tested, under controlled conditions of load and rate of application. The depth or size of the resulting indentation is measured, which in turn is related to hardness values. The softer the material, the larger and deeper the indentation, thus the lower the hardness value.

Samples of identical shapes used for differential scanning calorimetry and dilatometric measurements were used to perform hardness tests by means of an universal tester model M1C010 provided by Emco test. Brinell hardness was measured using a load of 10kg and 1mm ball. The samples were tested in different thermal conditions at room temperature.

4.2.2 General description of differential scanning calorimetry DSC 2920 CE

DSC has become a rapid, inexpensive, and quantitative tool for microstructural characterization in aluminum alloys [68,69]. In its simplest form, and under appropriate conditions DSC can show which precipitates are present and their volume fractions formed or dissolved during heating [70]. Also, additional information pertaining to reaction kinetics can be derived from the thermograms as explained in chapter 3 (3.2.6).

The DSC instrument, which we used, was DSC2920CE (see figure 4.6). The heat flux 2920CE instrument contains the system electronics, and the cell, which contains its own thermocouples (temperature sensor) for monitoring differential heat flow and temperature. The measurements provide quantitative and qualitative data relative to physical or chemical changes of a material involving endothermic or exothermic processes with a sensitivity of 0.1 μ W. The DSC cell has a constantan (thermoelectric) disc as a primary heat-transfer element. A silver heating block, capped with a vented silver lid, encloses the constantan disc.

The selected sample and reference sample are placed in pans that sit on raised portions of the disc. Heat is transferred through the constantan disc to both the samples and reference pans.

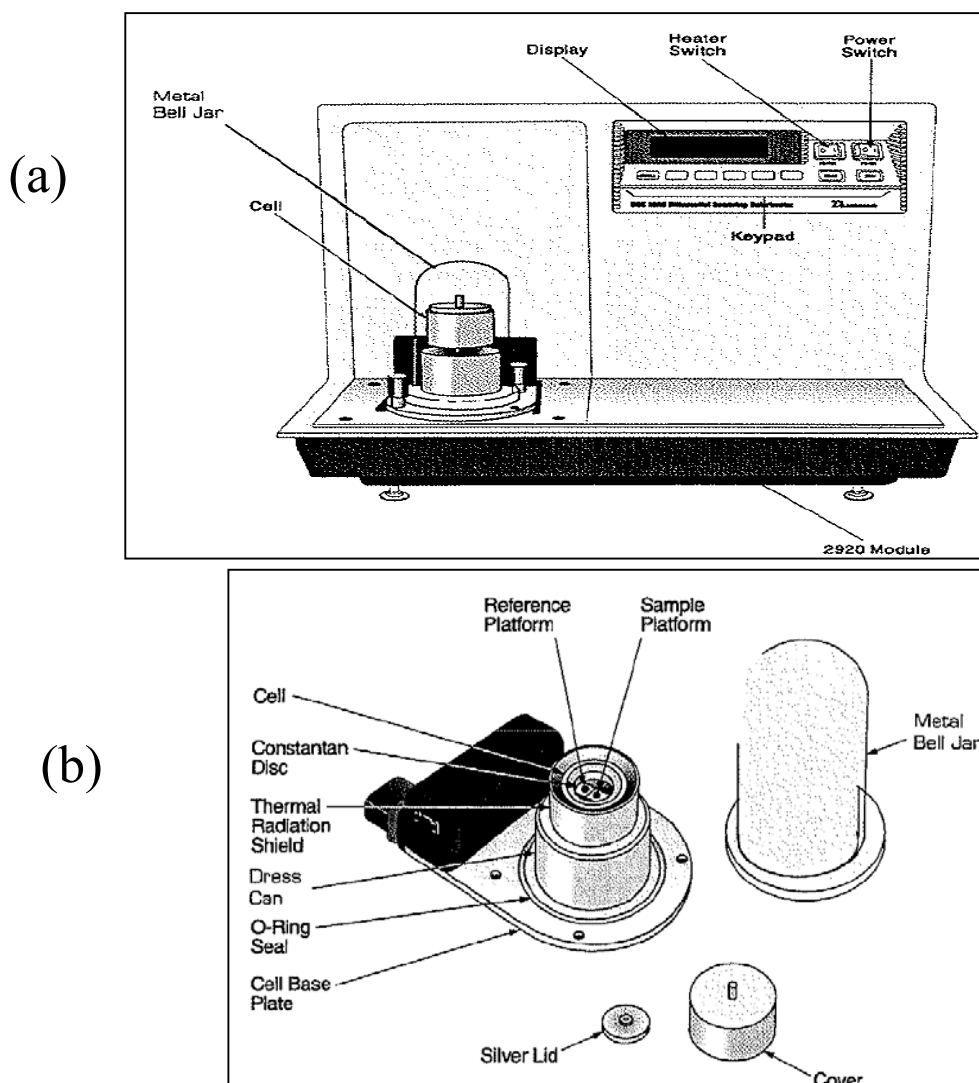


Figure 4.6 Heat flux DSC2920CE instrument (a) DSC controller (b) DSC cell

Differential heat flow to the sample and reference are monitored by the chromelconstantan area thermocouples. The thermocouples are formed at the junctions of the constantan disc and the chromel wafers welded to the underside of the two raised portions of the disc. Chromel and alumel wires are connected to the chromel wafers at the thermocouple junctions to measure sample temperature. The alumel wire welded to the reference wafer is for thermal balance. Purge gas, entering the heating block through an inlet in the DSC cell's base plate, is preheated to block temperature by circulation before entering the sample chamber through the purge gas inlet. Gas exits through the vent hole in the silver lid. Vacuum and air cooling ports on the DSC 2920 CE lead to openings in the cell but not directly to the sample chamber. A bell jar, placed over the cell and sealed with an O-ring, protects the operator from evolved gases and permits cell evacuation [71].

4.2.2.1 Calibration of DSC

To obtain accurate experimental results, we should calibrate the DSC instrument with identical samples. The calibration will be stored in the cell memory and automatically entered when the cell is installed. Once the initial calibrations are done we can save the resulting data files and reuse them when needed. For the best result, however, we should recalibrated periodically.

We plan to perform calibration runs encompass the temperature range in our experiments. If we change the general temperature range of our experiments, we should recalibrate within the new range. For precise experimental results we will need to generate a new calibration file whenever we change one of the following parameters:

- Ramp rate
- Purge gas
- Cooling technique
- First use of the cell.

Calibration consists of several types of specific procedures, which will be described briefly below.

4.2.2.1.1 Baseline slope and offset calibration

The baseline slope and offset calibration need to be performed separately on each cell. This calibration involves heating an empty cell through the entire temperature range expected in subsequent experiments. In our experiments we took between room temperature to 600°C.

Ideally, the heat flow signal should be zero, since there is no sample in the cell, and it should have minimum slope. The calibration program is used to calculate the slope and offset values needed to flatten the baseline and zero the heat flow signal.

4.2.2.1.2 Cell constant calibration

This calibration is based on a run in which a calibration material (e.g., indium) is heated through its melting point. The calculated heat of fusion is compared to the theoretical value. The cell constant is the ratio between these two values. In calibration of the DSC, the cell constant calibration is performed in two experiments. In the first experiment the calibration material is placed on sample side A, and sample side B is left vacant. In the second experiment, this

arrangement is reversed, so that the standard is placed on sample side B, and sample side A is left vacant.

4.2.2.1.3 Temperature calibration

Temperature calibration is based on a run in which a temperature calibration material (e.g., indium) is heated through its melting point. The recorded melting point of this material is compared to the known melting point, and the difference is calculated from temperature calibration.

4.2.2.2 Baseline correction in calorimetry

Although modern calorimeters are reliable instruments that can achieve remarkably high accuracy in measurements of heat evolution, no instrument is perfect and parasitic effects will always occur. In calorimetry, parasitic effects are often induced by disturbances from outside of the measuring cell causing transients in heat flows within the zones where heat evolution from the sample and reference are measured [72]. When DSC are used for specific heat measurements the baseline deviation becomes important. To identify base line drift, two separate DSC runs were carried out. In the first run, high purity annealed aluminum disks were placed in both the sample and reference holders, while in the second run the aluminum disk in the sample holder was replaced by the disk of the material under study. In a third run the material in the sample holder is replaced by pure aluminium disk. With this method, just before and after the test, the base line can be checked. The actual DSC curve of the alloy was obtained by subtraction of the first from the second DSC curve.

4.2.2.3 Procedure of DSC tests

Small disks were punched from materials under study, approximately 6 mm diameter, 1-1.2mm thick. The disks were solution heat treated according to typical heat treatment applied on materials listed in tables 4.16-4.21. DSC tests were conducted on each material in the as quenched condition transferring within 10-20 minute into the DSC (W.Q) or after room temperature with different aging time (W.Q +RT called T4). Heating rates $\frac{dT}{dt} = 5$ and 10K/min were used for the experiments (see figure 4.7). The DSC scans were initiated at 30°C and completed at convenient temperatures. The output was in milliwatts (mW). The net heat flow per time $\frac{dH}{dt}$ per mass of the sample was obtained by subtracting the specific base line data from the

specific heat data of the samples and recorded as a function of temperature. The enthalpy of transformation would be obtain by $\frac{dH/dt}{dT/dt}$, thus the signals are stronger for faster heating rates

4.2.2.4 The heat treatment before DSC

Table 4.16 Typical heat treatment applied to AlGe ,AlGeSi alloys

Alloy	Solution	Condition of Solution
AlGe	W.Q	430°C/30min+w.q
AlGe3	W.Q	430°C/30min+w.q
AlSi1Ge 5	W.Q	415°C/30min+w.q
AlSi11Ge5	W.Q	415°C/30min+w.q

Table 4.17 Typical heat treatment applied to AW3003

Alloy	Solution treatment	Condition of Solution treatment
AW3003	W.Q	620°C/30min+w.q
AW3003	W.Q	540°C/20min+w.q
AW3003	W.Q	400°C/30min+w.q

Table 4.18 Typical heat treatment applied to AlSi alloys

Alloy	Solution treatment	Condition of Solution treatment
AlSi1.7	W.Q	480°C/3h+w.q
AlSi1.7	W.Q	540°C/15min+w.q
AlSi1.7	W.Q	480°C/15min+w.q
AlSi1.7	W.Q	450°C/15min+w.q
AlSi12	W.Q	540°C/15min+w.q
AlSi12	W.Q	480°C/15min+w.q
AlSi12	W.Q	450°C/15min+w.q

Table 4.19 Typical heat treatment applied to AW5083

Alloy	Solution treatment	Condition of Solution treatment
AW5083	W.Q	550/1h+w.q
AW5083	W.Q + isothermal	As above +100K/s up to 200°C /16h

Table 4.20 Typical heat treatment applied to Al6xxx series

Alloy	Solution treatment	Condition of Solution treatment
AW6016DC	W.Q	550°C/15min+w.q
AW6016CC	W.Q	550°C/15min+w.q
AW6008	W.Q	550°C/15min+w.q
AW6008	T104	Simulation of heat affected zone (see figure 4.8)

Table 4.21 Typical heat treatment applied to AA7349

Alloy	Solution treatment	Condition of Solution treatment
AA7349	W.Q	480°C/20min+w.q
AA7349	W.Q	480° C/20min+w.q+RT
AA7349	T4	480°C/20min+w.q+RT (1 day)
AA7349	T6	120°C/24h

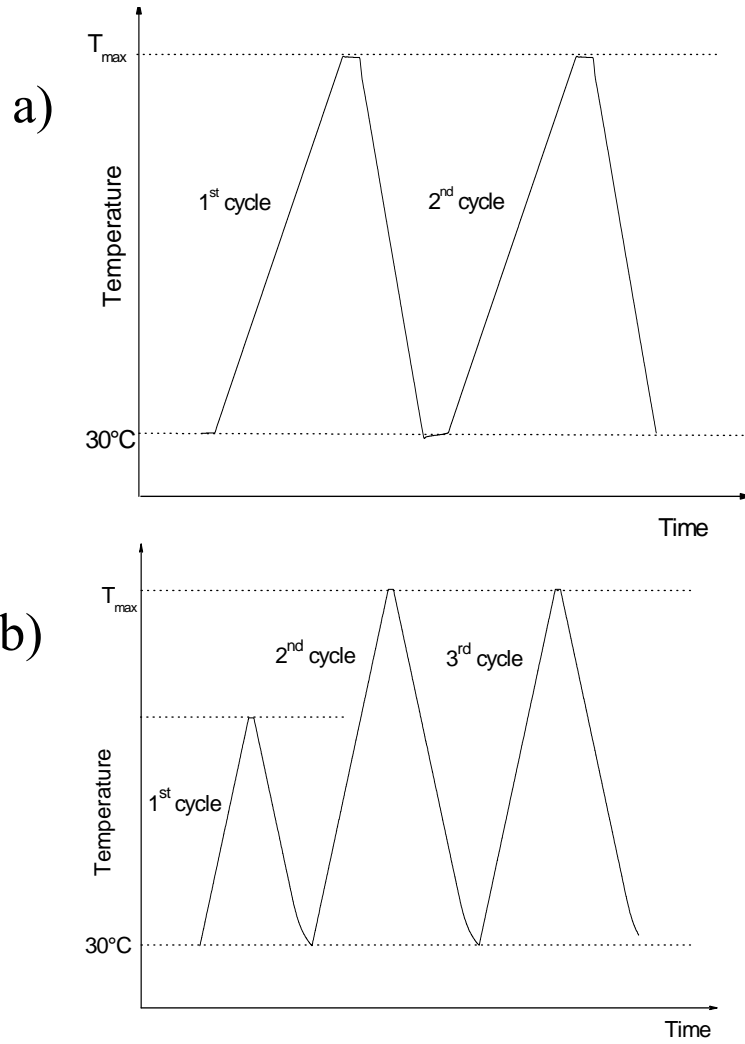


Figure 4.7a,b Show two kinds of temperature –time curves, heating rate 5 or 10K/min, cooling rate 5, 10 or 20K/min and holding time 5 or 10min which are used for samples.

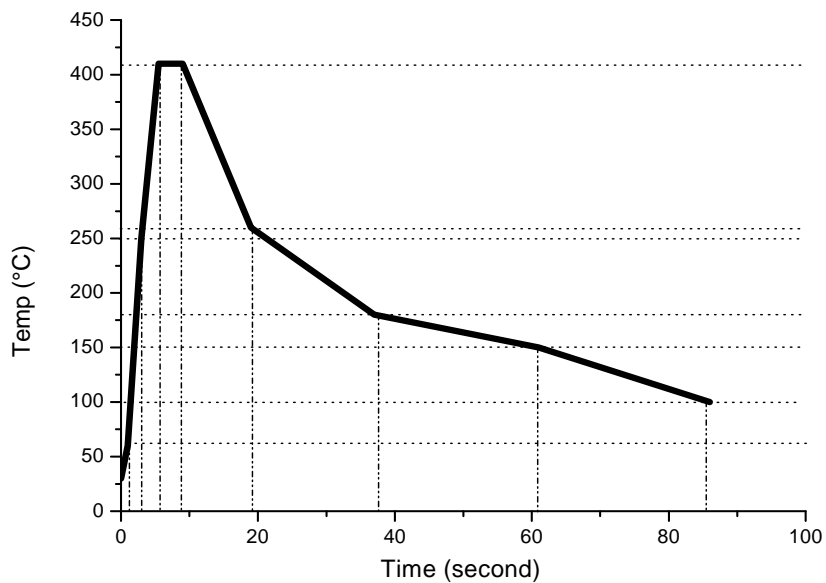


Figure 4.8 Temperature-Time curve of T104 condition of AW6008 simulating the HAZ.

4.2.3 General description of TMA 2940

The thermo mechanical analyzer (TMA) measures any linear changes in the dimension of a specimen as a function of time, temperature (in the range between -70°C and $+1000^{\circ}\text{C}$), and force. A schematic drawing of the instrument is shown in Figure 4.9

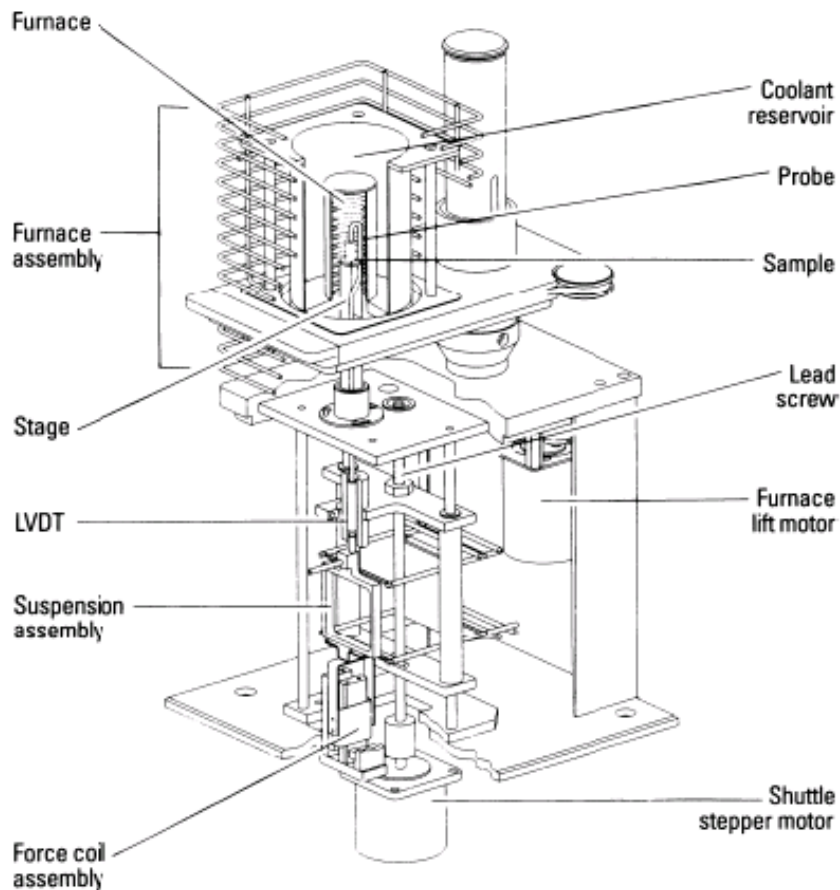


Figure 4.9 Schematic drawing of TA Instruments type: TMA 2940 [73]

The heart of the device is a moveable-core linear variable differential transformer (LVDT), the output of which is proportional to the linear displacement of the core caused by changes in sample's dimensions. The core itself is part of a quartz probe that contacts the sample. In the TMA, the sample is positioned above the LVDT, on the quartz stage and the movable probe was placed on the top of the sample (see Figure 4.10). The quartz probe with a low coefficient of thermal expansion of about 0.5ppm/K transmits changes in the length of the specimen to the transducer (LVDT) with a resolution of $0.1\mu\text{m}$. The sample temperature is measured using a thermocouple, positioned close to the sample. An optional cooling device placed around the furnace core accommodates programmed cooling and subambient operations. The furnace is

filled with nitrogen during the experiments (usually 100 ml/min). Force applied to the sample (0.001 to 1N) is generated and controlled by an electromechanical coil. The force can be held constant or varied during an experiment. The exerted pressure by the probe, with a diameter of 3mm, results in a stress of 7kPa.

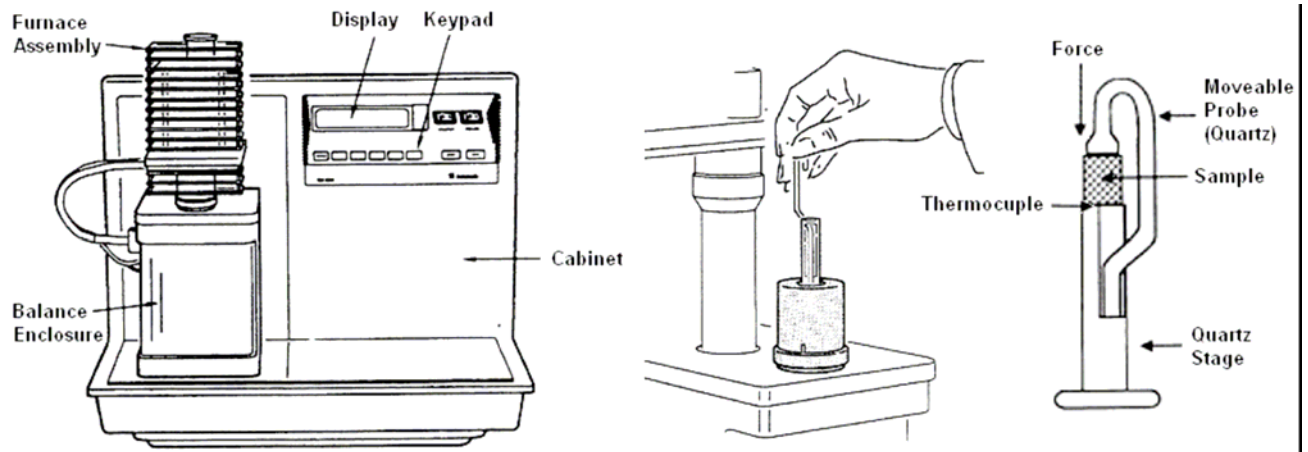


Figure 4.10 Specimen positioning in the TMA 2940

4.2.3.1 Calibration of TMA

The calibration of the TMA instrument was done according to ASTM standard method E-831 consisting of a temperature calibration and a calibration of the expansion response. The temperature calibration of the thermocouple is based on a run in which a temperature standard is heated through its melting point. The recorded melting point of this standard is compared to the known melting point, and the difference is calculated for temperature calibration. For the most accurate measurement of coefficient of thermal expansion (CTE), it is necessary to calibrate the expansion response of the thermo mechanical analyzer (TMA) using a reference material. The cell constant calibration is based on an experiment with a pure aluminium standard.

4.2.3.2 Procedure of Dilatometry tests

Dilatometric tests were carried out on a TMA 2940 CE thermal mechanical analysis equipment (TA Instruments). The expansion (Δl) of the specimens was measured between RT and convenient temperature at a heating rate of 5 or 10K/min in a nitrogen atmosphere. A numerical derivative of the smoothed Δl vs. T-curve provides the instantaneous coefficient of thermal expansion (CTE) at a temperature T (see figure 4.11). Specimens for TMA testing, were cut from various materials with a dimension of $3 \times 4 \times 12 \text{ mm}^3$. The top and the bottom of which were ground and polished to obtain plane-parallel surfaces for the measurement. The error in

CTE(T) measurements is estimated to be less than 1ppm/K. The CTE was only calculated 10K above RT until 10K below maximum temperature to avoid smoothing errors.

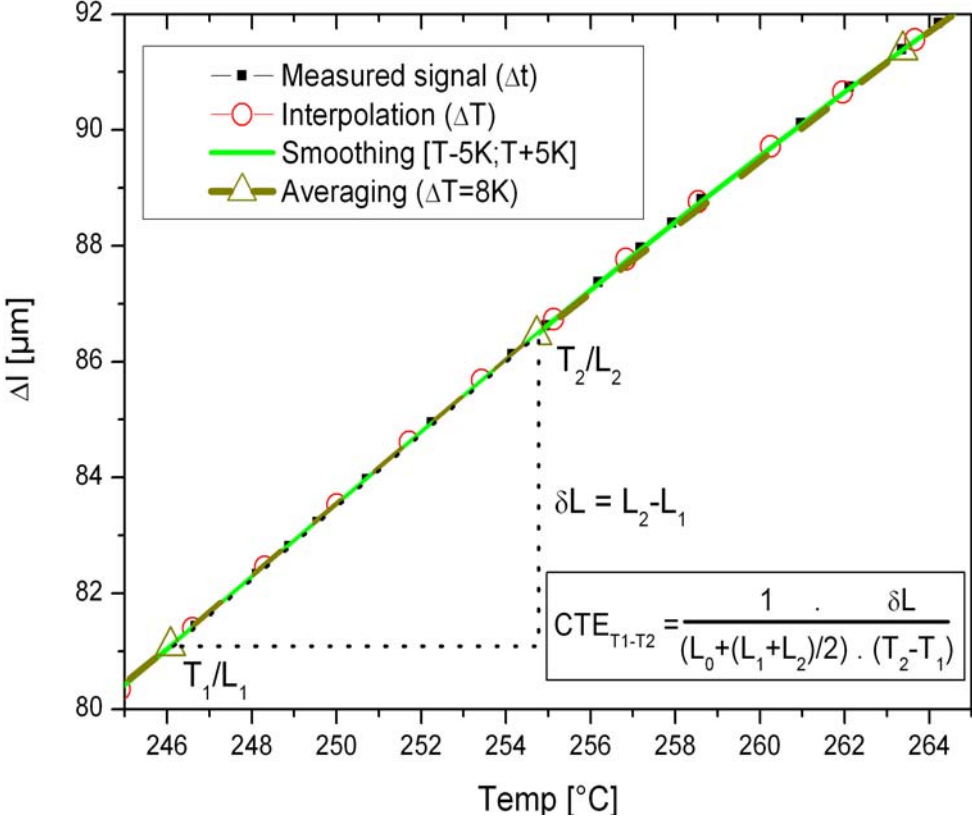


Figure 4.11 Method of differentiating the measurements to obtain the instantaneous CTE(T)

5. Experimental results

5.1 Metallography of samples

5.1.1 Al-Ge and Al-Ge-Si alloys

The microstructures of AlGe as cast alloy with different magnification by optical micro copy in figure 5.1a and b, and by a SEM image of this alloy is shown in figure 5.2. These micrographs show some porosity and interdendritic eutectic Al-Ge due to segregation during solidification.

Micrographs of AlGe5Si with low Si content (Figure 5.3a and b) show grain boundary decoration but in high Si content AlGe5Si11 (Figure 5.4a), we can see needle like structures. Figure 5.4b shows an optical micrograph of AlGe5Si11 with lower magnification, revealing a dendrite structure in this alloy. SEM BSE images of deep etched samples of this alloy show two kinds of particles, white and grey particles (see figure 5.5 and 5.6). The particles analysed by EDX marked “1” (white) and “2” (grey) in figures 5.7 and 5.8 show that the white particle is richer in germanium than the grey. The relative atom content of the white particles Ge:Si ~ 1:1 whereas the grey exhibit Ge:Si=1:13

5.1.2 Al-Mn Alloys (3XXX series)

The microstructure of the Al-Mn alloy in strip cast condition is shown in figure 5.9. This micrograph shows little pores and many particles. The particle structure of the AW3003 alloy is presented in Figure 5.10. From this figure it is seen, that the particles were formed mostly at grain boundaries.

Mapping analysis of the AlMn alloy is shown in figure 5.11 and indicates the distribution of alloying elements, where most of the particles are Fe-Mn aluminides. The Si distribution coincides only in some regions with the position of the aluminides.

5.1.3 Al-Si alloys

The optical microstructures of as cast AlSi1.7 and AlSi12 are depicted in Figure 5.12a and b respectively. The AlSi1.7 material consists of α -aluminium phase with a small amount of eutectic Si phase along the grain boundaries. AlSi12 presents the α dendrites with interdendritic eutectic microstructure exhibiting a secondary dendrite are spacing of about 30 μm . which means that the alloy behaves hypoeutectically.

5.1.4 Al-Mg Alloys (5XXX series)

The optical micrograph and SEM image of AlMg (AW5083) alloy are depicted in figure 5.13a and b. These figures show Mn-rich precipitates and Fe-rich dispersoids aligned in rolling direction. The intermetallic compound and its composition in this alloy is shown in figures 5.14 and 5.15 with the ratio of elements approximately Al:Fe:Mn:Si= 15:2:1:1 corresponding to the molecular compound $Al_{15}(Fe,Mn)_3Si_2$ [20].

Mapping analysis in figure 5.16 depicts distribution of alloying elements in AW5083 alloy revealing some Mg_2Si which appear dark in the BSE image and black in the Al distribution picture.

5.1.5 Al-Mg-Si Alloys (6XXXseries)

Figure 5.17 a) shows an optical micrograph and b) a SEM image of the strip cast AW 6016CC, respectively. As can be seen the material is not homogeneous along the longitudinal section, a segregation line can be observed in the middle of the thickness. In picture 5.17 a) the oriented solidification towards the center can be observed exhibiting significant center segregation of AlFeSi phases with pores (black). Figure 5.18 a and b show inclusions in AW6016CC alloy at different positions and the ternary eutectic of AlFeSi- Mg_2Si -Al in the center. Figure 5.19 shows light optical microstructure of conventionally cast hot rolled AW6016DC, which is homogenous along the cross section. AW6008 alloy in figure 5.20 shows small particles which are distributed uniformly in the matrix.

5.1.6 Al-Zn-Mg Alloys (7XXXseries)

Figure 5.21a and b show optical micrographs of AW7349 in homogenized condition (1C-A) and as cast (1C-B), respectively. Optical micrograph of AW7349 (1C-B) shows some porosities and segregations. Precipitates can be observed in the SEM image of this alloy (figure 5.22). Mapping analysis in figure 5.23 depicts the distribution of alloying elements of AW7349 (1C-A) alloy. Most of the inclusions are rich in Cu, Zn and Mg, some particularly rich in Mg. Sc distribution is related to that of Zr indicating primary $Al_3(Zr,Sc)$.

5.2 Hardness of samples

5.2.1 AlGe, AlGe3 alloys

Figure 5.24a and b show Brinell hardness of the AlGe and the AlGe3 alloy in different conditions. The word “t” in front of number means test. Condition of t40 (test forty) is heated to

430°C/30 min + w.q., and then to 415°C with 5K/min heating rate and cooled to room temperature with 5K/min and this cycle is repeated 3 times and then the hardness is measured.

This method was used for t 45, t 41 and t 46. After 7 days means that after doing the test, the sample was held at room temperature and hardness measured again after 7 days. There is actually no precipitation hardening effects at RT. The as cast condition exhibits the largest hardness followed by t45 and after 7 days RT there after for AlGe and AlGe₃, respectively.

5.2.2 Al-Mg-Si 6XXX series (6016CC,6016DC)

Figure 5.25 shows the comparison of hardness values of specimens in as delivered condition, before DSC experiments and after the last DSC cycle which means solution treatment by heating up to 550°C and cooling down at different rates. T6 yields the highest hardness followed by W.Q and T1. The hardness of the strip cast CC6016 is always little less than that of the conventional DC6016. The compared WH (cold rolled condition) is even less in hardness. The DSC cycles perform an annealing treatment little less efficient with the higher cooling rates.

5.2.3 Al-Zn-Mg Alloys 7XXXseries

Figure 5.26 shows the comparison of hardness values of AW7349 (1C-A, B) in different conditions: “1C-A” is homogenized 1C-B is as cast and the condition of test 202 is that heating with 100K/s to 350°C and holding at that temperature for 16 hours. The hardness of the as cast and the homogenized condition is almost the same, whereas test 202 produced an annealed condition.

5.3 Calorimerty

5.3.1 Differential scanning calorimetry of AlGe and AlGe₃ alloys

Figure 5.27 depicts DSC thermograms of AlGe and AlGe₃ alloys. As shown in the figure an exothermic effect starts around 230°C and finishes at 280°C for AlGe alloy, and starts at 150°C for AlGe₃ and finishes as well at 280°C. Comparing these two graphs, the exothermic effect starts at lower temperature for AlGe₃ and the endothermic effect is extended to higher temperature exhibiting the shape of a double peak.

5.3.2 Differential scanning calorimetry of AlSi1Ge5 and AlSi11Ge5 alloys

Figure 5.28 depicts DSC runs of AlSi1Ge5 and AlSi11Ge5 alloys in different thermal conditions. As depicted in the figure an exothermic effect for the as cast AlSi1Ge5 condition starts from the beginning and finishes at 350-400°C, and in W.Q condition the exothermic effect is between 150°C to 320°C. The exothermic effect for AlSi11Ge5 is smaller and at higher

temperatures between 230°C to 320°C. The W.Q conditions show a clear endothermic effect around 350°C.

5.3.3 Differential scanning calorimetry of AlSi1.7 and AlSi12 (AC4XXseries.)

Differential scanning calorimetry of AlSi1.7 and AlSi12 is shown in figure 5.29. As shown in this figure for AlSi1.7 we can see an exothermic peak which starts at 170°C and finishes at 325°C, the exothermic peak, for AlSi12 starts at 200°C and finishes at 375°C. These graphs show that the temperature interval, where the exothermic peak temperature in the eutectic alloy moved from 250°C to 280°C. There is no clear endothermic effect observed.

5.3.4 Differential scanning calorimetry of Al-Mg-Si alloys of AW6XXXseries

Figure 5.30 shows the DSC runs of AW6016 DC alloy in W.Q condition. Four peaks have been recognized, two endothermic and two exothermic peaks. The first endothermic peak for 5K/min appears at about 175°C (peak I), two exothermic peaks follow (II;III), and after them one large exothermic peak (IV) can be observed. The two exothermic peaks for 5K/min were centred around 230°C (peak II), 280°C (peak III). As we see in these figures the peaks I;II;III are shifted to higher temperatures for the higher heating rate by about 10K. The higher heating rate produced almost twice as big signals. The final endothermic peak extends from about 380°C to 500°C (IV) for both heating rates. And its enthalpy change correlates with the heating rate difference. In figure 5.31 the two kinds of 6016DC and 6016CC are compared with each other, showing almost the same curves, peak I is slightly bigger for the DC sample and peak II,III about 10K earlier than the for the CC samples. The endothermic peak IV starts about 15K earlier for the CC version than for DC.

DSC graphs of AW6008 alloy are depicted in figure 5.32. Different heat treatments show different exothermic and endothermic peaks. AW6008 W.Q + RT (T4) shows a clear endothermic peak I and the exothermic peak II and III can be recognized. There are two endothermic peaks, one from 320°C – 460°C (IV) and another peak V is around 510°C. The as received condition dose not show peak I and only one exothermic peak is around 260°C. The endothermic peak (V) at 490°C is much more pronounced than the one around 380°C (IV) in all conditions except W.Q.

Condition T104 is a special heat treatment to simulate the temperature history of the heat affected zone of a welded sample. The sample was heated from room temperature to 60°C in 1s and further to 250°C in 2s, then to 410°C in 2.5s where it stayed for 3.5s when it was cooled to 260°C in 10s and further in 18s to 180°C then in 24s to 150°C and after that in 25s to 100°C.

The thermogram of T104 condition is very similar to that of the as received condition. After some room temperature aging a small peak (I) appears for T104 samples. There is a difference in the base line of those thermograms.

5.3.5 Differential scanning calorimetry of Al-Zn-Mg alloy (7XXX series)

Figures 5.33 shows DSC graphs of homogenized AW7349 (1C-A) with different heat treatments, starting immediately after solution treatment at 480°C/20min (W.Q) producing different exothermic and endothermic peaks. In this alloy in W.Q conditions, four relative minima are observed, at 150°C to 180°C (2), 180°C to 220°C (3), 225°C to 230°C (4), and around 250°C (5). Also relative maxima appear one around 120°C (1) and a large endothermic peak from 270°C to 450°C (6). In T4 condition we can see a large endothermal peak (1) around 120°C compared to that immediately after solution quenching. The minima are qualitatively at the same temperatures in both W.Q conditions and the area of the exothermic effects is almost the same as that of endothermic effect (6). After T6 treatment (120°C/24hr) the endothermic peak moves to 200°C, the exothermic peaks disappear except number 5. The endothermic peaks (6) is the same for all these conditions.

5.4 Dilatometry

5.4.1 Dilatometry of AlGe, AlGe₃, AlSi1Ge₅, AlSi11Ge₅ alloy

Instantaneous coefficient of thermal expansion (CTE) of the AlGe alloy in differently cooled condition as function of temperature is depicted in figure 5.34 for the same heating rate of 5K/min. Two kinds of peaks were observed during heating the sample from quenched (W.Q) condition. (C1) shows a relative maximum at 270°C and a relative minimum at 320°C. After cooling with 5 or 1K/min from solution temperature of 430°C (C2, C3) and heating of 5K/min, the CTE curves don't show any peaks. But with heating rate of 1K/min, a small deviation of the CTE (T) curve can be observed similar to that in the W.Q condition as depicted in figure 5.35 (C3). Figure 5.36 shows the percent linear change (PLC) of AlGe₃ and AlGe in W.Q condition compared with pure Al. Figure 5.38 shows a strong peak at 250°C for the as quenched W.Q condition of AlGe₃. Sample was cooled at 5K/min from 280°C and the following heating cycle exhibits a minimum from 250°C to 400°C. When cooled from 430°C at 5K/min the CTE curve shows a maximum around 320°C followed by a minimum at 375°C. The effect of holding time at room temperature was investigated on the AlGe₃ alloy after dilatometry. As shown in figure 5.39 we can't see any difference of CTE curve with respect to the third cycles in figure 5.38 but in the second cycle in figure 5.39, the maximum is smaller and moved to a lower temperature

(around 300°C). in figure 5.37, the relative change between this maximum and the following minimum looks very similar.

Effect of cooling rate on AlSi1Ge5 alloy is shown in figure 5.40. After quenching a similar peak appears as in figure 5.38 followed by a decrease. Changing the cooling rate from 5 to 20K/min didn't influence the CTE (T) curve significantly which is similar to CTE (T) curve for AlGe3 after 5K/min cooling.

Figure 5.41a and b show the response of AlSi11Ge5 alloy to different solution treatments. As depicted in these figures the higher solution treatment shows a CTE peak at 250°C after quenching from 480°C, but a smaller peak around 280°C after quenching from 415°C. The second cycles displaces the maximum to higher temperatures. The sample of figure 5.41b was heated to 480°C yielding CTE (T) peak of similar height as in the condition quenched from 430°C. The effect of the different cooling rate is similar to that in figure 5.41a. The increase in solution treatment temperature increases the peaks and displaces them to lower temperatures. Cooling rates smaller than water quenching displace the CTE(T) peak to 310°C for both solution treatment temperatures.

5.4.2 Dilatometry of Al-Mn alloy (3XXXseries)

Figure 5.42a and b show CTE(T) curves of Al-Mn alloy (AW3003) in different conditions of solution treatment. As depicted in figure 5.42a, there is only a small deviation between the first and second cycle, but this deviation is bigger in figure 5.42b and occurs between 280°C to 400°C. The CTE (T) of the water quenched conditions differs between each other as shown in figure 5.42c, but there is little difference with respect to pure Al: < 1ppm/K smaller 350°C, +1ppm/K at 470°C.

5.4.3 Dilatometry of AlSi alloys (4XX series)

Different solution heat treatments of different AlSi alloys (AlSi1.7, AlSi12) show different CTE (T) curves, see figure 5.43a and b. Comparing different cycles of the CTE(T) curve of AlSi 1.7 (figure 5.43a) the sample quenched from 540°C, shows a peak with a shoulder already at 260°C which shifts about 90°C for the lower solution temperatures. The 350°C peaks after 480°C and 450°C quenching temperatures coincides with the intersection of the CTE(T) of the sample solutionized at 540°C with the CTE(T) of pure Al. The CTE(T) of the other samples drops below pure Al only above 400°C. The CTE(T) peaks for the AlSi12 alloy in figure 5.43b shift from 280°C to 320°C with decreasing solution treatment temperature. The CTE(T) registered with 50K/s heating rate serves as reference instead of pure Al showing that the CTE of

AlSi12 registered at 5K/min drops below that at about 380°C. Table 5.1 compares the length change of both AlSi alloys during heating after solution quenching from different temperatures with that calculated according to the solubility changes. Figure 5.44a and b show the isothermal change in length after W.Q condition and fast heating at 50 K/s to 540°C for AlSi1.7 and AlSi12. the shrinkage at 540°C is for both alloys the same corresponding to the Si precipitation during fast heating.

5.4.4 Dilatometry Al-Mg alloy (5XXX series)

The CTE curve of AlMg alloy (AW5083) is given in figure 5.45. It confirms that the CTE of Al is increased by alloying Mg. As indicated in this figure there is a slight deviation between first and second cycle around 300°C and 500°C. The result of isothermal dilatometry of this alloy at 200°C and 300°C are depicted in figure 5.46a and b. During isothermal holding at 200°C there is an expansion of about $5 \cdot 10^{-5}$ in length within 8 h. There occurs a corresponding contraction of $-6 \cdot 10^{-5}$ at 300°C within 6h afterwards.

5.4.5 Dilatometry Al-Mg Si alloys (6XXX series)

Figure 5.47 shows the coefficient of thermal expansion of AW6016CC and DC in W.Q condition. Both curves are the same and have a maximum peak at 300°C, Comparing the CTE(T) of alloy AW6008 in W.Q and T104 (heat affected zoon simulation) in figure 5.48a and b we can see a much smaller relative maximum in CTE(T) in the first heating around 250 to 270°C and we can't see any difference in all curves between 300 to 400°C. About 460°C, there is a minimum in all CTE(T) curves, which is more pronounced during the first heating then in the second. This minimum lies 1ppm/K lower for the T104 condition than for the as received condition. Figure 5.48c compares first heating of as received and T104 condition. Dissolution peaks (5) are more or less the same.

5.4.6 Dilatometry of Al-Zn-Mg alloys (7XXX series)

The CTE(T) graphs of the homogenized Al-Zn-Mg alloy (AA7349 1C-A) in different conditions of heat treatment can be observed in figure 5.49. We can see five extrema, one positive 75 to 150°C in T4 conditions, three relative minima at 160°C, 210°C and 250°C, an accelerated expansion between 280°C and 450°C. In W.Q +RT(3 weeks) condition (T4), peak 1 is increased compared to the as quenched condition. In T6 (120°C/24 hr) condition; there is a maximum peak at 175 to 200°C (between the numbers 2,3) and the minimum at 250°C (number 4) is pronounced,

5.5 Metallography pictures



Figure 5.1.(a) Light optical micrograph of Al-Ge as cast alloy showing some porosities

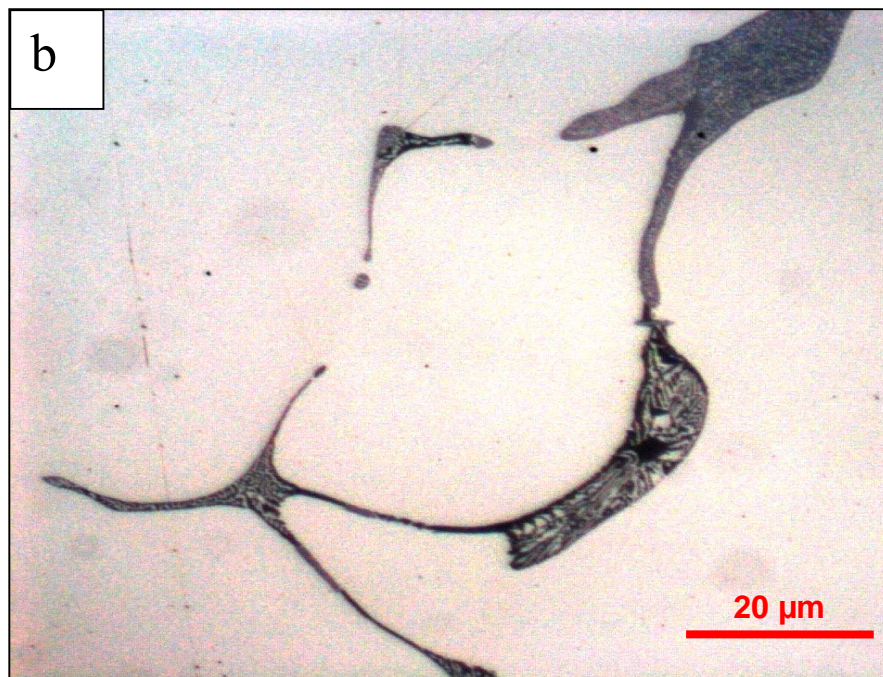


Figure 5.1 (b) Light optical micrograph of Al-Ge as cast alloy showing interdendritic eutectic Al-Ge

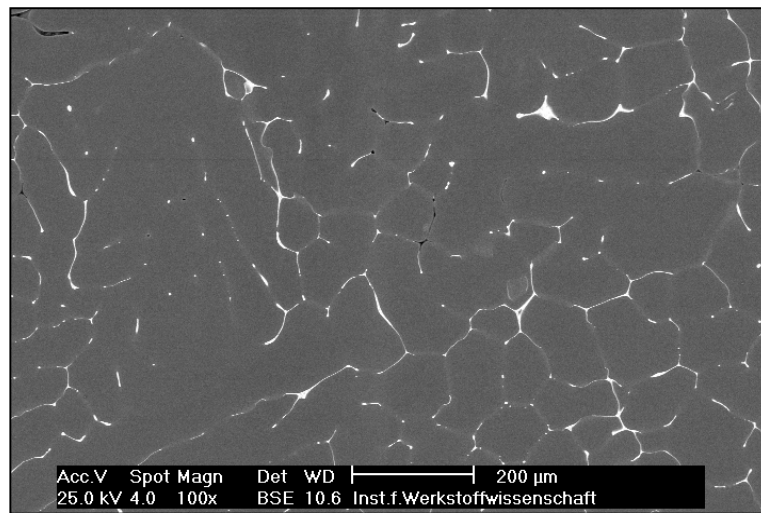


Figure 5.2 BSE image of AlGe showing Al-Ge (white) decorated grain boundaries in as cast condition

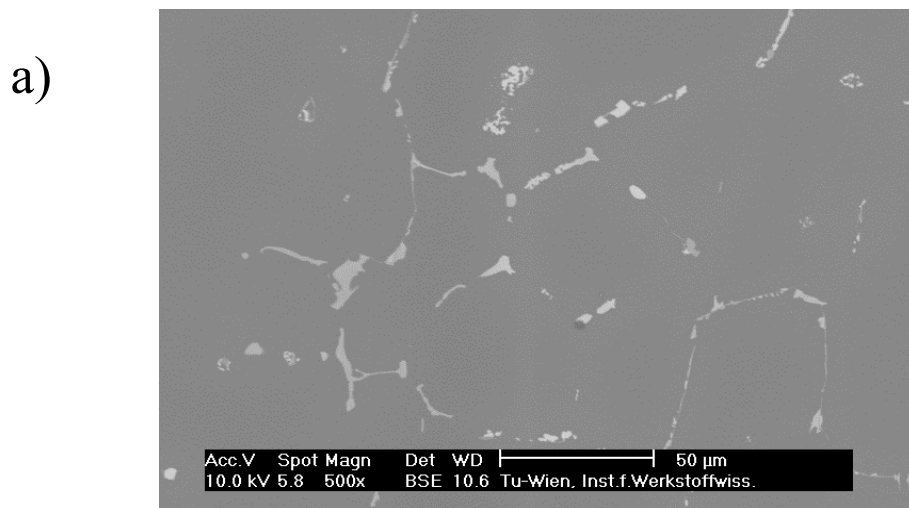


Figure 5.3 a) BSE image of AlSi1Ge5 after solution treatment at 450°C slowly cooled to 415°C.



Figure 5.3 b) Light optical micrograph of Al Si1Ge5 with low Si content in as cast condition.

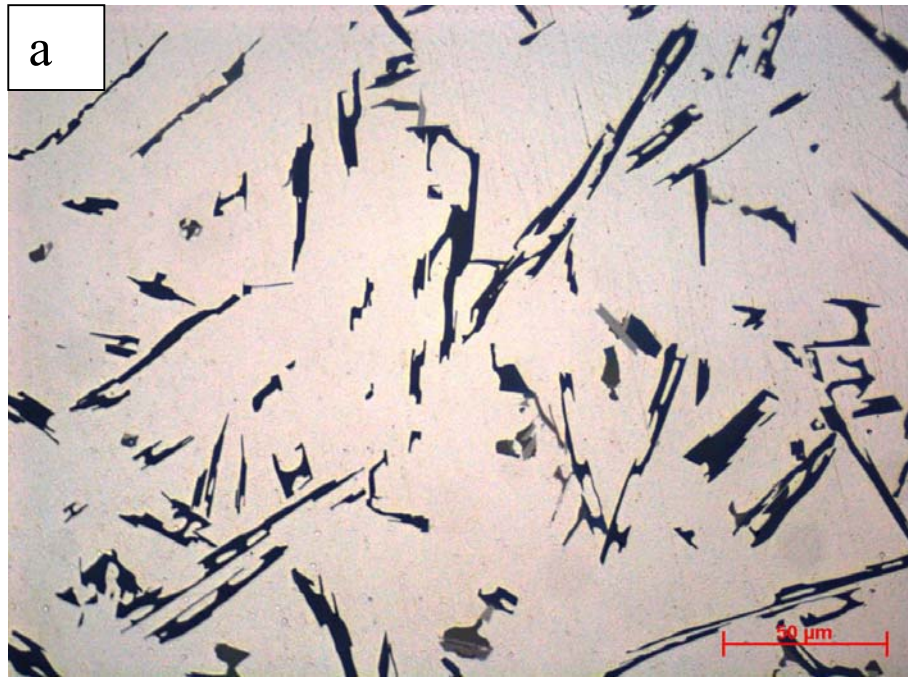


Figure 5.4 a) Light optical micrograph of AlGe5Si11 with black and grey inclusions.

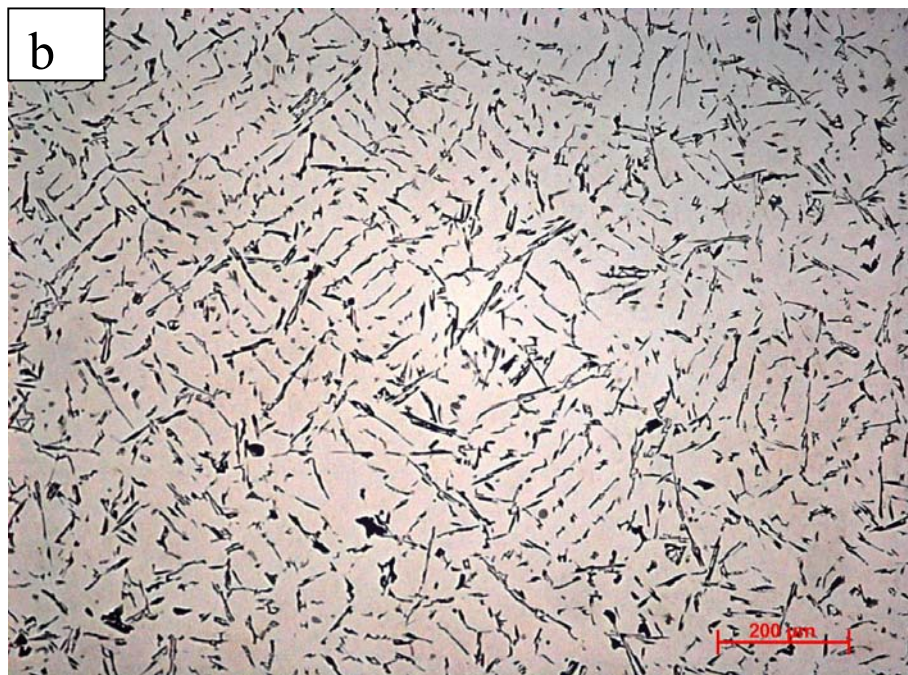


Figure 5.4 b) Light optical micrograph of AlGe5Si11 showing a dendritic structure and interdendritic, needle like inclusions.

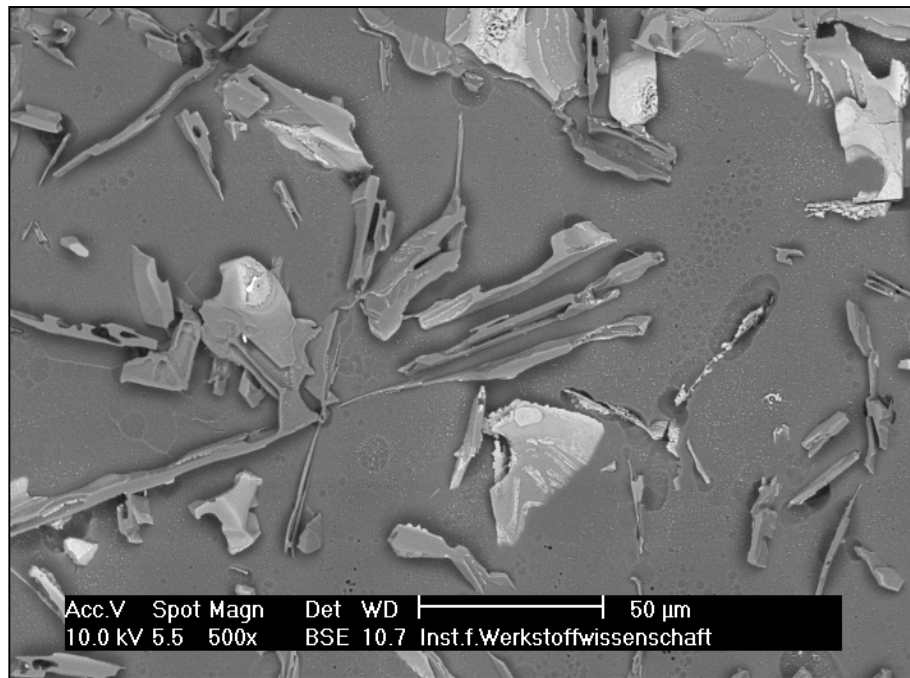


Figure 5.5 BSE image showing white and grey platelets in AlSi11Ge5 alloy (deep etched)

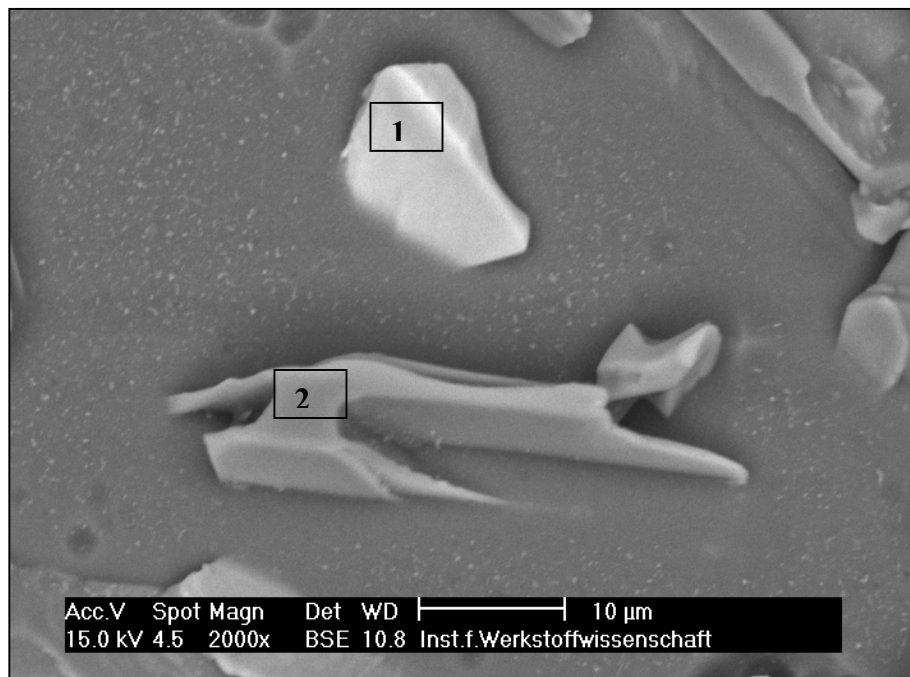
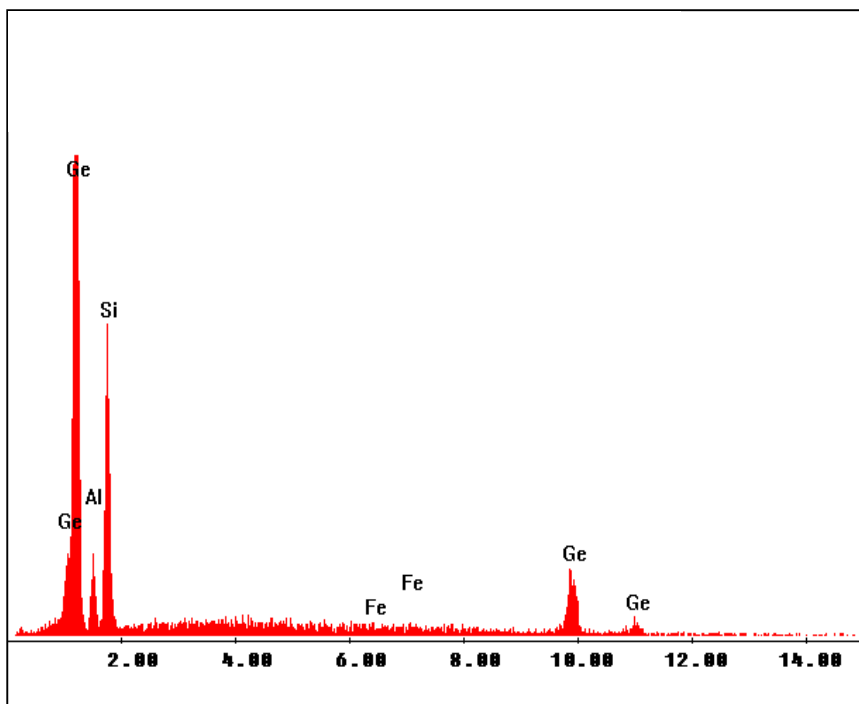
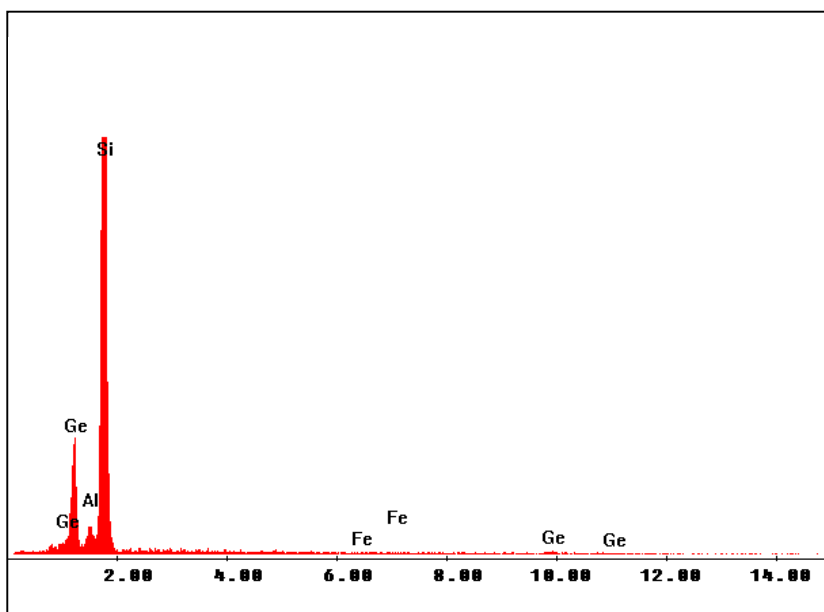


Figure 5.6 BSE image of deep etched sample showing white and grey particles in AlSi11Ge5 alloy with higher magnification.



Element	Wt %	At %
GeL	67,14	44,75
AlK	6,25	11,21
SiK	24,51	42,22
FeK	2,1	1,82
Total	100	100

Figure 5.7 EDX Analysis of particle “1” of figure 5.6 (Ge:Si ~1:1 at%)



Element	Wt %	At %
GeL	15,8	6,79
AlK	2,61	3,02
SiK	80,91	89,82
FeK	0,68	0,38
Total	100	100

Figure 5.8 EDX Analysis of particle “2” of figure 5.6 (Ge:Si~1:13 at%)

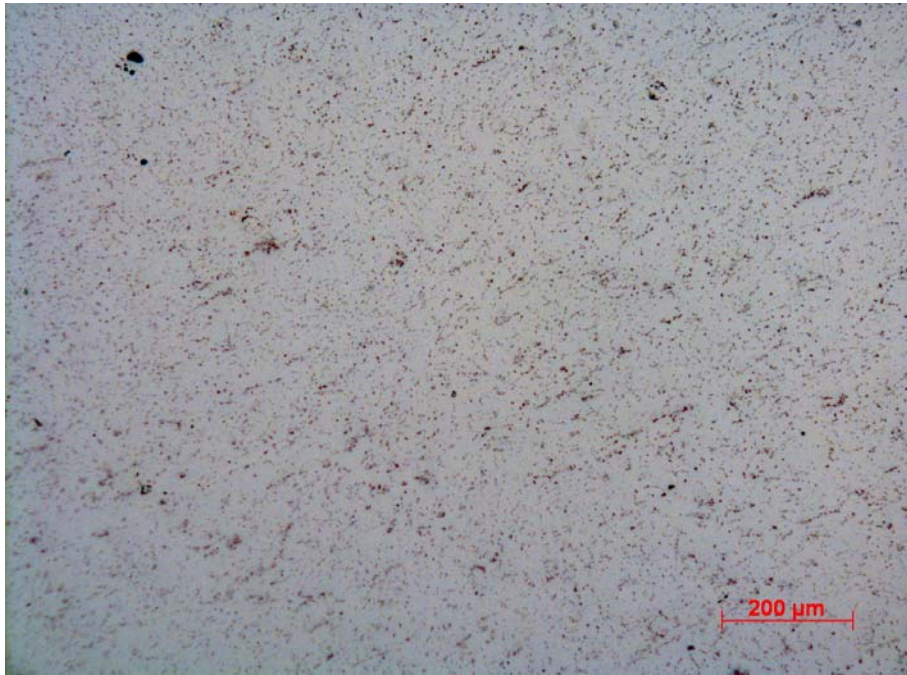


Figure 5.9 Light optical micrograph of Al-Mn alloy (AW-3003) with pores (black) and inclusion (dark).

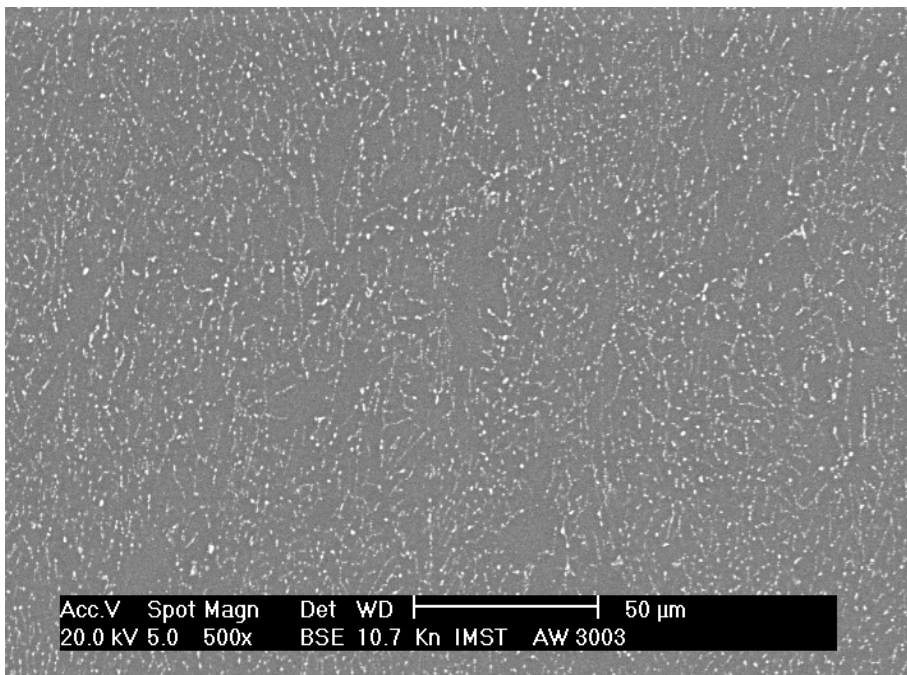


Figure 5.10 BSE image showing particles in Al Mn alloy (AW-3003) some decorating grain boundaries

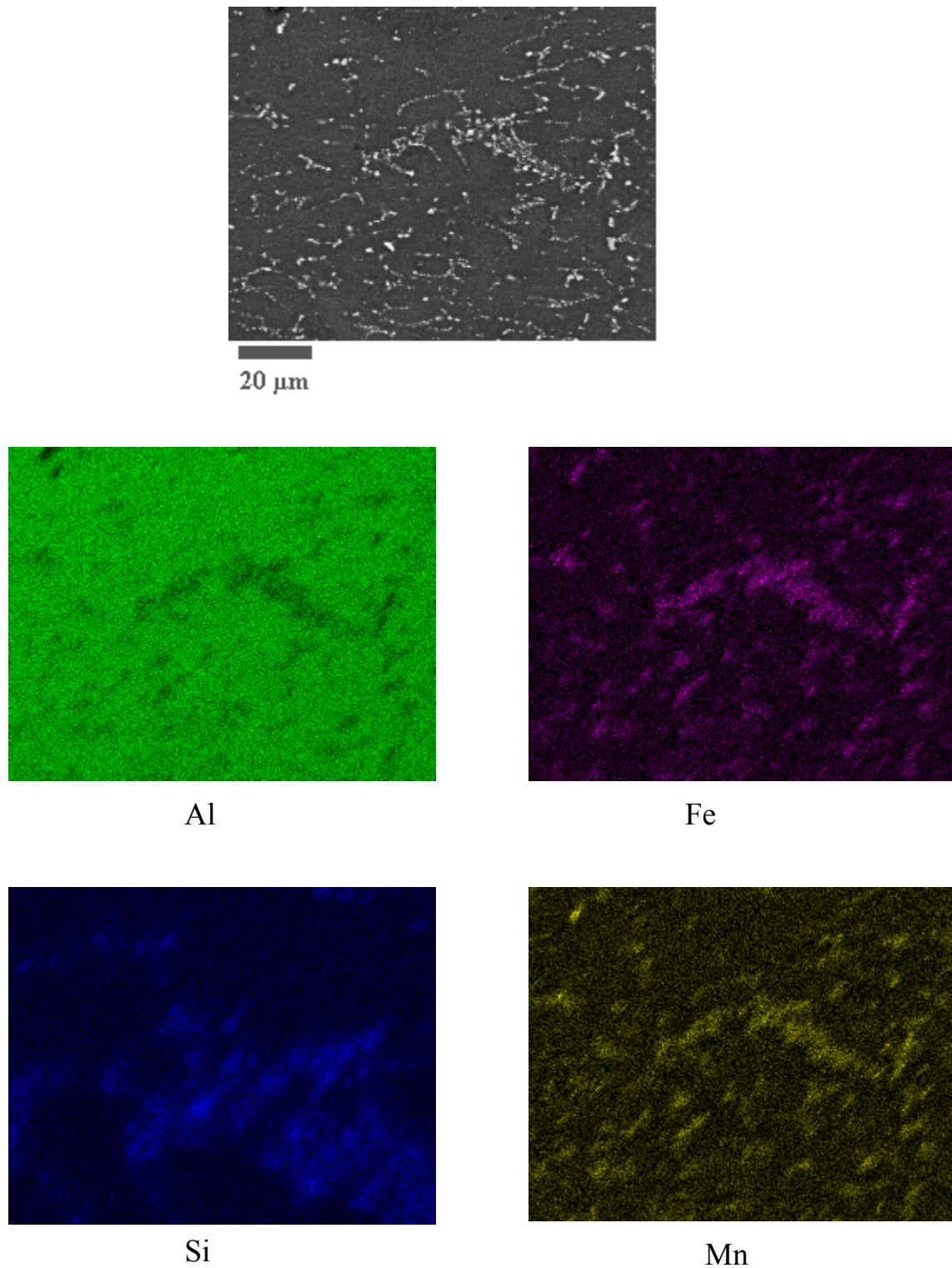


Figure 5.11 Mapping of Al-Mn alloy (AA3003) for the elements Al, Mn, Fe and Si revealing that most of the particles shown in the BSE image are Fe-Mn aluminides. The Si cannot be correlated.

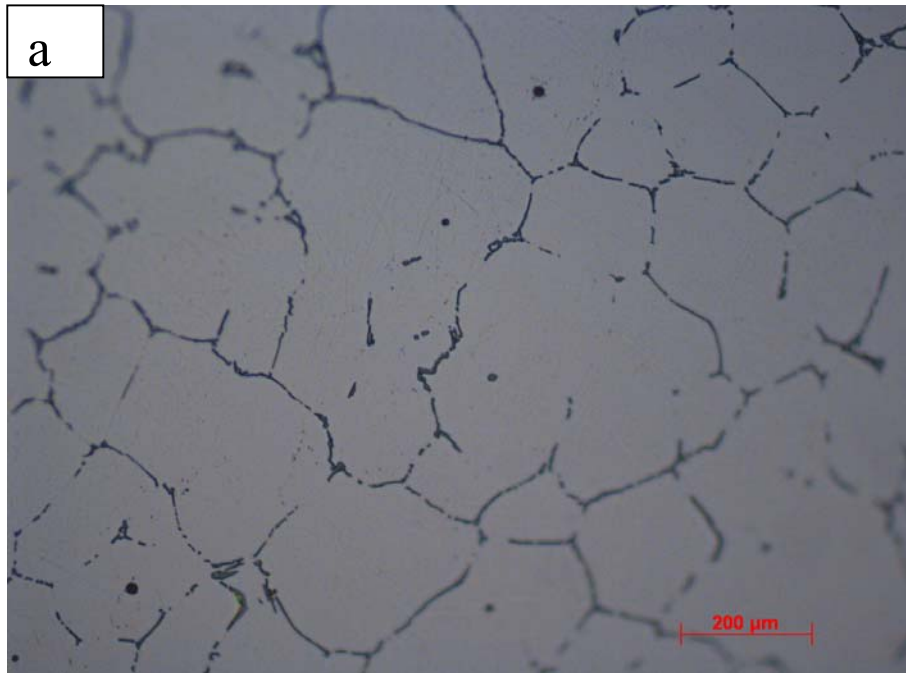


Figure 5.12 Microstructure of a) AlSi1.7 showing little interdendritic eutectic b) AlSi12 as cast condition (α -Al white, eutectic Al-Si structure, dark).

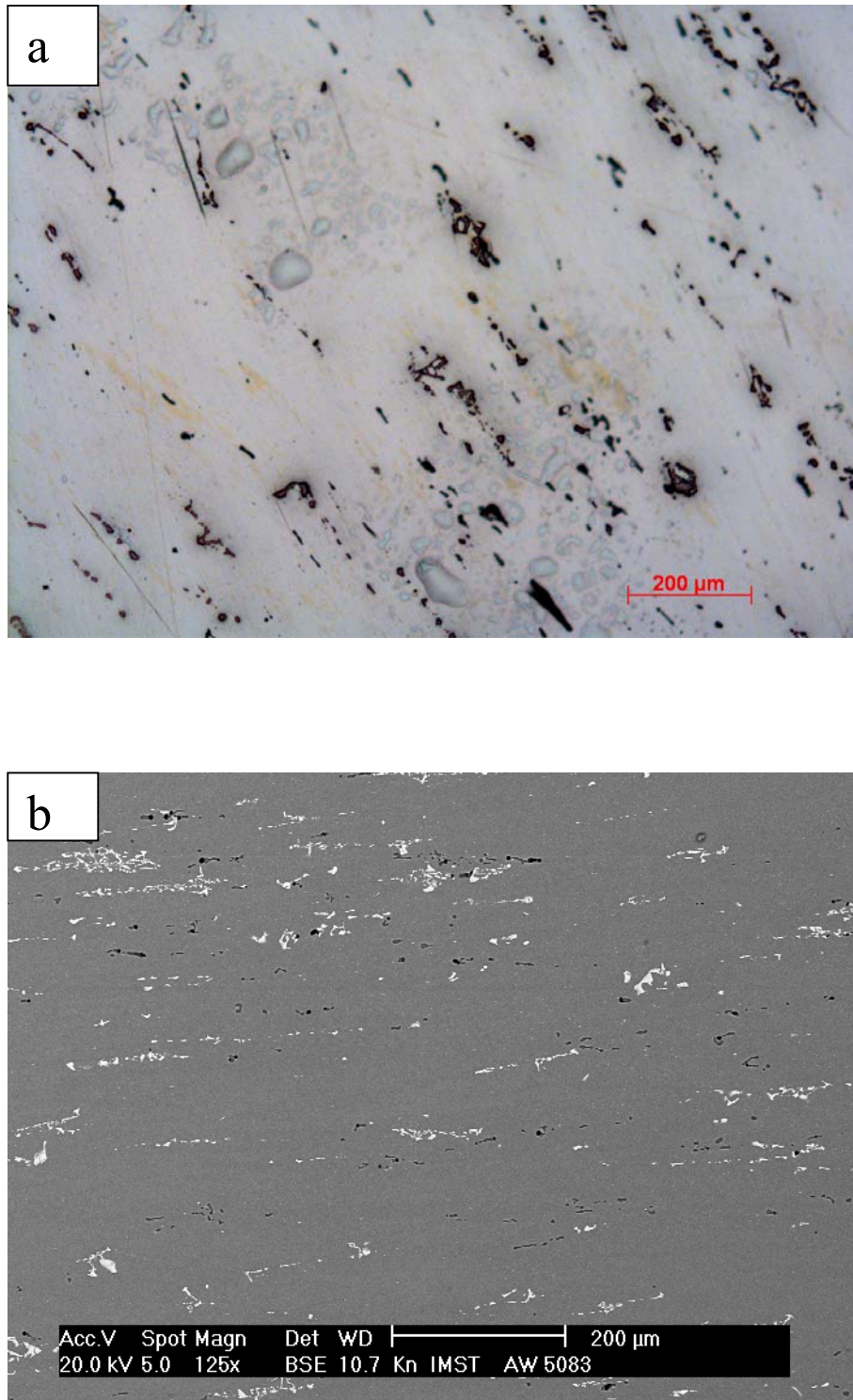


Figure 5.13 a) Optical micrograph of hot rolled AW5083 showing aligned inclusions and some contamination
b) BSE image revealing Fe-aluminides (white) and Mg-rich (dark) inclusions.

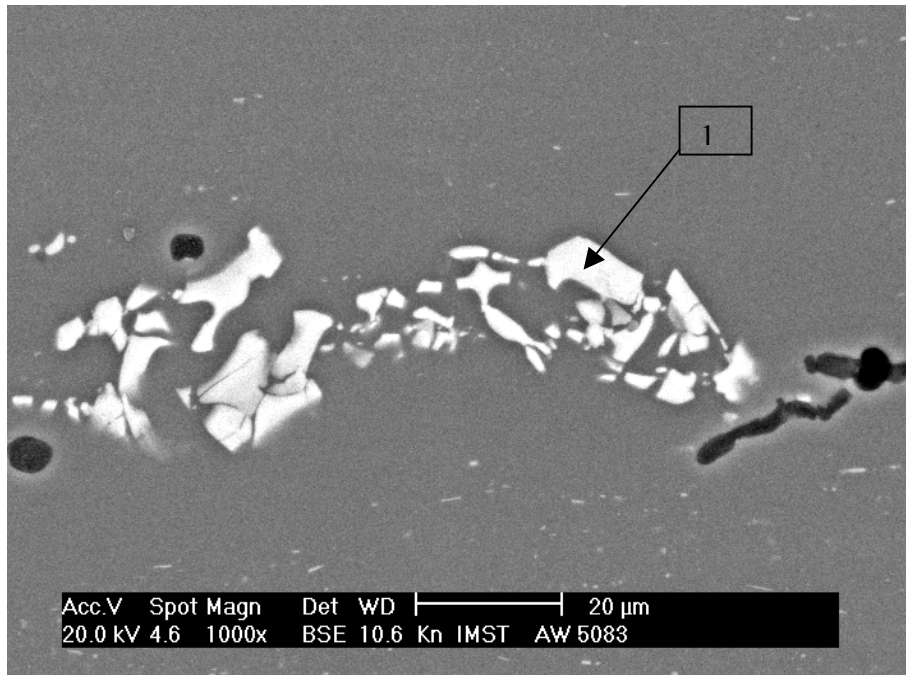


Figure 5.14 BSE image showing intermetallic compound

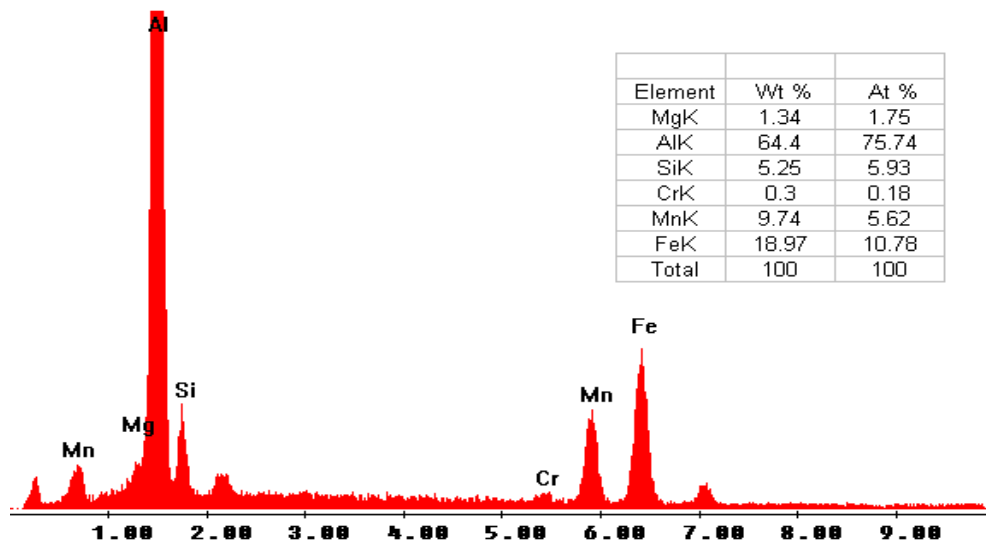


Figure 5.15 EDX Analysis of white particle “1” of figure 5.14 corresponding to $Al_{15}(Fe,Mn)_3Si_2$

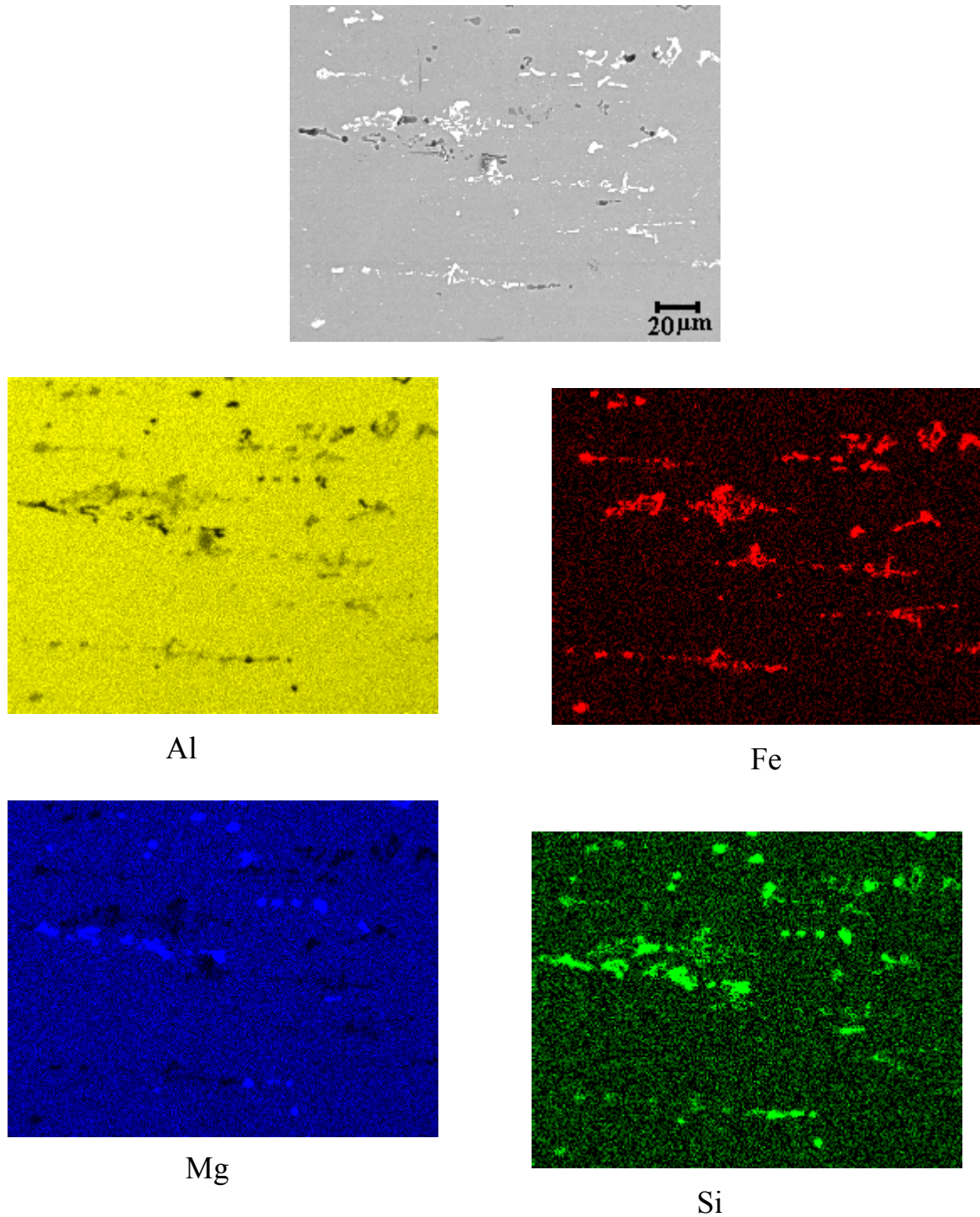


Figure 5.16 Mapping of AW5083 alloy in the BSE picture, where bright particles are AlFeSi phases and grey are Mg₂Si particles, which appear black in the Al distribution picture.

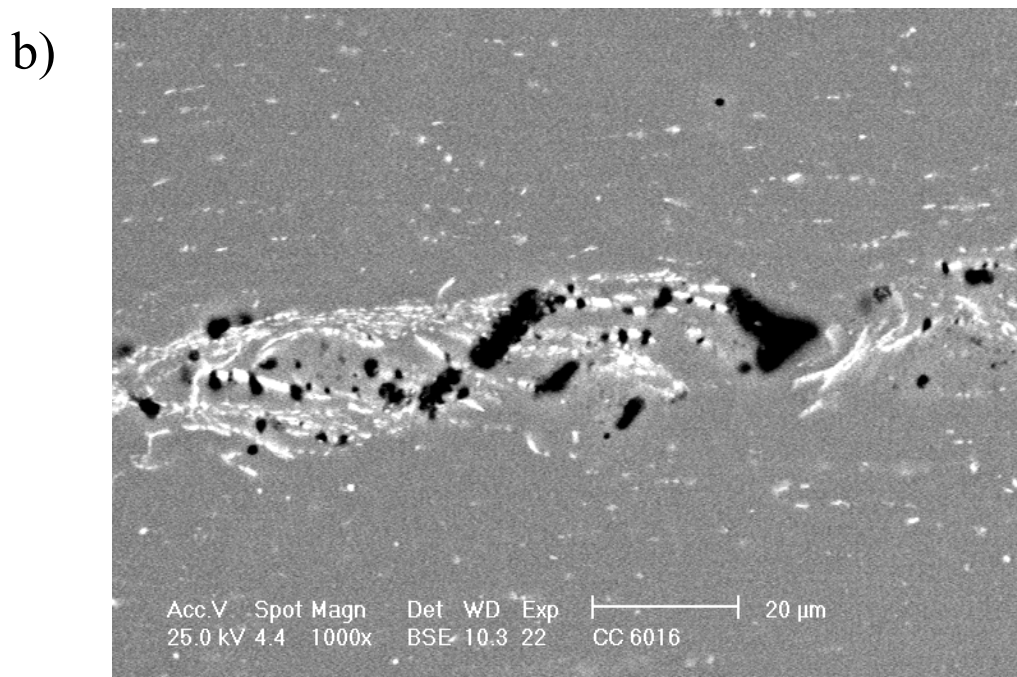
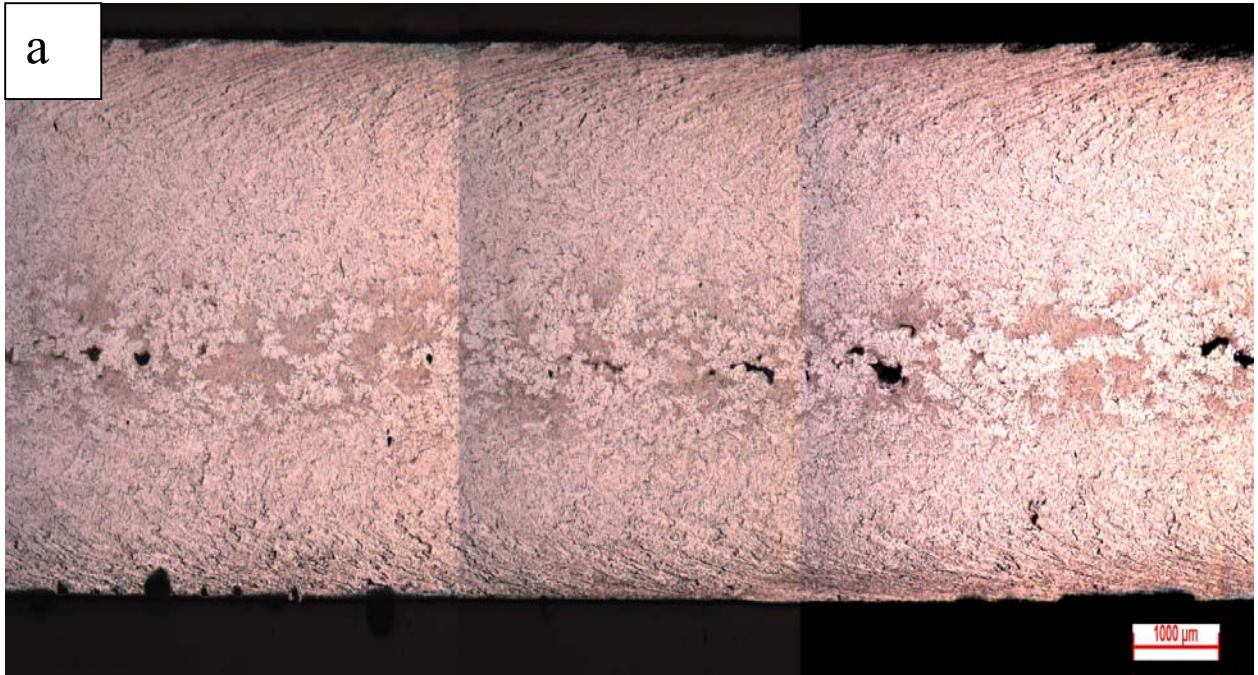


Figure 5.17 AW6016CC a) Light optical micrograph and b) BSE image of the center segregation with pores.

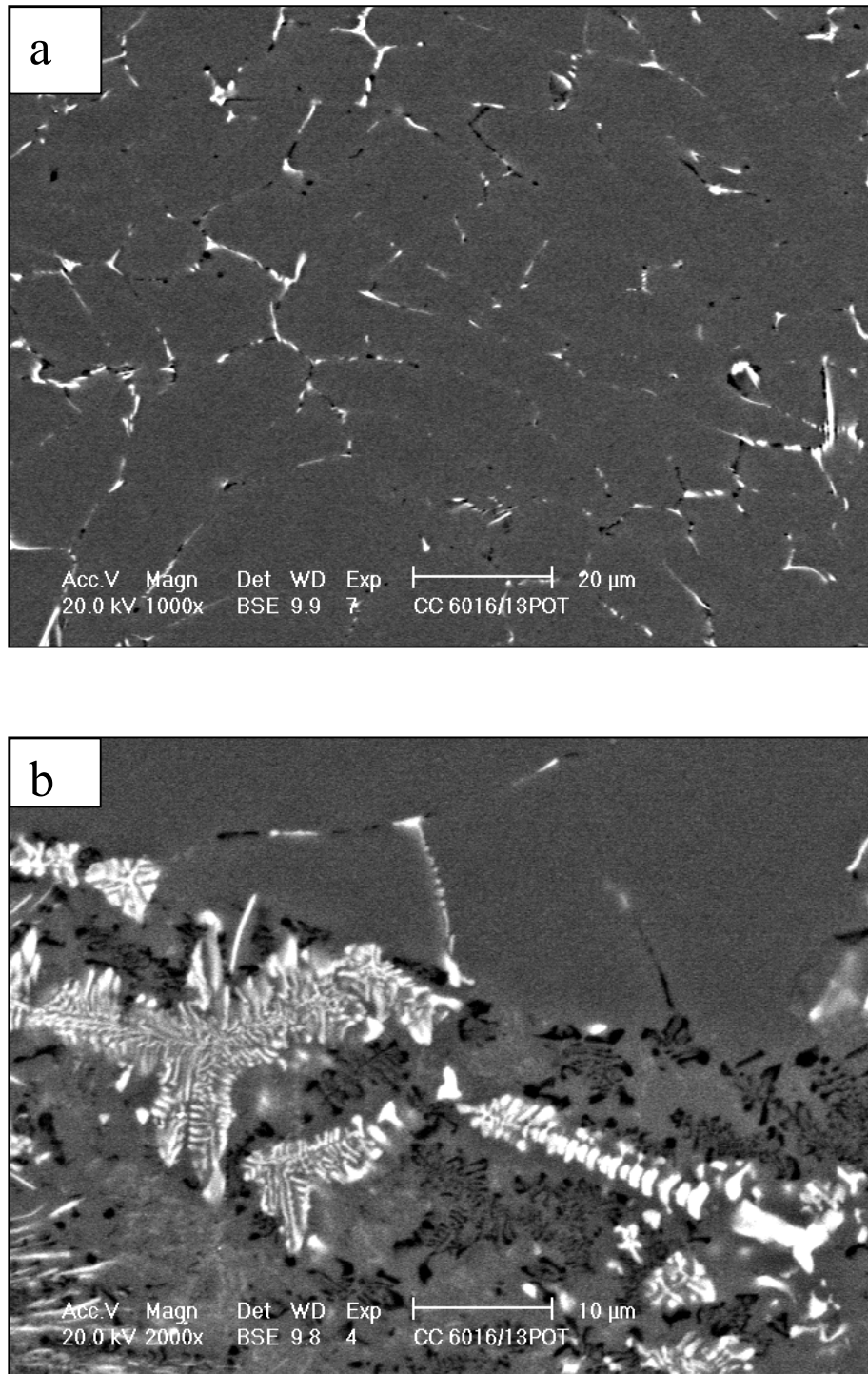


Figure 5.18 Light optical images of AW6016CC a) shows precipitation clusters at $\frac{1}{4}$ of the thickness and b) the central segregation line with Al-Fe eutectic (white) and Mg₂Si (dark).

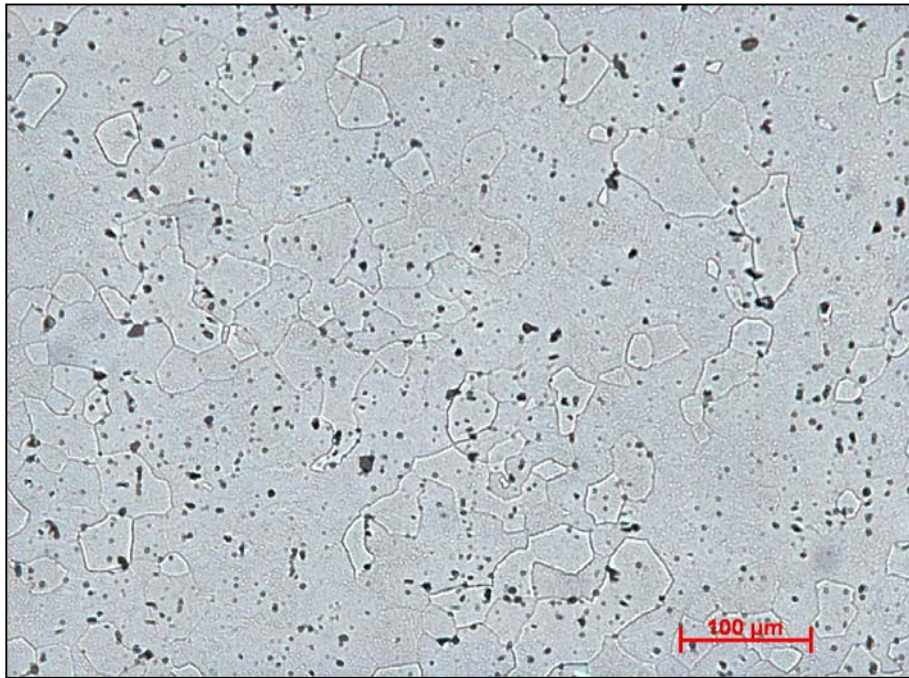


Figure 5.19 Light optical micrograph of AW6016DC the material is homogeneous with evenly distributed inclusions.



Figure 5.20 Light optical micrograph of a cross section of extruded AW6008 with particles evenly distributed in the matrix.

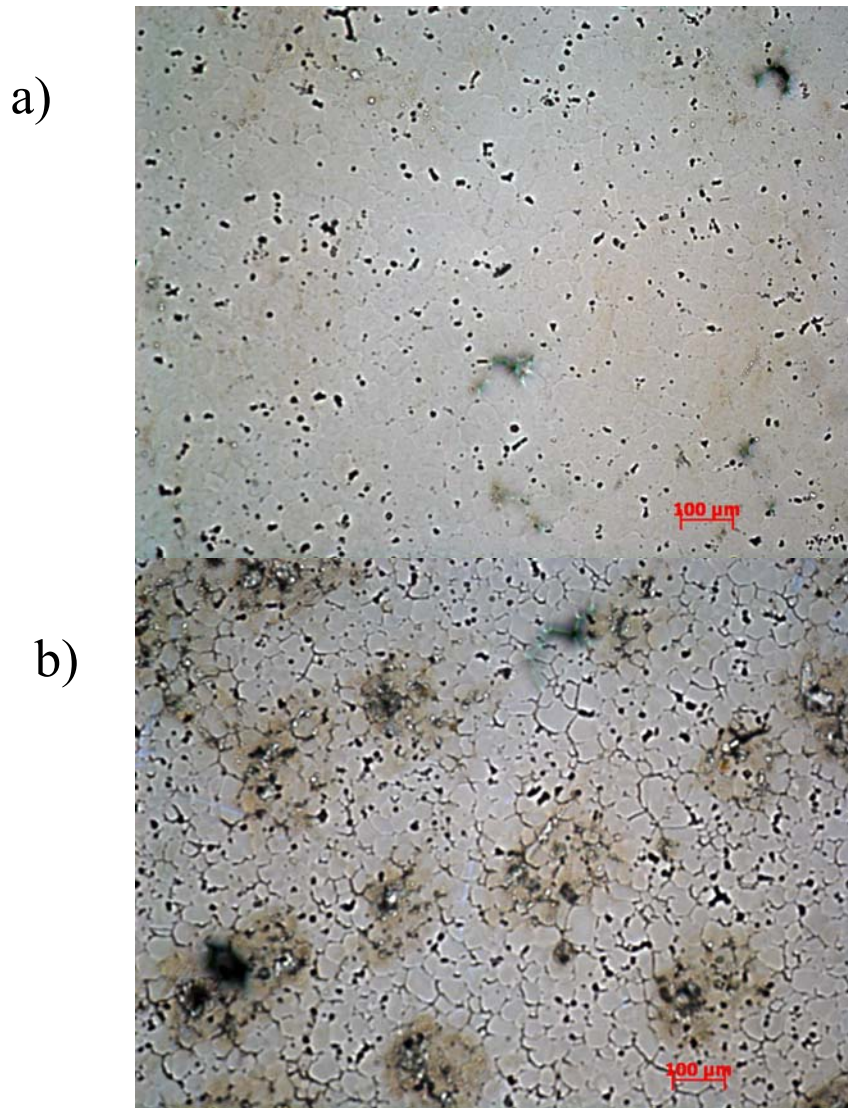


Figure 5.21 Light optical micrograph of AA7349 a) homogenized (1C-A) with casting porosity and dispersoid. b) Al7349(1C-B) as cast with segregation.

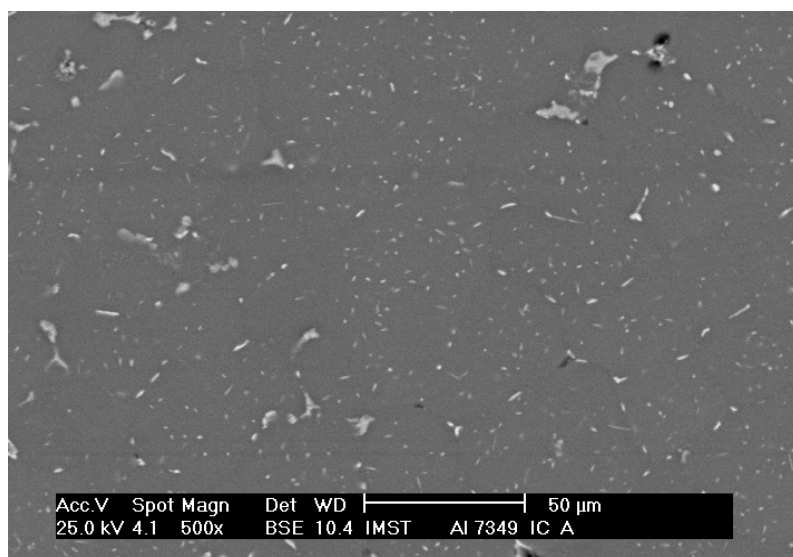


Figure 5.22 BSE image of AA7349 homogenized (1C-A)

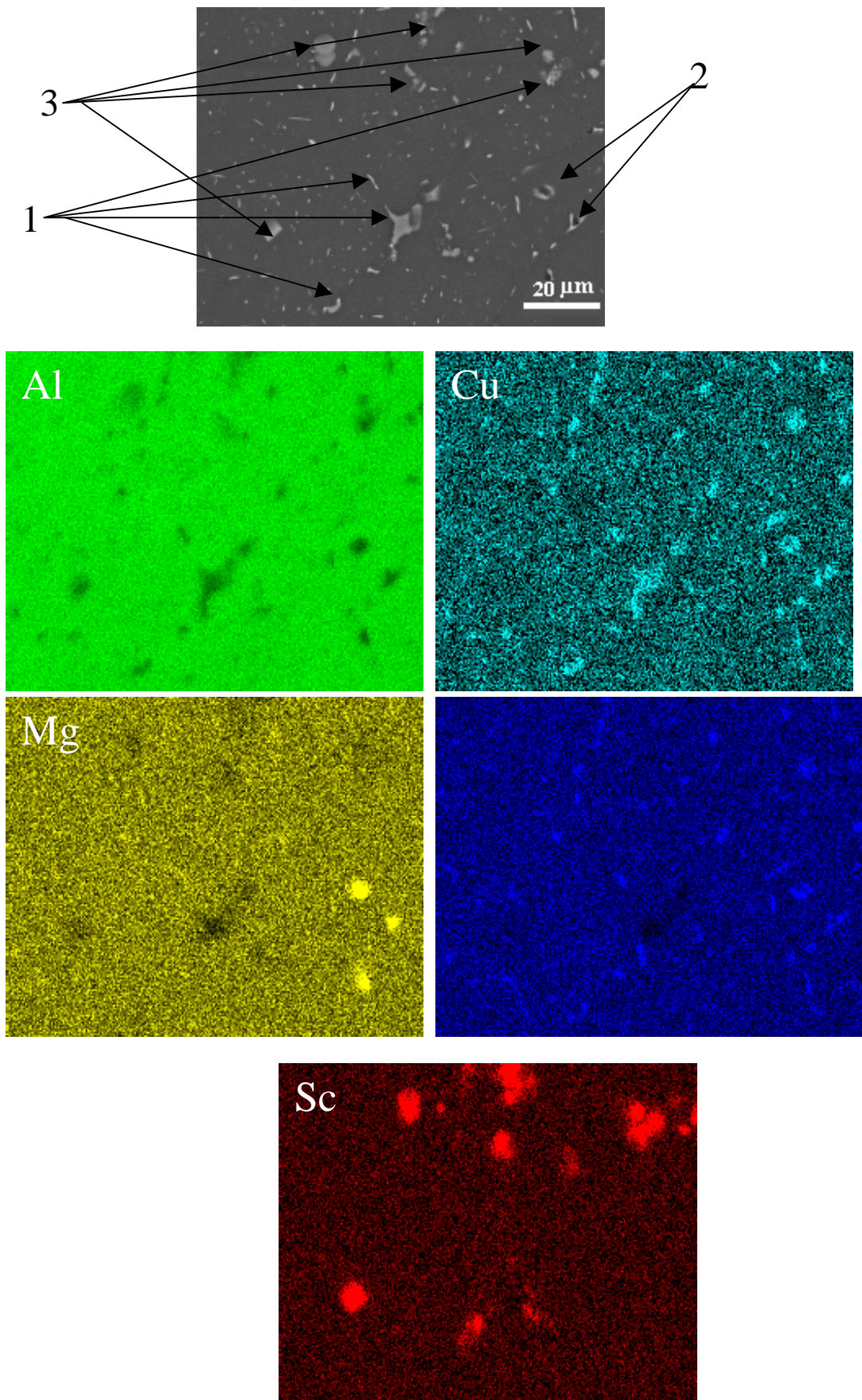


Figure 5.23 Element mapping of homogenized AW7349 (1C-A) indicating Cu and Zn-rich(1), as well as Mg-rich (2) dispersoids and primary $Al_3(ZrSc)$ inclusions (3)

5.6 Hardness graphs

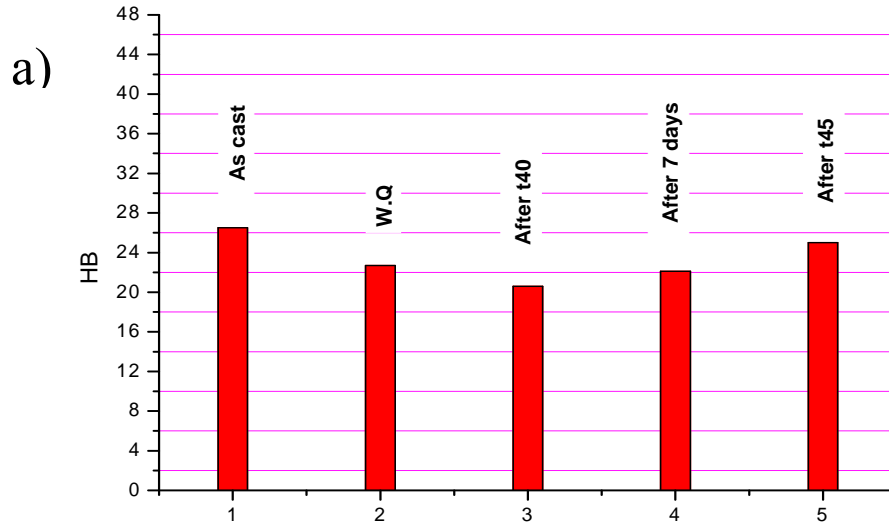


Figure 5.24 a) Brinell hardness of AlGe alloy in different conditions

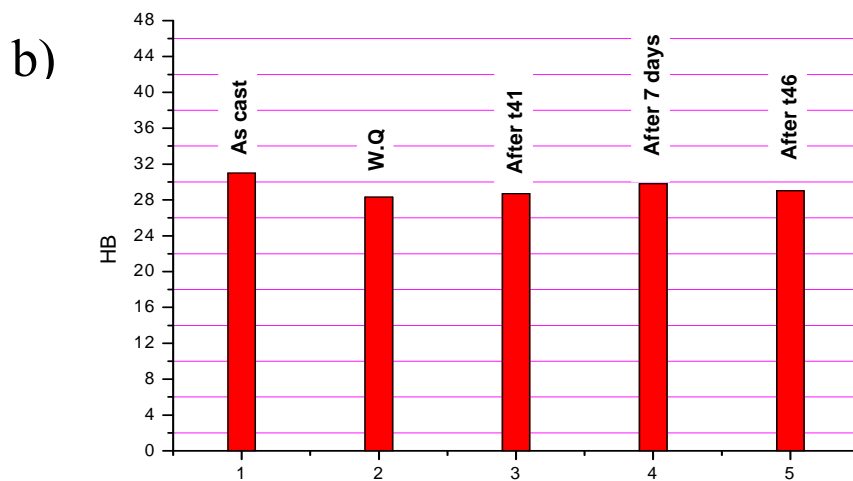


Figure 5.24 b) Brinell hardness of AlGe3 alloy in different conditions

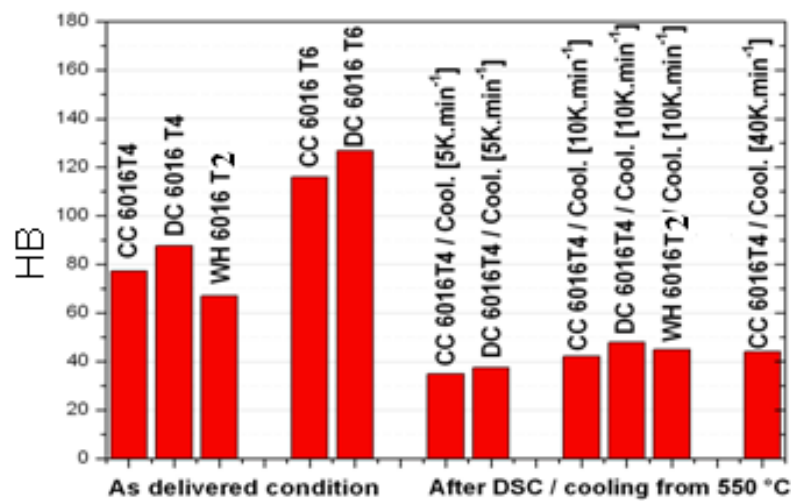


Figure 5.25 Brinell hardness of AW6016CC, DC in different conditions (WH = cold rolled).

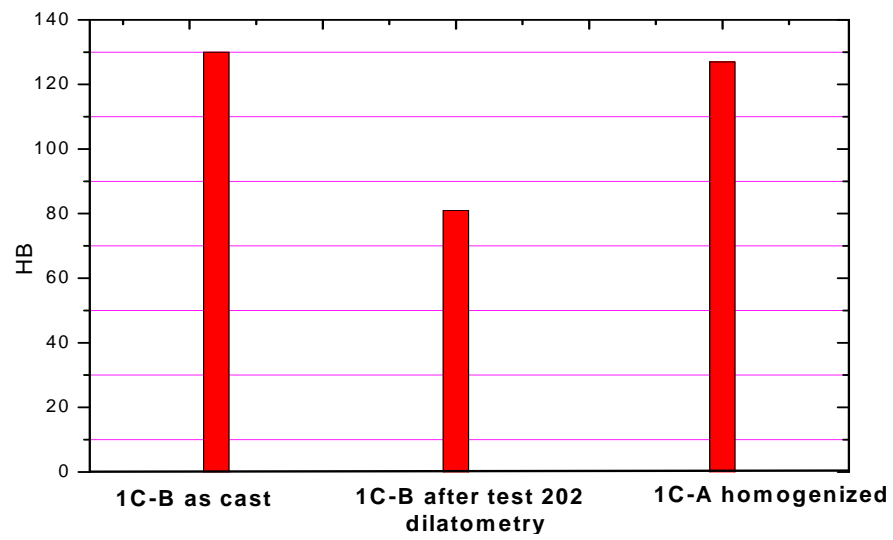


Figure 5.26 Brinell hardness of AW7349 (1A-C,B) in different conditions

5.7 DSC Thermograms

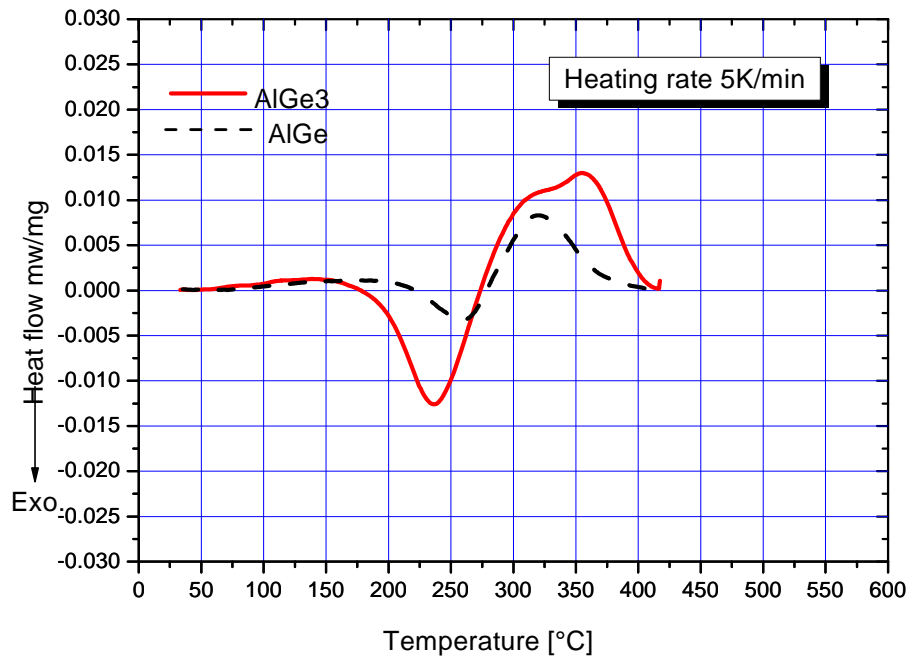


Figure 5.27 Comparing DSC thermograms of AlGe and AlGe3 alloys in the same solution treatment condition (120 min at 410°C + 10 min at 440°C + quenched in water).

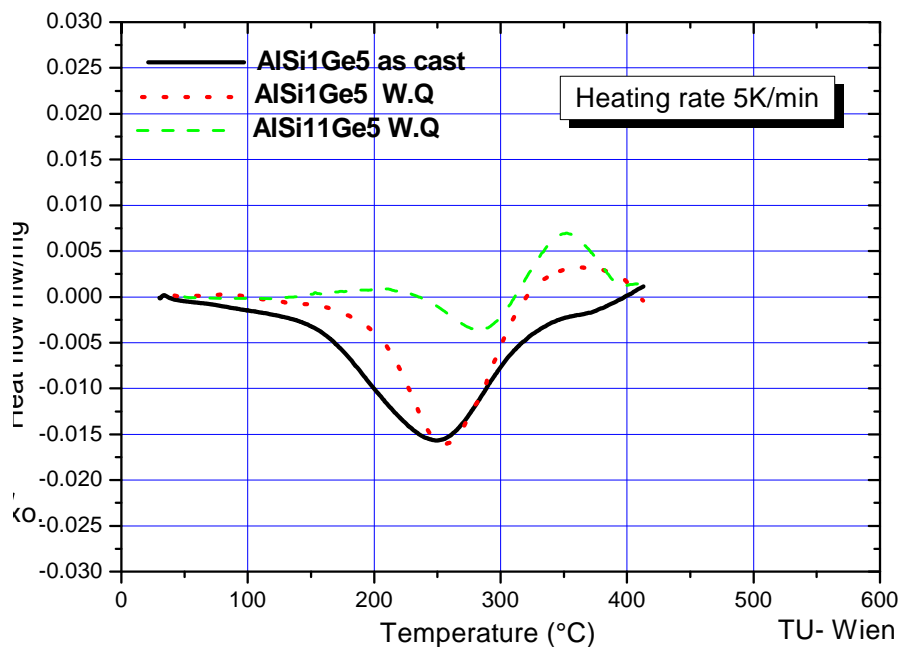


Figure 5.28 DSC thermogram of AlSi1Ge5 alloy with different heat treatments compared with AlSi11Ge5.

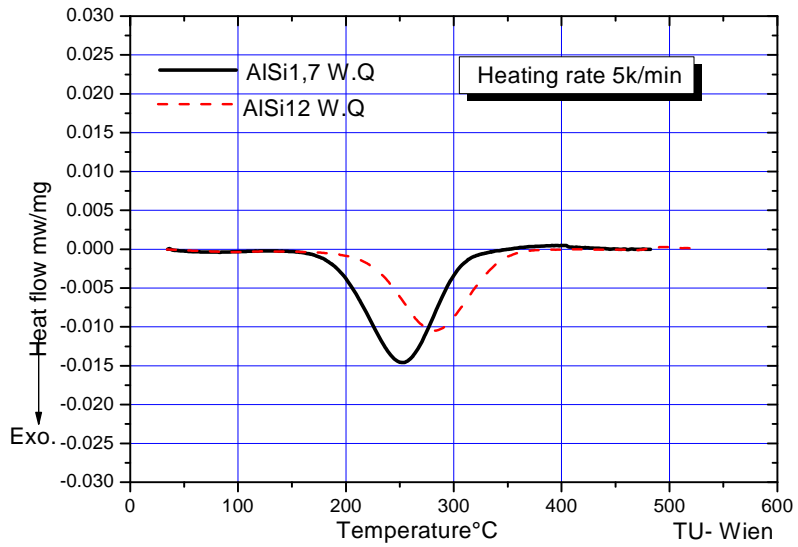


Figure 5.29 Comparing DSC thermogram of AlSi1,7 with AlSi12

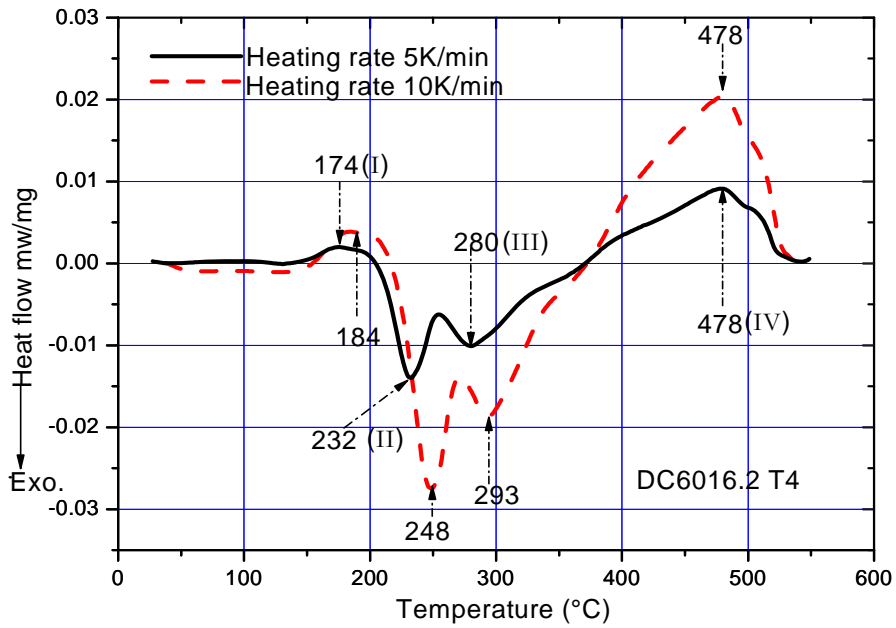


Figure 5.30 DSC thermogram of AW6016DC in W.Q condition comparing heating rates 5K/min and 10K/min

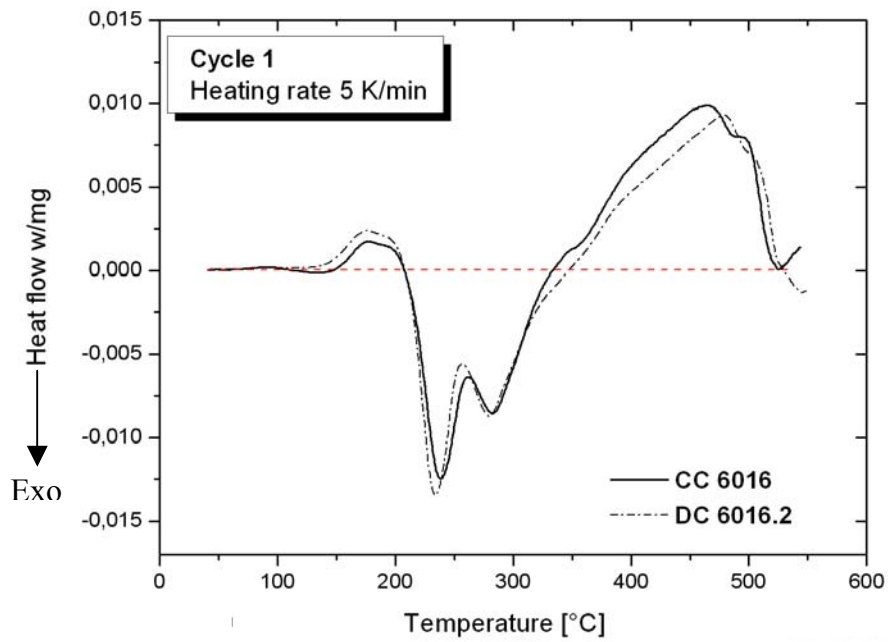


Figure 5.31 Comparing DSC thermograms of first cycles of AW6016.2DC and AW 6016CC in W.Q condition.

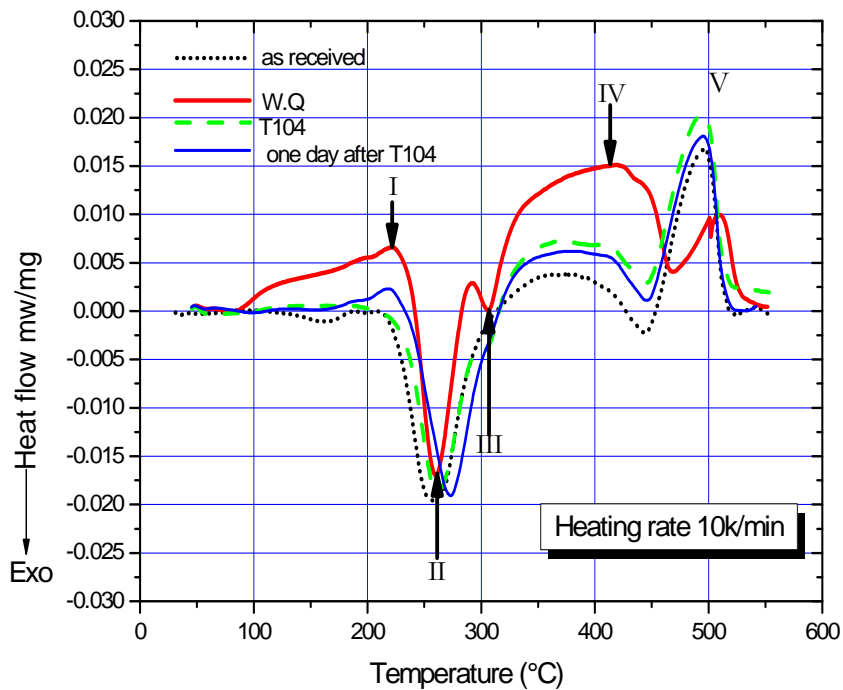


Figure 5.32 Comparing DSC thermograms of AW6008 in different heat treatments. T104 resembles a heat treatment like in an heat affected zone of a weldment (see text).

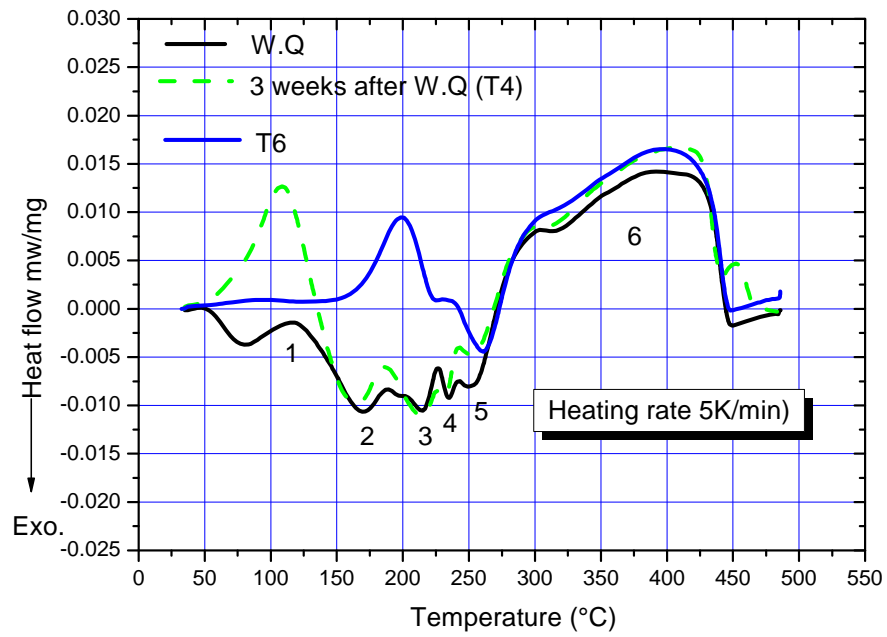


Figure 5.33 Comparing DSC thermograms of homogenized AW7349 in different conditions (distinguished thermal effects are numbered)

5.8 Dilatometry graphs

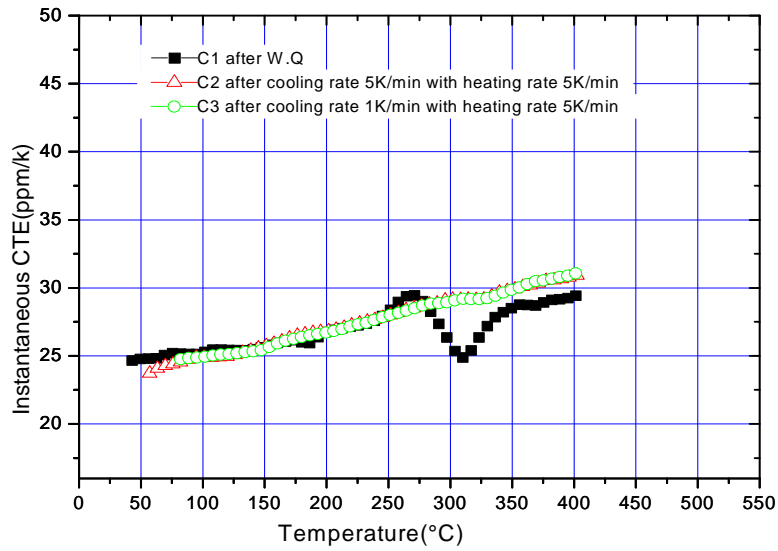


Figure 5.34 CTE(T) of AlGe alloy after different cooling rate from 430°C and same heating rate

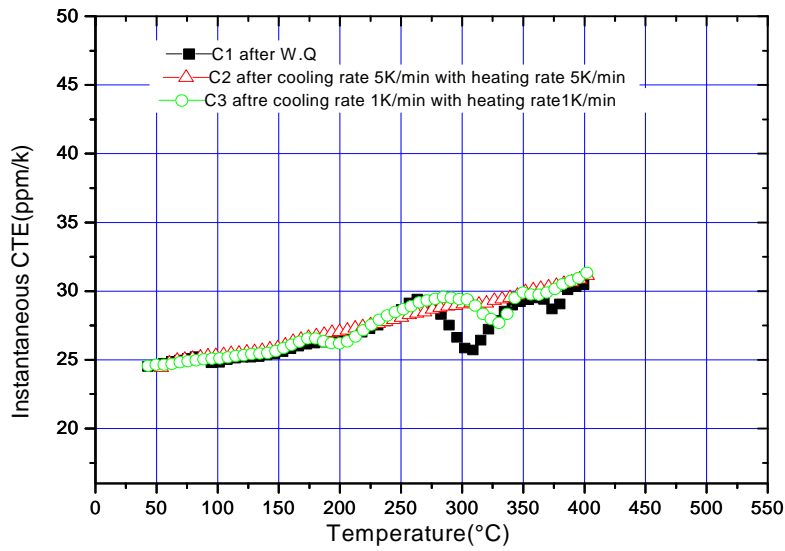


Figure 5.35 CTE(T) of AlGe alloy after different cooling rates from 430°C at different heating rates

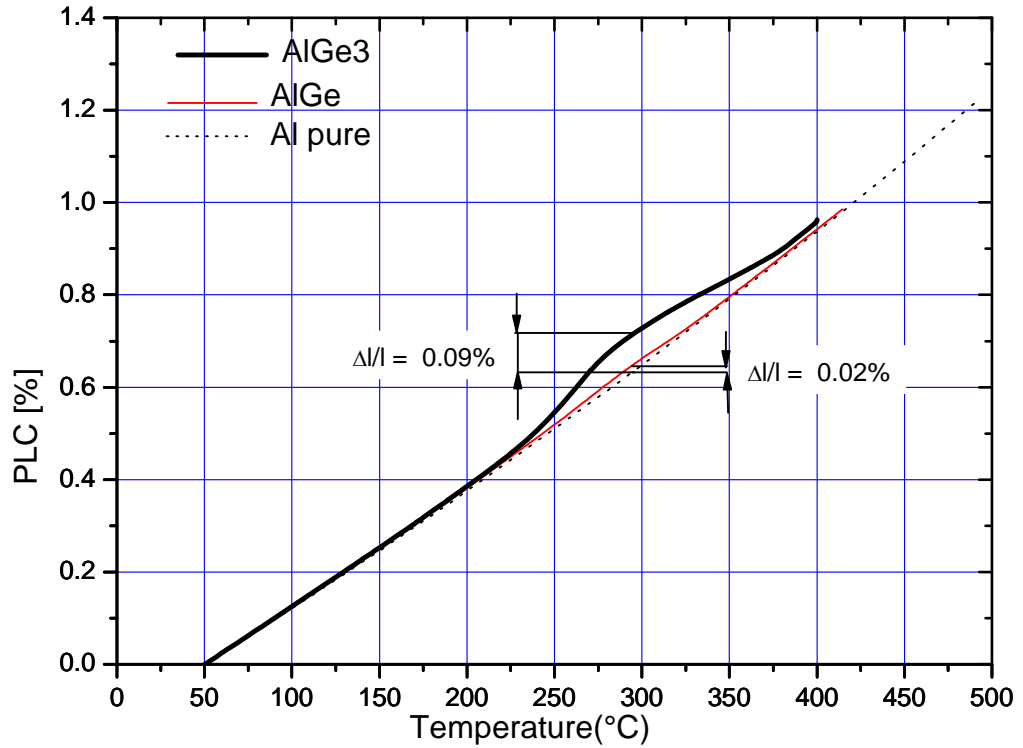


Figure 5.36 Comparing per cent linear change (PLC) AlGe3 and AlGe in W.Q condition with pure Al

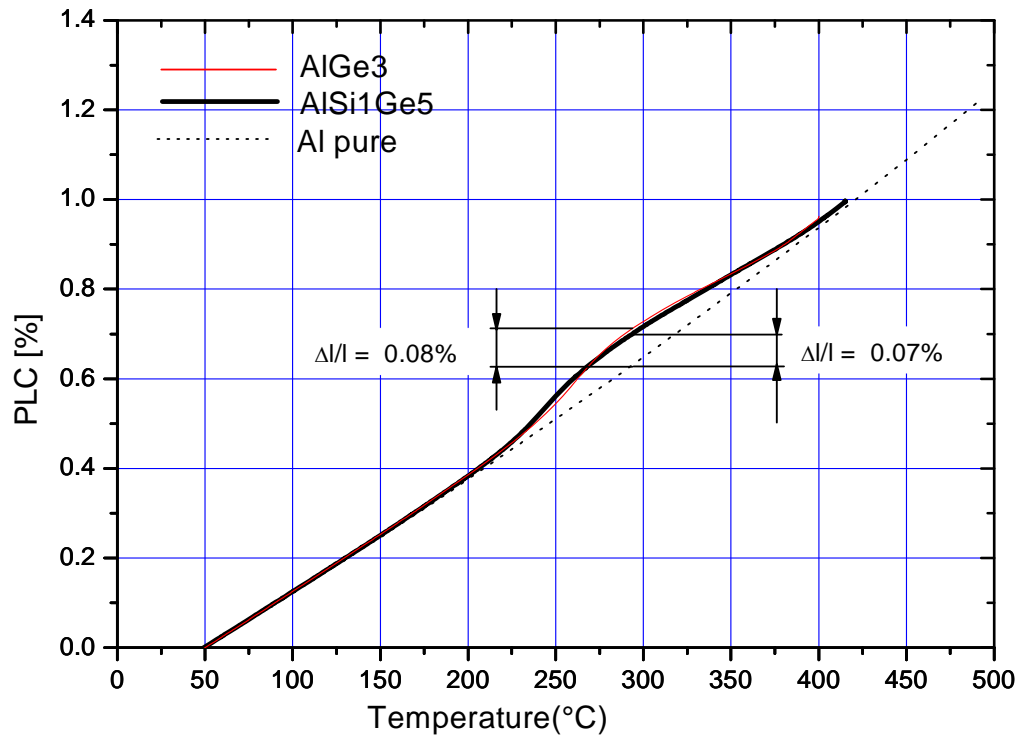


Figure 5.37 Comparing per cent linear change (PLC) AlGe3 and AlSi1Ge5 in W.Q condition with pure Al

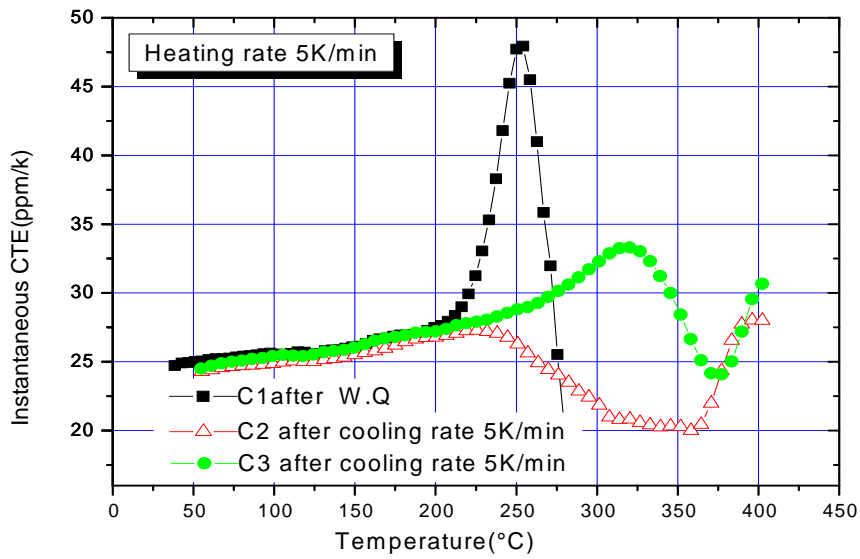


Figure 5.38 CTE(T) of AlGe3 alloy in W.Q (quenched from 430°C) heated at 5K/min to 280°C (C1), then cooled to room temperature at 5K/min and reheated to 430°C (C2). The following cycle is C3.

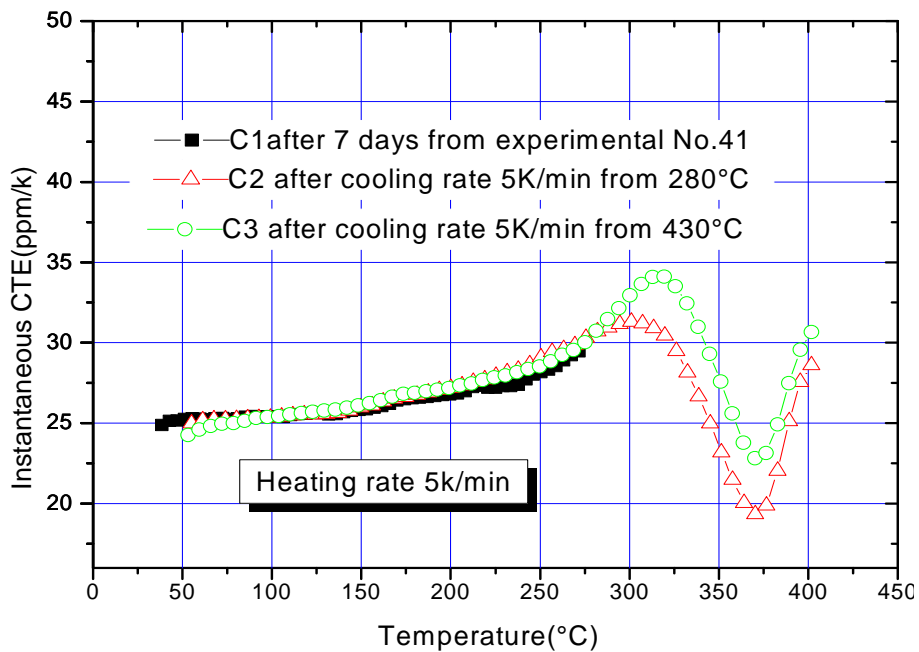


Figure 5.39 CTE of AlGe3 alloy with elapsing time at room temperature after experiment of figure 5.35.

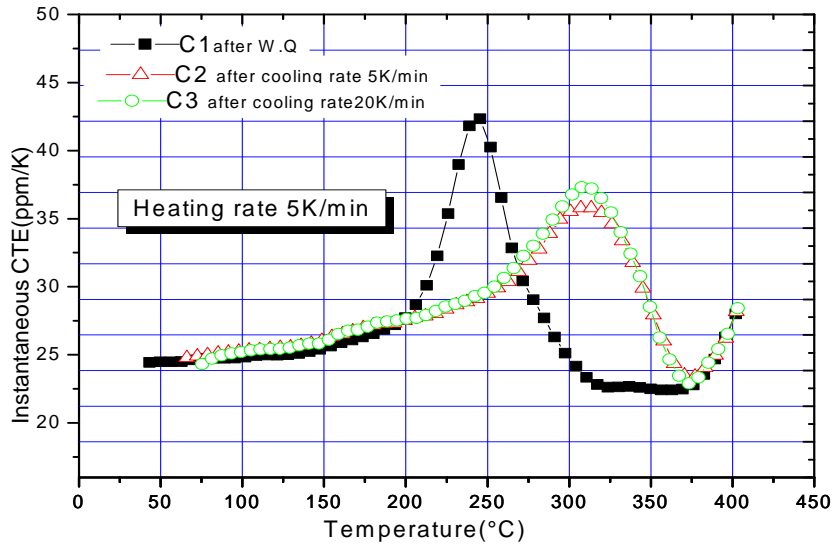


Figure 5.40 CTE(T) showing the effect of the preceding cooling rate for the AISi1Ge5 alloy

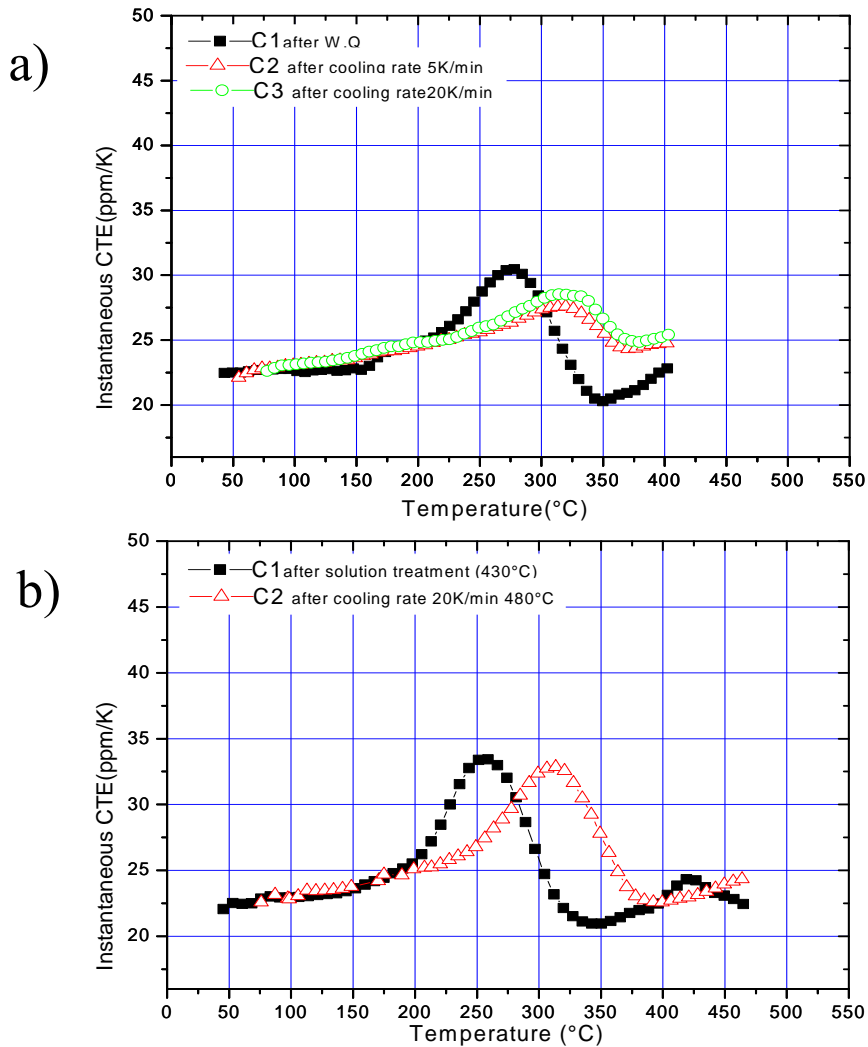


Figure 5.41 CTE(T) of AISi11Ge5 after different solution treatments and cooling rates
 a) 415°C/30min w.q. compared with conditions after cooling rates of 5K/min and 20K/min
 b) 430°C/3h w.q. and after 20K/min cooling from 480°C (second cycle).

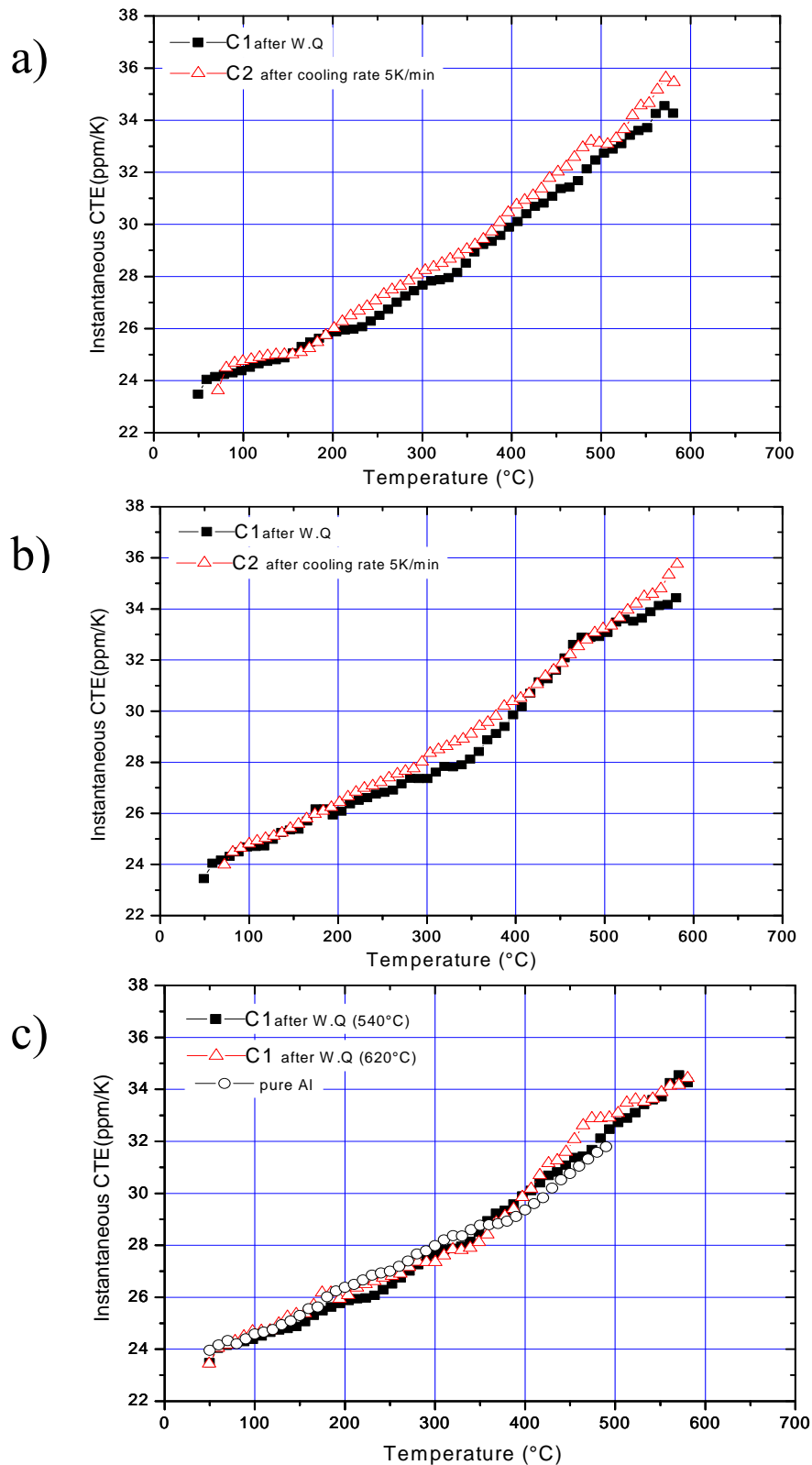


Figure 5.42 CTE(T) of Al-Mn alloy (AW3003) in different conditions of solution treatment.

- a) 540°C/20min w.q. and after cooled at 5K/min from 600°C
- b) 620°C/30min w.q. and after cooled at 5K/min from 600°C
- c) Comparing the Al-Mn alloy after different W.q. with Al pure

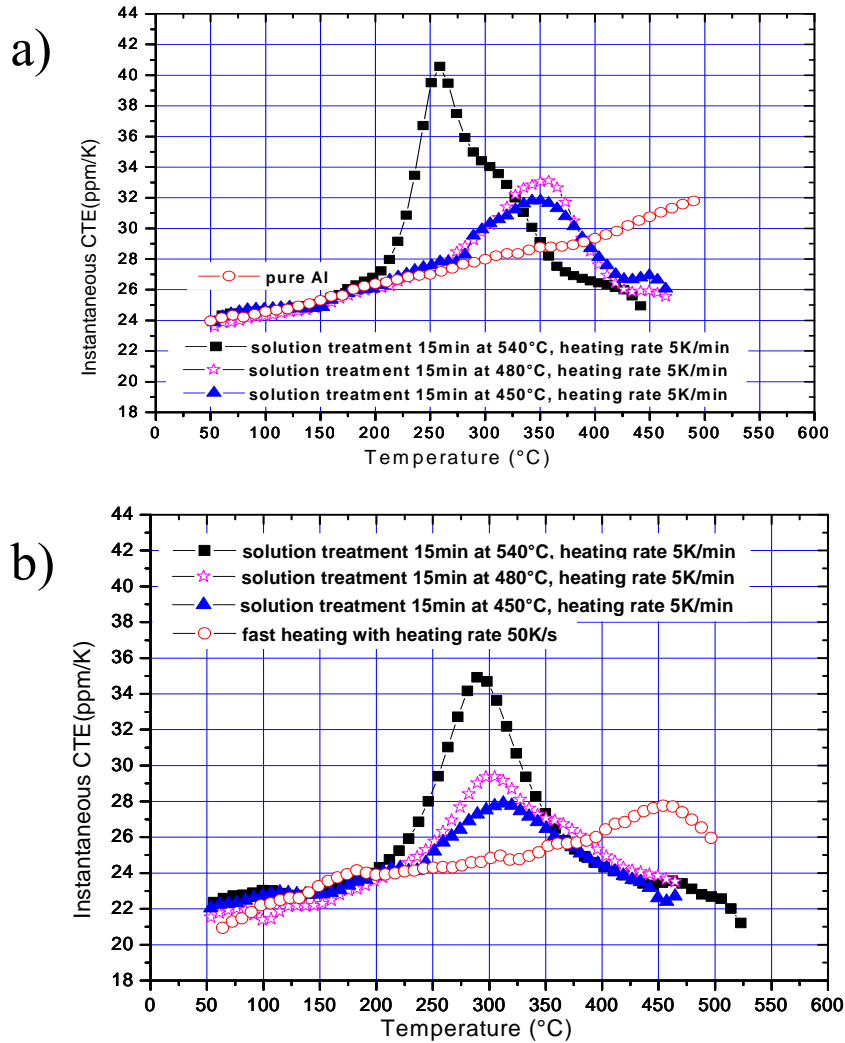


Figure 5.43 CTE(T) of AlSi alloys with different Si content and different solution treatment temperatures, in figure a) for AlSi1.7 with the CTE(T) of pure Al as base line and in b) for AlSi12 with a recording with a fast heating rate used as base line.

Table 5.1. Calculated and experimental change in length due to Si precipitation according above CTE(T) curves in figure 5.43.

Alloy	Solution treated temp. °C	wt% Si in solution	Δl calculation [%]	Δl experimental [%]
AlSi1.7	540	1.18	0.077	0.08
	480	0.66	0.043	0.04
	450	0.48	0.034	0.03
AlSi12	540	1.18	0.077	0.08
	480	0.66	0.043	0.04
	450	0.48	0.032	0.03

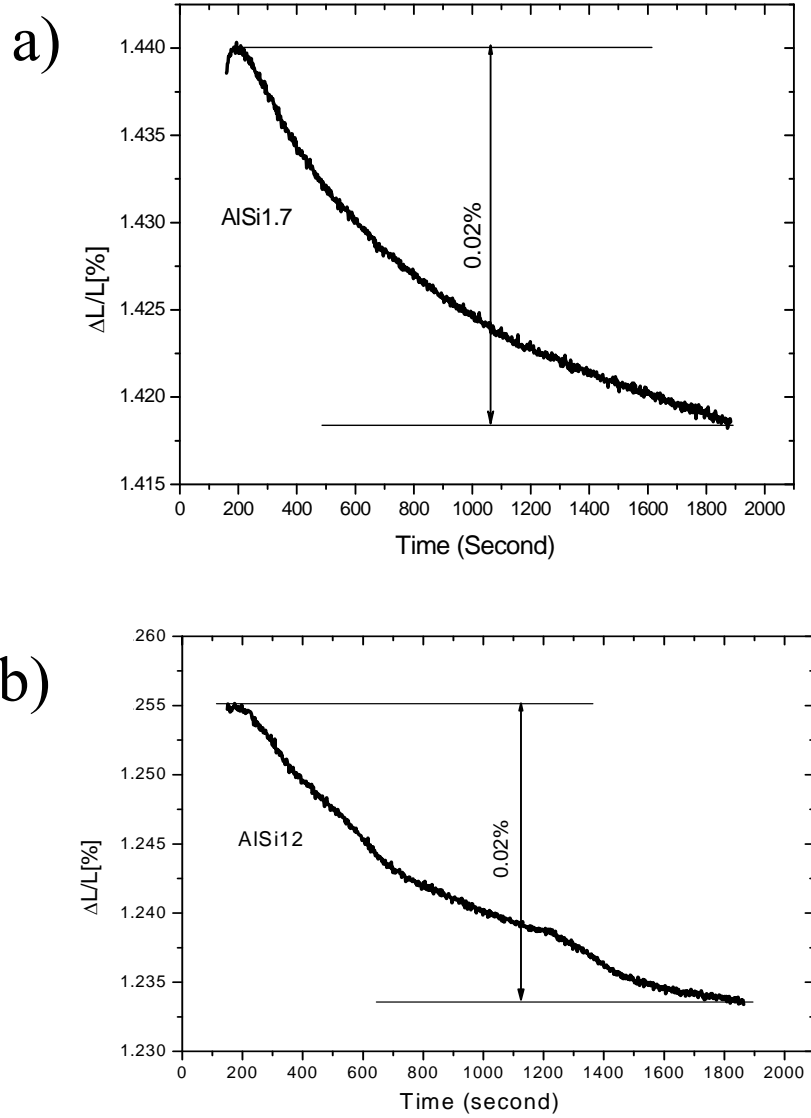


Figure 5.44 Isothermally change in length, after W.Q condition and fast heating 50K/s to 540°C, during holding 30 min at that temperature a) AISi1.7 and b)AISi12

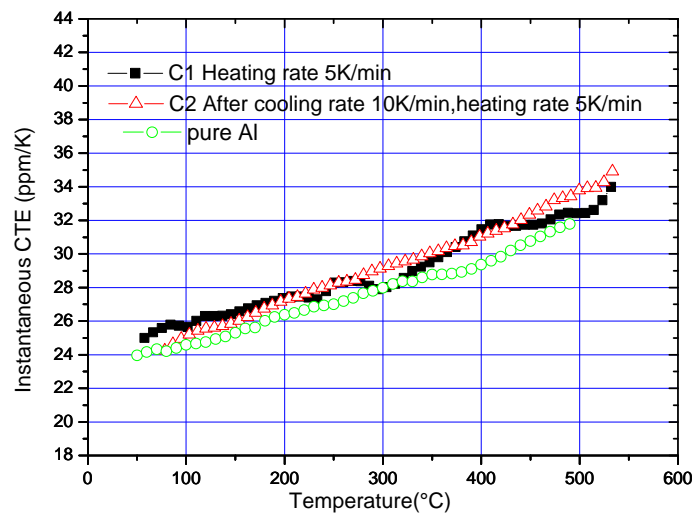


Figure 5.45 CTE(T) curves of Al-Mg alloy (AW5083) for two consecutive cycles after solution quenching from 550°C/1hr.

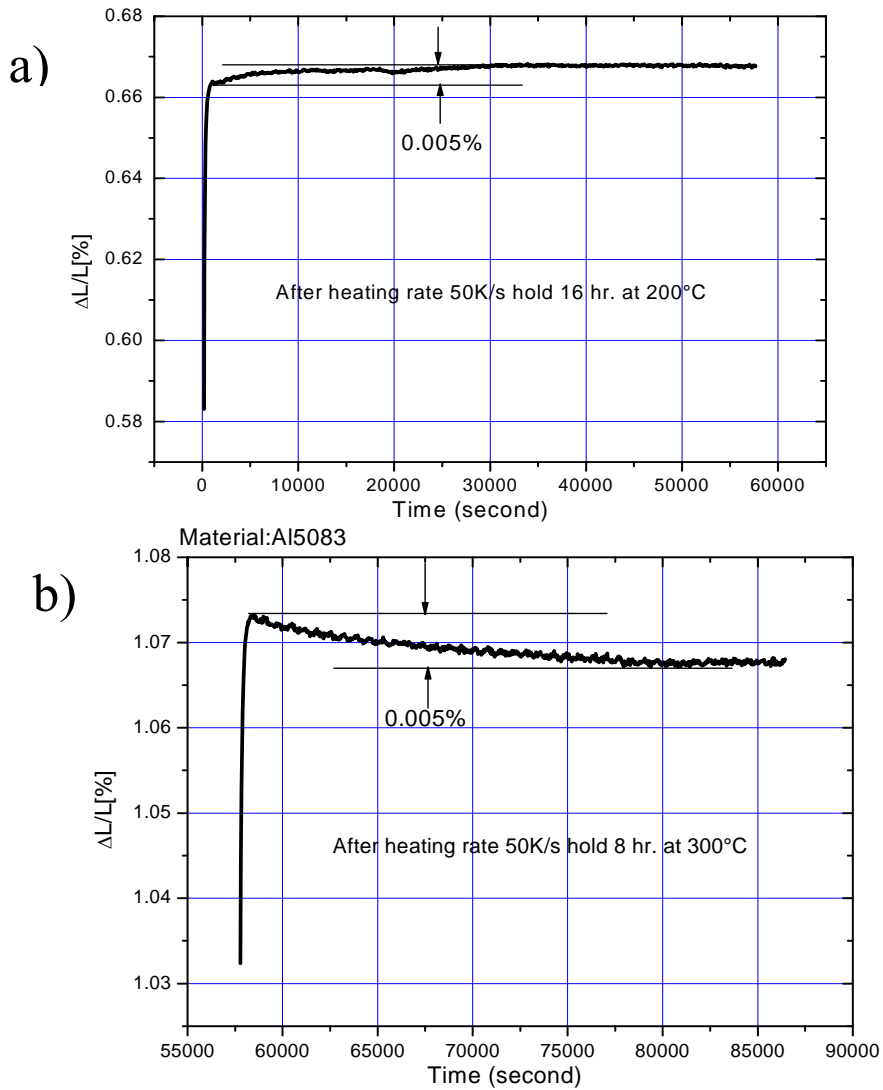


Figure 5.46 Percent linear length change of AW5083 w.q. from 550°C a) during heating and holding isothermally at 200°C/16h. b) further heating and isothermal holding at 300°C/8h.

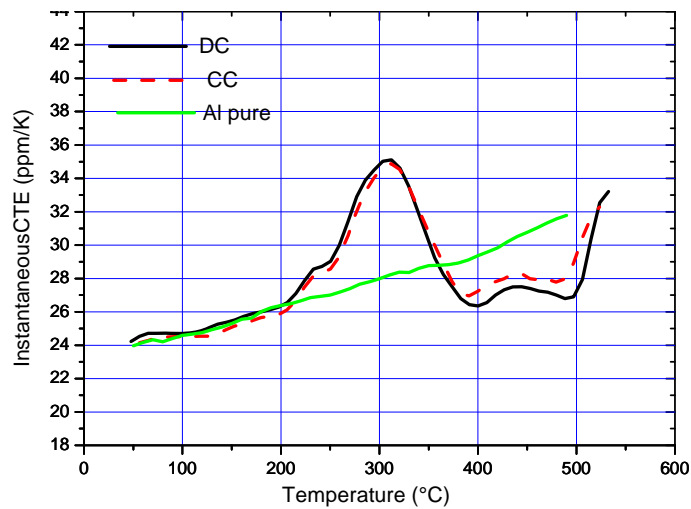


Figure 5.47 Comparing CTE(T) of AW6016CC and DC after solution treatment (550°C/30min + quenching in water)

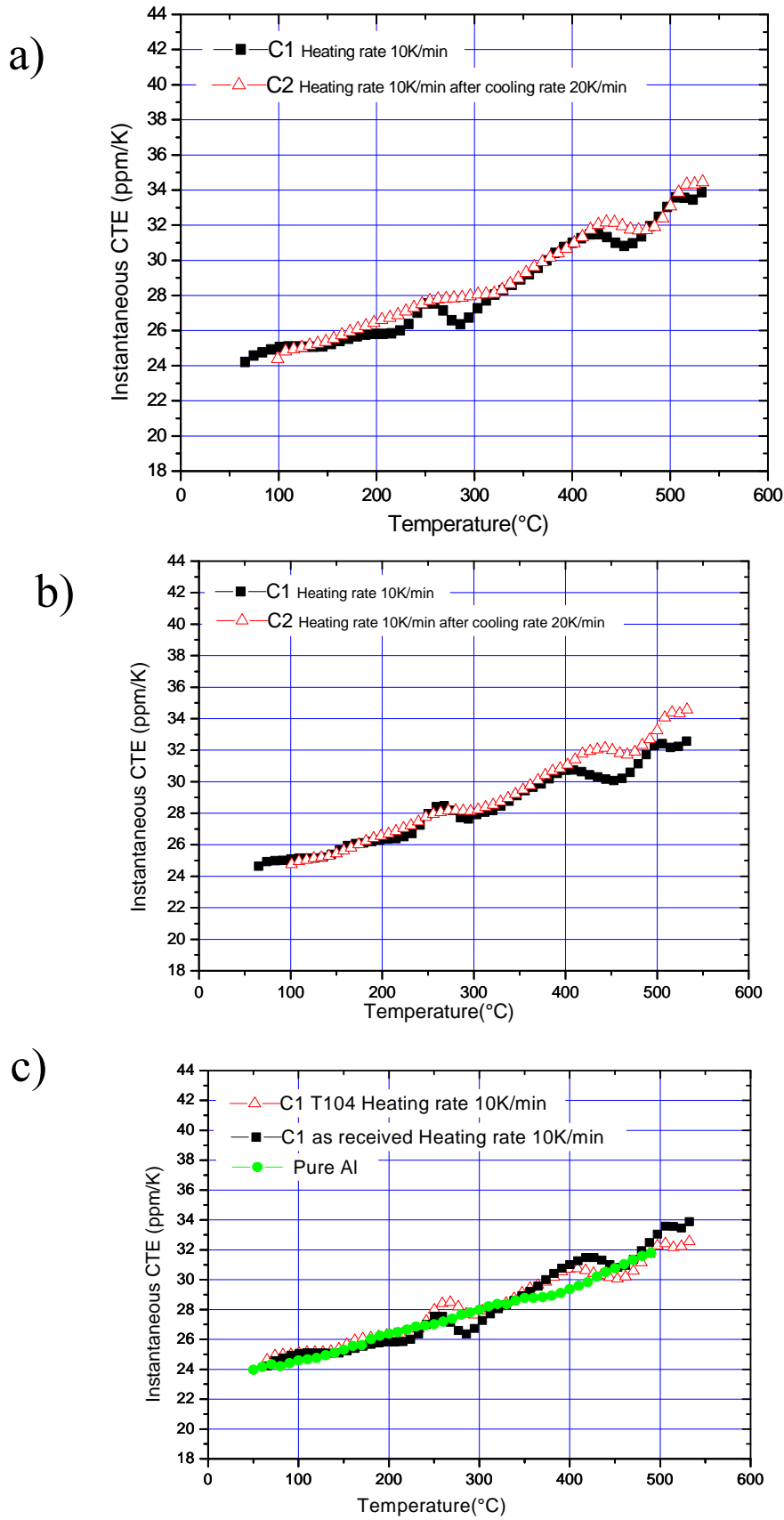


Figure 5.48 CTE(T) of AW6008 alloy a) as received condition b) after heat treated with T104 method simulating a heat affected zone c) comparison of first heating of as received and T104 condition with pure Al.

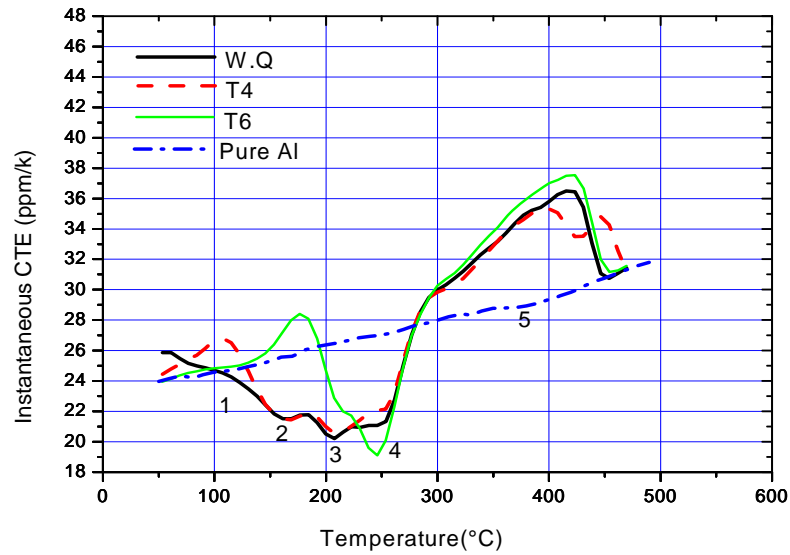


Figure 5.49 Comparing CTE(T) curve of Al-Zn-Mg alloy (7349 1C-A) in different conditions of heat treatment. The numbered expansion effects are referred to in the text.

6. Discussion of results

6.1. Al-Ge and Al-Ge-Si alloys

The mechanical properties of age hardening alloys are governed by the shape, size and distribution of the strengthening particles. The binary Al-Ge and Al-Si and ternary Al-Si-Ge systems are interesting choices for studying precipitation since the precipitates have the diamond cubic structure [76]. Precipitation dispersion in the ternary Al-Si-Ge alloy is almost finer than that in the binary Al-Si and Al-Ge alloys [77]. However the precipitation hardening effect is rather small in these systems (see figure 5.24).

Figure 6.1 shows DSC of Al-Ge and Al-Si-Ge alloys.

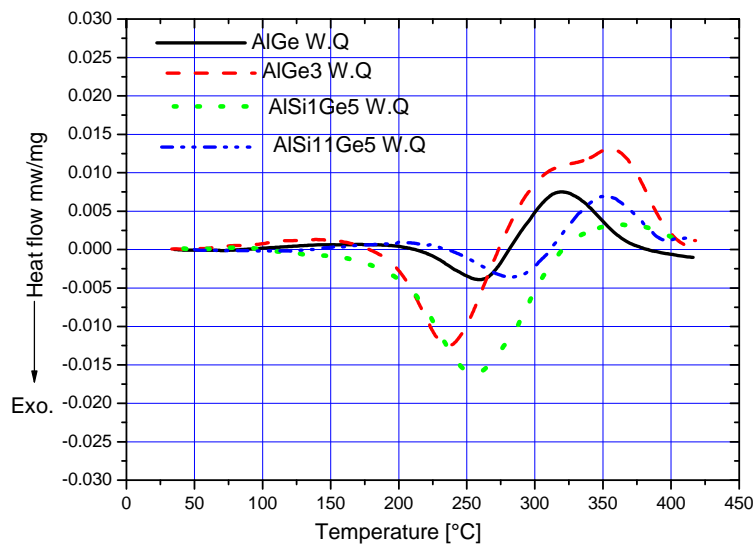


Figure 6.1 Comparing DSC graph of Al-Ge and Al-Ge-Si alloys after solution quenching

In order to simplify the notations, from this point on, we are going to denote f.c.c, aluminum as α -aluminum and diamond-structured germanium as β -germanium. According to Figure 6.1 for the AlGe and AlGe₃ alloys, DSC thermograms show the exothermic peak around 260°C and 235°C, respectively. At this temperature the solid solution decomposes into α -aluminum and β -germanium precipitates. Further on this curve it shows an endothermic peak around 325°C for AlGe and a broad peak for AlGe₃ that show the re-dissolution of germanium in aluminum matrix. The exothermic peak near 260°C and the endothermic peak around 325°C are also confirmed in dilatometry traces of the AlGe alloy as depicted in figure 6.2. Since most of materials have positive coefficients of expansion, a dilatometry curve exhibits an upward tendency like a straight line with increasing temperature, unless some phase changes like

precipitation and dissolution events occur inside the material. As can be seen in this figure there is a positive deviation from pure Al above 200°C which is caused by precipitation and a negative deviation from pure Al above 280°C exhibits dissolution of those precipitates in the material.

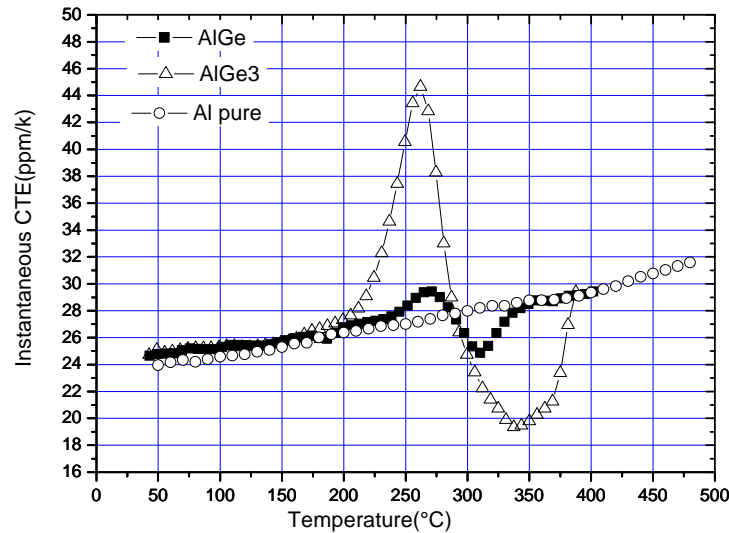


Figure 6.2 comparing CTE (T) graph of Al-Ge alloys

Comparing the DSC thermograms, precipitation in Al Ge₃ starts earlier (160°C) than in AlGe (200°C) and the maxima in precipitation rate are reached at 230°C and 260°C, respectively. The deviation of the linear expansion with respect to pure Al starts at 180°C and 230°C, respectively. The CTE peaks are reached at 260°C for AlGe₃ and 270°C for AlGe. The acceleration of expansion can be attributed to the precipitation, although the effects are measured at somewhat higher temperatures as in the DSC thermograms.

Figure 5.36 ($\Delta l/l$) shows the percent length change (PLC) of AlGe and AlGe₃ alloys in the as-quenched condition (W.Q) and after heating at 5K/min. Figure 5.36 shows the linear expansion of AlGe alloy similar to that of pure Al, but a small deviation from linearity occurs from about 290°C (0.02%), by increasing the amount of Ge this deviation is dramatically increased at 290°C

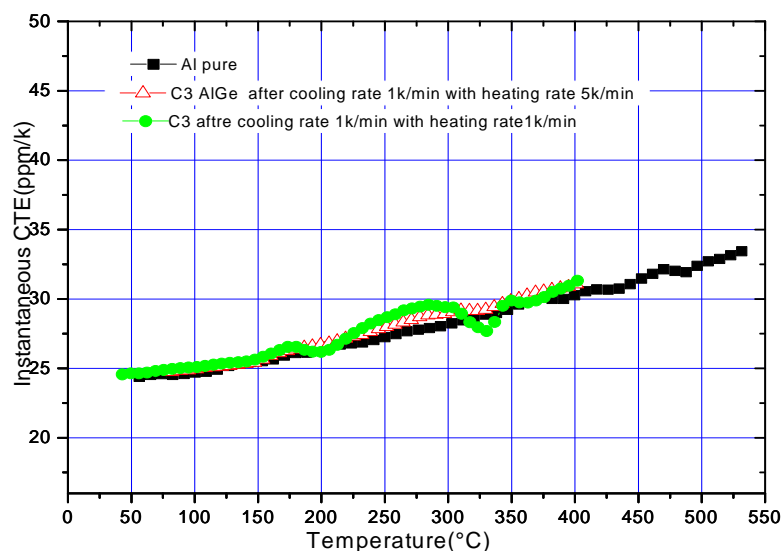
(0.09%). According to equation $\Delta l_{\text{mod}} = \frac{V_{\text{atGe}} - V_{\text{atAl}}}{3V_{\text{atAl}}} f_{\text{Supersaturated}} \cdot 100\%$, we calculated

theoretical values of change in length and the results are given in table 6.1 and compared with experimental results. According to this table there is a difference between theoretical and experimental values for the amount of precipitation. The reason might be, as the temperature increases from W.Q condition during DSC and dilatometry, the amount of precipitation increased while the amount of supersaturation of Ge decreased. In table 6.1, the extreme case is given, where equilibrium would be established during heating up to 250°C.

Table 6.1. Calculated and experimentally change in length due to Ge precipitation

Alloy	Solution treatment	Δl calculation [%]	Δl calculation [%] At 20°C	Δl experimental [%] Due to precipitation	Δl experimental [%] At 250°C
AlGe	430°C	0.08	0.013	0.02	0.01
AlGe ₃	430°C	0.13	0.013	0.09	0.05

Figure 5.38 shows the coefficient thermal expansion CTE (T) of AlGe alloy in three different cycles. As shown in this figure, AlGe alloy from W.Q condition (C1) has a relative maximum at about 270°C this shows the alloy expansion due to precipitation of Ge, and has a relative minimum at about 320°C. It shows that the alloy contracted due to dissolution of Ge. In the third cycle after cooling with 1K/min and heating with 5K/min, we can't see any expansion or contraction in specimen and the thermal expansion of the alloy is close to that pure of Al (see figure 6.3), which indicates the absence of precipitation. Only when heated at 1K/min there are some deviations observed correlated with precipitation. The dilatometry experiments show precipitation effects only at slow heating rate (1K/min) in the third cycle. This indicates that precipitation is very slow in absence of vacancy super saturation due to preceding slow cooling.

**Figure 6.3 comparing CTE(T) of C3 of AlGe in different heating rates with pure Al**

Adding more Ge to aluminium increases precipitation, which is shown in figure 6.2. Comparing figures 5.24a and 5.24b, it is interesting to note that by addition of more Ge into aluminium, increases the hardness of alloy by almost 20% but reaching only around 30HB.

Referring to figure 6.1 the dotted line belongs to the Al-Si-Ge alloy. Many researchers have shown that this type of alloy has very fine and densely distributed precipitates [78, 79]. This may cause a shift of the precipitation peak to lower temperature and there also exist precipitation of Ge at grain boundaries. In the ternary Al-Si-Ge solid solution the vol./atom of Ge is larger and for Si is smaller in size than aluminium (see table 2.8). When pairs of Si and Ge are dissolved in the aluminium matrix, the misfit strain cancellation leads to the reduction of the strain energy barrier for nucleation and decreases the critical nucleation size. Due to this, the precipitation of Si+Ge starts at lower temperature than in the binary Al-Ge alloy. The ternary alloy has much less misfit strain than the binary ones. Vacancies are necessary in the binary alloys to minimize these stresses and to allow the nuclei to grow to the critical size for precipitation.

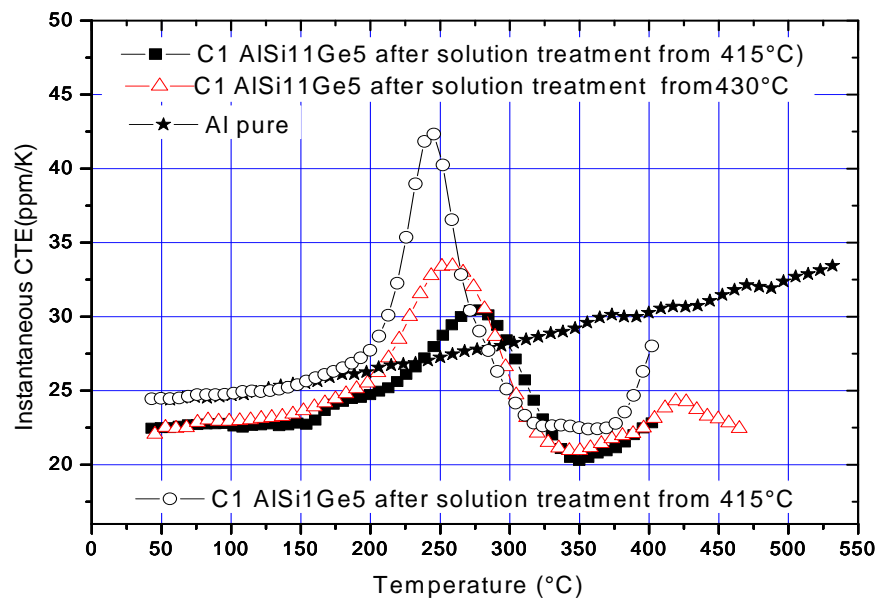


Figure 6.4 Comparing CTE (T) of AlSiGe alloy with different Si content and different solution treatment

Figure 6.4 comprises CTE (T) of AlSi_1Ge_5 with $\text{AlSi}_{11}\text{Ge}_5$ in the same condition of solution treatment and of $\text{AlSi}_{11}\text{Ge}_5$ with different solution treatment. As shown in the figure, precipitation peak for AlSi_1Ge_5 is sharper than that of the $\text{AlSi}_{11}\text{Ge}_5$ and occurs at lower temperature. In $\text{AlSi}_{11}\text{Ge}_5$ the lack of vacancy super saturation due to the vacancy sinks along the interfaces with the eutectic Si may retard the formation of precipitates to higher temperatures.

The Si in AlSi_1Ge_5 increases the precipitation peak in the DSC thermogram with respect to AlGe_3 (quenched from 430°C). Precipitation starts already just above 120°C reaching the peak at 255°C . The associated increase of the expansion starts at about 150°C reaching a peak at 240°C , which is below the CTE peak for AlGe_3 . The higher Ge content together with some Si accelerates precipitation as recorded by DSC and dilatometry although the solution treatment

temperature was 15K lower. In this case the CTE peak is observed at slightly lower temperature than the DSC peak, that is the opposite tendency to the Si free samples

According to metallography 5wt% Ge +1wt%Si are above the solubility limit at 430°C. About 1vol% of grain boundary precipitates of Ge+Si form at this temperature.

The super saturation in Ge and Si of quenched $AlSi_{11}Ge_5$ should be the same as of $AlSi_1Ge_5$ samples both quenched from 415°C. Both the CTE and DSC peaks (275°C) are smaller and at higher temperatures compared with $AlSi_1Ge_5$. This indicates that the existence of eutectic Si-Ge phases reduces the precipitation owing to the loss of vacancies at the eutectic interfaces. Increasing the solution treatment temperature to 430°C increases the precipitation as observed in figure 6.4, but it is still smaller than in $AlSi_1Ge_5$. This effect is more pronounced than in AlSi alloys.

When the temperature is increasing, dissolution of the precipitates will occur as soon as the solubility limits are reached. Table 6.2 shows difference between solubility temperature from phase diagram and experimental observation of the beginning of dissolution.

Table 6.2. Comparison of solubility temperature of Al-Ge and Al-Si-Ge alloys from phase diagram and experimental.

Alloy	T_{sol} (phase digram)	T_{sol}^{start} (DSC)	T_{sol}^{start} (CTE)
AlGe	300°C	280°C	280°C
AlGe ₃	370°C	260°C	280°C
AlSi ₁ Ge ₅	420°C	320°C	280°C

The overlapping of formation and dissolution in DSC thermograms yields different T_{sol}^{start} , where the heat flow becomes bigger than the base line. The CTE curves give the same temperature, where expansion drops below that of pure Al, which indicates dissolution of Ge precipitates. This temperature of 280°C corresponds to the solubility surpassing 0.9at%Ge.

6.2. Al-Mn alloy (AW3003)

As depicted in table 4.5 in this alloy, Mn and Si are alloying elements and Fe impurities. The addition of alloying elements in Al–Mn alloys has strong influence on the precipitation behavior. Fe and Si greatly decrease the solubility of Mn in solid solution and accelerate the precipitation rate [88].

During solidification, constituent particles $Al_6(Mn,Fe)$ and $\alpha-Al(Mn,Fe)Si$ form in the alloy mainly as inter-dendritic eutectic networks [87]. Some $Al_6(Mn,Fe)$ particles transform into α -

Al(MnFe)Si particles during homogenization heat treatment. These α -Al(MnFe)Si particles, are harder than $Al_6(Mn,Fe)$ particles. It has been found that Mn and Fe are substitutional in primary $Al_6(Mn,Fe)$ and α -Al(Mn,Fe)Si within a wide limit [87]. The deposition of supersaturated Mn onto primary particles and dissolution of Mn-rich dispersoids cause the increase of Mn content in primary particles and the decrease of the solut content of Mn in the matrix.

The 5K/min CTE (T) thermograms of AW 3003 in different conditions of solution treatment are shown in figures 5.42a,b. As can be seen in figure 5.42b, there is a deviation from second cycle, which starts at around 310°C. This deviation is associated with some precipitation of Mn. Due to the low diffusion rate of Mn in aluminium at low temperatures, the decrease of Mn in solid solution mainly causes the precipitation of dispersoids, and further precipitation of Mn onto primary particles can be neglected. In figure 542c Al-Mn alloy after different W.Q condition compared with Al pure this figure shows a small deviation from pure Al. There is no expansion effect corresponding to excess Si.

6.3.Al-Si alloys (4XX.X)

The Al-Si system is a simple eutectic system containing two phases, fcc Al and diamond cubic Si. The solubility of silicon in aluminium reaches a maximum 1.65 at. % at the eutectic temperature of 577°C [80] see figure 4.4. Aluminium is fcc with a coordination number of 12 and Silicon is diamond cubic with a coordination number of 4, referred to the Hume-Rothery rules for substitutional solid solution the solubility of Al in Si is extremely limited.

Differential scanning calorimetry of different AlSi alloys are depicted in figure 6.5. As shown in this figure, the two kinds of alloys have different peak temperatures 250°C and 290 °C for AlSi1.7 and AlSi12, respectively. The amount of precipitation is also different, because they have different peak areas. The molar heat of reaction (here precipitation) for AlSi1.7 is more negative than the other one. In AlSi1.7 alloy in W.Q condition, the exothermic peak observed in DSC run between 170 and 325°C clearly correlates with the noticeably expansion of the alloy at the same temperature interval during dilatometric measurements (both dilatometry and DSC tests at 5K/min). For this alloy, the expansion of pure-Al can be taken as base line for comparison with the CTE curves. Exothermic precipitation of incoherent globular Si and Si platelets, having higher atomic volume (diamond-Si) compared to that of the substitutional Al-Si fcc structure [82] and thus produce an expansion above that of pure Al.

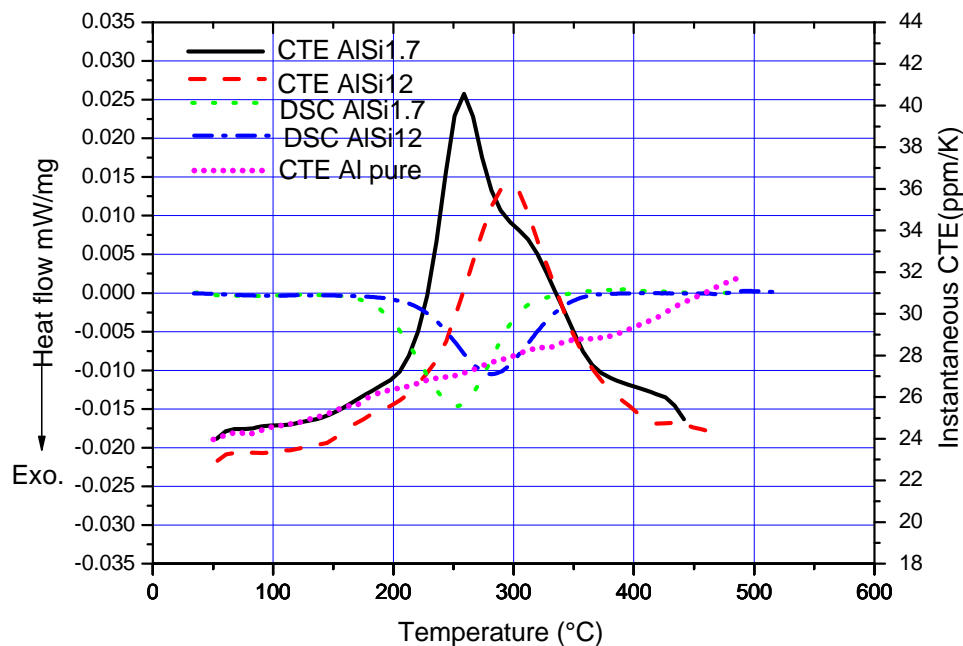


Figure 6.5 Instantaneous CTE and heat flow of AlSi1.7 and AlSi12 alloy in W.Q condition.

The AlSi12 material consists of the α -dendrites with interdendritic eutectic microstructure. DSC thermograms and dilatometry curves of the material AlSi12 are also shown in figure 6.5 by using a common temperature axis and two different y-axes. The material was in W.Q (540°C/15min + water quenched) condition before the tests. The exothermic peak of the DSC curve presents the precipitation of Si at about 280°C and coincides well with the peak of the CTE(T), which extends over a wider temperature range. Dissolution of Si is only observed in dilatometers.

The exothermic effect is shifted to a higher temperature for AlSi12. The exothermic energies for DSC runs in AlSi1.7 and AlSi12 samples result for AlSi1.7 to be 1.1 W/g.K and for AlSi12 around 0.8 W/g.K. This decrease in exothermic precipitation energy is related to the presence of eutectic Si, where Si and vacancies can precipitate easily.

The samples AlSi1.7 and AlSi12 were solution treated at 540°C, 480°C and 450°C for 15 min and water quenched. The CTE of the samples at heating rate of 5 K/min are depicted in figure 5.43a and b. Although the Si contents of the both alloys are different, the solubility limit of Si in both alloys at different solution temperatures should be thermodynamically the same. The excess amount of Si is segregated in the AlSi eutectic.

The CTE of the AlSi12 alloy in W.Q condition was measured at a fast heating rate of 50 K/s (by Bähr dilatometer) to exclude a Si precipitation effect. Because precipitation is diffusion

dependent, 50 K/s heating rate is considered to be high enough to prevent significant precipitation during heating, and just thermal expansion excluding precipitation is measured.

The area between the base line and each dilatometer cycle was calculated numerically and was equal to the increase in length due to only Si precipitation. This can be compared with calculated theoretical values of length changes due to precipitation, given by [82].

$$\Delta l_{\text{mod}} = \frac{(V_{\text{at}_{\text{Si}}} - V_{\text{at}_{\text{Al}}})}{3 \cdot V_{\text{at}_{\text{Al}}}} \cdot f_{\text{supersaturated}} \cdot 100\%$$

Where $V_{\text{at}_{\text{Si}}}$ and $V_{\text{at}_{\text{Al}}}$ are the atomic volumes of Al and Si, respectively, and $f_{\text{supersaturated}}$ is the concentration of Si in supersaturation (max. solubility at temperature) [89].

Comparing figure 5.43a and b reveals, that although the amount of Si precipitation for the same solution treatment is the same, the precipitation kinetics (position and height of the peaks) of both materials are different (250 and 300°C, respectively). Depletion of vacancies near the interface area of the eutectic structure in AlSi12 is one factor to interpret this observation, which may increase the critical radius of nuclei as well. Figure 5.44a and b shows isothermally change in length after W.Q condition and fast heating 50K/s to 540°C during holding 30 min at that temperature percent change in length for both alloy are the same.

6.4Al-Mg alloy (5xxx)

Precipitation behavior and changes in mechanical properties of Al-Mg alloys have been extensively studied by researchers and they have been confirmed that the changes were caused mainly by the formation of Guinier-Preston (GP) zones and that with a reversion treatment following a period of natural ageing, all these properties returned to the as-quenched values [90].

As mentioned in chapter 2 the Al-Mg supersaturated solid-solution decomposition has four-stages solid solution → GP zone → β'' → β' → β . The GP zones are thin plates and consist of solute-rich clusters which may be only one or two atom planes in thickness they could be observed at the beginning of ageing at relatively low temperature, e.g. room temperature [90].

Instantaneous coefficient of thermal expansion of AW5083 is shown in figure 5.45. The material was in W.Q (550°C/1h + quenched in water) condition before the test. As depicted in this figure, there is a positive deviation from C2 between 50 to 100°C, this refers to formation of GP zones. We can also see a small deviation between 100 to 200°C caused by the formation of β'' . There is a small negative deviation from C2 around 230°C which refers to dissolution of β'' . Between

250 to 280°C we can see relative positive deviation which may refer to formation of β' . The negative deviation between 280 to 360°C is attributed to dissolution of β' . Between 370 to 430°C, β forms and after that dissolution of all phases occurs.

Isothermal dilatometry was carried out on AW5083 and results are shown in figures 5.46a,b. Figure 5.46a shows about 0.005% increase in the length which refers to precipitation at 200°C which should refer to 2 at% of Mg in supersaturation and. Figure 5.46b shows 0.005% decrease in the length which refers to dissolution at 300°C, where the solubility of Mg is higher than its content in the alloy. This phenomenon is confirmed in figure 5.45.

6.5 Al-Mg-Si alloys

Differential scanning calorimetry of Al 6016.2 DC is shown in figure 6.6 for a heating rate 5K/min. Four peaks are visible in the thermogram, indicated by (I) to (IV). The endothermic peak (I) with a maximum at approximately 174°C is due to dissolution of GP zone. GP zones formed at room temperature are completely coherent with the aluminum matrix. The exothermic peak (II), with a minimum at approximately 232°C, represents the precipitation of β'' intermediate phase due to Mg-Si clusters (Mg_5Si_6) and is fully coherent with the matrix [83].

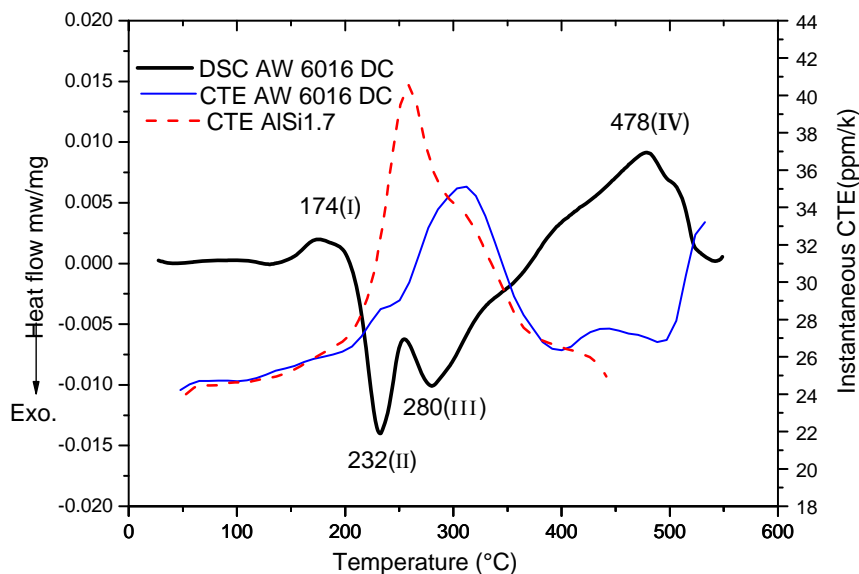


Figure 6.6. DSC thermogram of AW 6016DC in W.Q condition with indicated peak position (I-IV) and show comparison with CTE(T) of AW6016DC and AISi1.7 alloy.

The exothermic peak (III), attributed to the transformation of β'' into β' phase with a minimum at approximately 280°C, is caused by the formation of Mg_2Si particles [84].

The endothermic peak (IV) with a maximum at approximately 478°C is due to the dissolution of the Mg_2Si particles. The effects of heating rate on solid-state reactions is illustrated in figure

5.30, which shows DSC curves for alloy AW6016.2DC in W.Q condition, taken at two heating rates. It is noted that the first endothermic peak and two exothermic peaks are strongly affected by the heating rate whereas the last endothermic peak is not. This is typical of two types of processes, namely, those affected by reaction kinetics (the first three peaks) and those dominated by the thermodynamics of the reaction (the last peak). Dilatometry tests of AW6016CC, DC as shown in figure 5.47 produce effect in the same region but there excess Si is precipitating as well. The position of the double peak in the CTE(T) curve of W.Q of AlSi1.7 resembles that of the W.Q of the AW6016DC, where the overlapping peaks are weighted differently.

Concerning AW6008, four different kinds of experiments have been performed on this alloy (as received, W.Q, T104, one day after T104) to monitor the behavior of precipitates and dissolutions, as depicted in figure 5.32 DSC scans are characterized in W.Q condition by two sharp endothermic (dissolution) peaks called I, IV and two exothermic (precipitation) peaks designed as II, III. The first peak is directly related to the dissolution of pre-existing particles, i.e. GP zones. Peak (II) is due to the formation of more stable phases, related to precipitation of β''/β' and peak III is due to formation of β' phase. While peak IV is related to dissolution of β' particles [85], there is another endothermic peak (V) which is related to dissolution of the $Al_{10}V$ phase. Figure 6.7 shows comparison of the DSC curves in different solution heat treatments. In W.Q condition before the β''/β' precipitation peak, a dissolution peak is observed around 220°C. This peak results from the dissolution of GP zones. The area of the GP dissolution peak after W.Q condition is larger than for the other conditions. β' precipitates in W.Q condition after dissolution of β'' . In T104 condition, it has a shoulder at about 310°C, which can be attributed to the precipitation of β' during dissolution of β'' and no GP zones have precipitated in T104 condition.

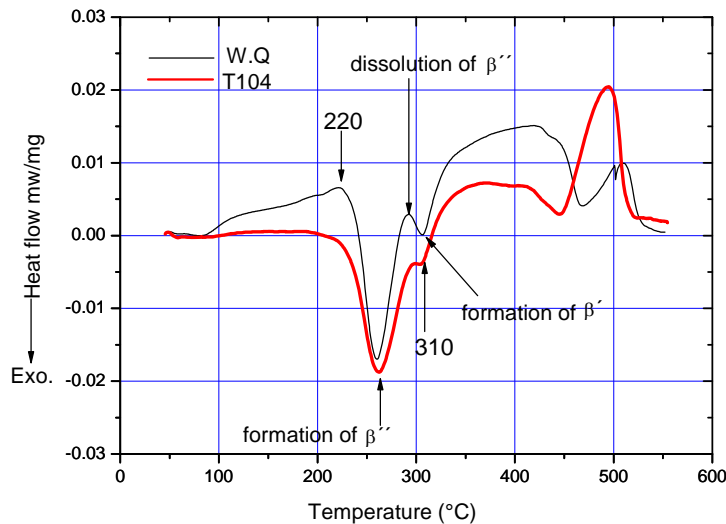


Figure 6.7 DSC thermo gram of AW6008 in different conditions of heat treatment

DSC and CTE tests in T104 condition carried out on 6008 alloy and depicted in figure 6.8 (dilatometry and DSC tests at 10K/min). The expansion of pure-Al can be taken as base line for comparison with the CTE run. The first exothermic peak of the DSC curve represents the precipitation of β'' between 200-300°C and coincides well with the small peak of the CTE(T). The CTE goes back to the Al base line at 270°C, where dissolution of β'' is expected (see figure 6.7 dissolution of β''). This would mean that the CTE curve reflects rather the formation of Si precipitation due to the surplus of 0.2 wt% Si superimposed in the DSC thermogram.

The crystal structure of Si in Al solid solution is FCC with $V_{\text{at si}}=0.0152 \text{ nm}^3/\text{atom}$ and of Mg $V_{\text{at Mg}} = 0.023\text{nm}^3/\text{atom}$ yielding a volume of 0.0612nm^3 for 2 Mg plus 1 Si atom. The difference with respect to 3 Al atoms amounts to +23%. This means that particularly the Mg atom expand the Al lattice in solid solution, which yields a high probability of Mg vacancy pairs. The volume per molecule of crystalline Mg_2Si according to table 2.4 with low different lattice parameter (0.635-0.640 nm) is $0.063\text{-}0.066\text{nm}^3/\text{atom}$. If Mg_2Si precipitates with $0.063\text{nm}^3/\text{atom}$, it creates a change in volume +3% and with $0.066\text{nm}^3/\text{atom}$ +8% with respect to solid solution of Mg and Si. We couldn't see this amount of volume change in our experiment because we assume that vacancy loss occurs during precipitation.

Comparing the results of 6008 with higher Mg_2Si content but less excess Si than 6016DC suggest that the Si precipitation is dominating the thermal expansion whereas the DSC curves reflect the Mg_2Si precipitation.

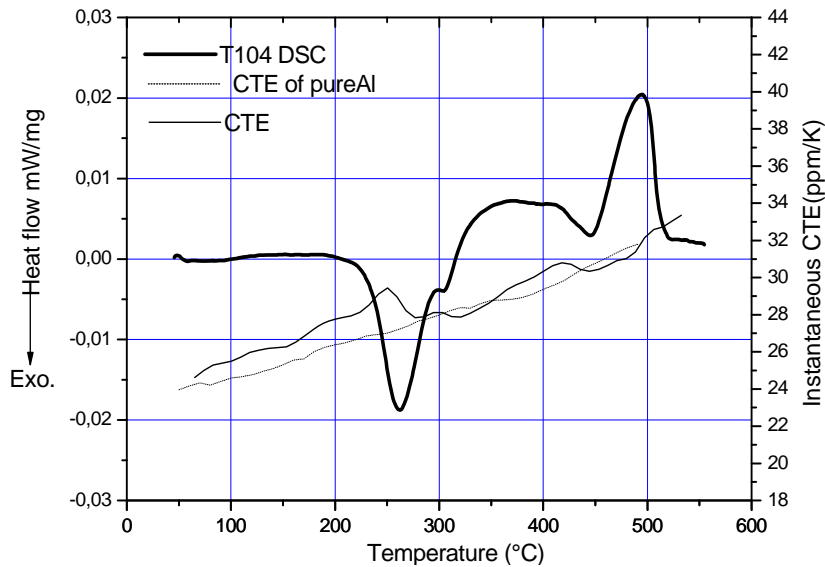


Figure 6.8 DSC and CTE(T) of Al6008 in T104 condition.

6.6 Al-Zn-Mg alloy

The phenomena of phase transformations are very complex particularly in the case of the Al-Zn-Mg alloys because of the various parameters which influence them (heat treatments, chemical composition, relationship between different chemical constituents. . .) [91].

Differential scanning calorimetries of Al-Zn-Mg-Cu (AW7349 1C-A) alloy in different conditions are depicted in figure 5.33. The scan from the W.Q specimen shows five distinct precipitation reactions in the temperature range 50-275°C. Peak 1 (heated to 75°C) is most likely associated with the clustering of the solute leading up to the formation of GPI zones. Peak 2 (heated to ~165°C) indicates that this exothermic reaction corresponds to the formation of the η' phase. Peak 3 (~220°C) is associated with the formation of the η phase. Peak 4 (~237°C) is most likely associated with the formation of the T ($Mg_3Zn_3Al_2$ or $Mg_{32}(Zn,Al)_{49}$) Phase. The final exothermic reaction under peak 5 (~250°C) may correspond to the formation of the S ($CuMgAl_2$) phase [86]. The endothermic peak 6 (~400°C) shows dissolution of all phases.

DSC scan in W.Q plus three weeks (room temperature ageing) (T4) condition exhibited an endothermic peak at about 110°C. The position of the endothermic reaction indicates that the GPZ formed during room temperature ageing increased in number density of precipitates compared to the W.Q condition.

As shown in this figure the dissolution peak in T6 condition, shifted to higher temperature (200°C), which indicates an increase in the thermal stability (size) of η' zones formed in T6 condition. As depicted in Figure 5.33 in T6 condition, complete dissolution of GP zones is observed before any other precipitation event (because there is a straight-line between

endothermic and exothermic effect). However, in W.Q condition the direct transition from the endothermic to the exothermic reaction at $\sim 135^\circ\text{C}$ is observed.

Dilatometric curve, CTE(T) of Al-Zn-Mg alloy (7349 1C-A) is given in figure 5.49. According to that curve the first expansion is in the interval of temperature ($75\text{--}100^\circ\text{C}$) this expansion is allotted to the dissolution of GP zones or VRC (Vacancy Rich Cluster) formed after cooling. Two successive contractions are obtained in the interval of temperature ($143\text{--}280^\circ\text{C}$) with three minima located at 160°C , 210°C and 255°C , respectively. The first contraction with a minimum located at 160°C , it is probably due to the formation of GPII zones or the VRC or/and the η' . The second contraction with two minima is located at 210°C and 255°C , this contraction would be due to the precipitation of the η . The second expansion interval ($280\text{--}420^\circ\text{C}$), is due to the dissolution of the precipitates of the various types (η_1 , η_2 , η_3) of equilibrium η phase [91].

For ageing at room temperature (W.Q +3 weeks at room temperature), the first expansion is slightly shifted towards the high temperature (105°C). This expansion is due to the dissolution of the precipitates formed during room temperature aging. The sequence of contraction and expansion after the first expansion are quite the same as of W.Q condition.

For T6 condition (W.Q + $120^\circ\text{C}/24\text{h}$) the maximum and minimum are shifted towards higher temperatures. The first expansion is due to the dissolution of η' , the contraction is due to the precipitation of η and two minima ($220\text{--}245^\circ\text{C}$) may be due to precipitation of the various types of η phase. There is a clear correlation between DSC and CTE(T) results as shown in Figure 6.9 for both conditions.

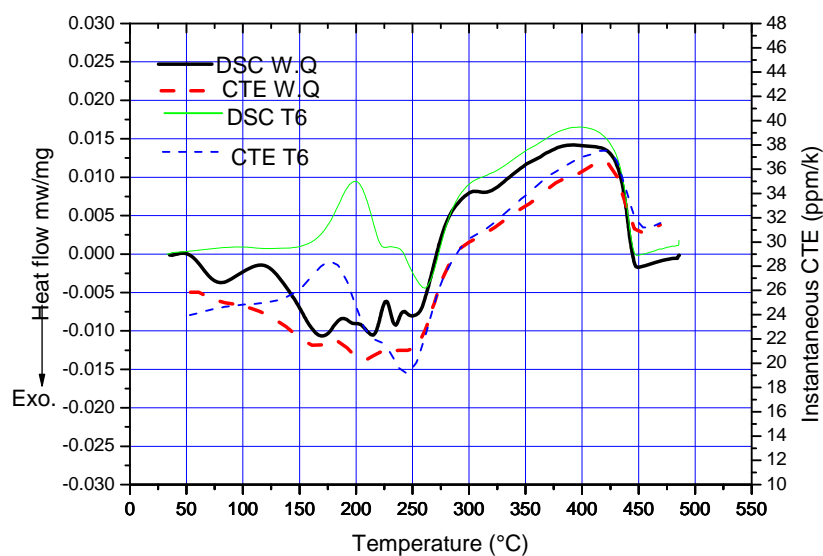


Figure 6.9 Comparing DSC and CTE(T) of Al-Zn-Mg alloy in W.Q and T6 condition

7 Conclusions

7.1. Al-Ge and Al-Ge-Si alloys

Room temperature age hardening mechanisms of AlGe and AlGe₃ alloys were studied by hardness testing, DSC and dilatometry analyses. In the two alloys, hardening at room temperature occurs after seven days and hardness of AlGe₃ alloy is higher than that of AlGe alloy. Addition of Ge promotes not only accelerated aging kinetics but also increases the level of hardness compared to the alloy with low Ge.

Precipitation and dissolution peaks were observed during heating the sample with a rate of 5 K/min from W.Q. It is possible to distinguish the precipitation and dissolution peaks in Al-Ge / Al-Si-Ge alloys by dilatometry tests. DSC and the dilatometry tests confirm each other with respect to Ge (Si) precipitation and dissolution peaks. Considering the agreement between the results of DSC and dilatometry, the dilatometry method can be used successfully to investigate the kinetics of Ge precipitation by different thermal cycles.

Considering the AlGe, the aluminium matrix in W.Q condition is supersaturated in vacancies. The local vacancy concentration directly controls the rate of solute diffusion and this affects the rate of nucleation. It has a dramatic effect on the local rate of clustering and GP zone formation. During the first heating run just after W.Q, the high density of the vacancies in the as-quenched condition increases the nucleation rate and growth rate. During the slow cooling (5 K/min or 1K/min) of the first cycle, the driving force for precipitation will be much smaller. Considering the 2nd and 3rd heating run of the Fig.5.34, no precipitation and as a consequence no dissolution is observed. Some supersaturation of Ge remains even after 1K/min cooling rate, as observed with the slow heating rate in dilatometry.

Considering the alloys AlGe₃ and AlSi₁Ge₅ and comparing them with the alloy AlGe, we see that the difference is not only due to the amount of alloying elements but on the availability of Si. It is known that Ge atoms in solid solution are larger than the Al-matrix atoms (Si atoms are smaller). A higher lattice strain is produced due to Ge atoms in Al-matrix. A high interfacial energy which is characterised by strained interfaces with a high local atomic disorder presents considerable barrier to the homogeneous nucleation of an equilibrium phase within the supersaturated matrix. This could include the reason for the general delay yielding room temperature precipitation of Ge in AlGe alloy. In AlSi alloy Si doesn't precipitate at all at room temperature, Ge precipitation is similar to Si but much slower.

7.2. Al-Mn alloy (AW3003)

The study on this alloy was performed in order to determine whether dilatometry can be used to analyse the effect of super saturation of transition elements.

Dilatometry is sensitive to both the precipitation and dissolution of Mn in AW3003 alloy. Two reactions are evident in CTE(T) diagram of AlMn sample, (1) precipitation of Mn between about 300 and 380°C and (2) slight dissolution of Mn above 450°C. The CTE(T) diagram of this sample rises slightly above 450°C indicating that dissolution is not occurring as rapidly at the high temperature in this sample. Different solution treatment temperatures resulted in different amount of manganese in solid solution. The cooling rate and Mn content in solid solution have the biggest impact on the formation of precipitation. This can be observed in CTE(T) diagram, see figure 5.42a and b.

7.3. Al-Si alloys (4XX.X)

Differential scanning calorimetry (DSC) and dilatometry can be used as efficient methods to study the kinetics of Si precipitation in different Si containing Al-alloy systems. The precipitation of Si causes an additional expansion, and the magnitude of this effect as a function of temperature and time corresponds to the amount and rate of Si precipitation. Growth and dissolution of Si precipitates revealed by dilatometry can be used to differentiate superimposed exothermic and endothermic effects of other precipitates in DSC thermograms.

Fast quenching of AlSi1.7 alloy causes Si-supersaturation. Due to Si precipitation during slow heating an additional expansion (compared with the thermal expansion of pure Al see figure 5.43 (a)) takes place for water quenched AlSi1.7 alloy. The amount and rate of precipitation are directly related with the supersaturated Si by quenching from elevated temperature. By decreasing the solution treatment temperature the precipitation peak moves to higher temperature and the rate of precipitation decreased (see figure 5.43(a)). CTE(T) of this alloy decreases at least above 350 and 400°C due to dissolution of Si.

By increasing Si content in Al-Si alloy (AlSi12), the relative expansions are similar (See table 5.1) after applying the same solution treatment temperatures

7.4 Al-Mg alloy (5xxx)

To reveal phase transformations (precipitation and dissolution) during dilatometric tests, isothermal dilatometry tests were performed. The conclusion is given as follow:

-The isothermal experiments at 200°C show formation of β''/β' which increases the percent linear length change (see figure 5.46(a)). They show dissolution of those phases at 300°C that decreases the percent linear length change (see figure 5.46(b))

7.5 Al-Mg-Si alloys

Differential scanning calorimetry and dilatometry have been used successfully to investigate the precipitations kinetics of the DC and CC 6016 types aluminium alloys.

The precipitation sequence of the supersaturated Al-Mg-Si alloys can be written as

SSSS \rightarrow Mg-Si-vacancy clusters and G.P. zones

$\rightarrow \beta''$ (Mg₅Si₆)-needle precipitates + Si

$\rightarrow \beta'$ -rod shaped precipitates $\rightarrow \beta$ (Mg₂Si)-phase + Si.

The result of DSC and dilatometry implies that precipitation of Si is centered at about 300 °C for W.Q condition, where β' formation is assumed. Maximum rate of change in length occur at the temperature of β' formation (see figure 5.47). There is a little difference between the DSC thermograms and CTE(T) curves of CC and DC 6016 in W.Q condition. The intermetallic line segregation in the centre of the CC 6016 sheet could have also contributed to the thermograms as it consumes some Mg and Si missing for the precipitation kinetics in comparison with the homogeneous DC 6016.2 material.

The increase in hardness is attributed to GP zones and β'' phases. β'' is the most effective hardening phase, which increases with increasing Mg₂Si content of the alloy. The reason for the hardening effect is the interface coherency in Al planes that produces strong strain fields around the precipitates, which slows the movement of dislocations. A high number density of precipitates is responsible for high hardness.

In an alloy with higher Fe content, more Si is bound to the Fe. Consequently, Si concentration in solute solution is lower and precipitation of excess Si will decrease. Excess Si precipitates and produces increased thermal expansion like in Mg-free AlSi alloys. The corresponding DSC thermograms show both Mg₂Si and Si precipitation whereas CTE(T) is dominated by Si precipitation. Dilatometry does not reveal Mg₂Si as mentioned in chapter 6.5. where the volume change between Mg and Si in solid solution and crystalline Mg₂Si is described. The reason of reducing hardness in heat affected zone (HAZ) in Al6008 might be the enhanced formation of Mg and Fe containing π phase (FeMg₃Si₆Al₈) as intermetallic compound while the amount of β'' phase is simultaneously reduced. The absence of GPZ in the HAZ certainly reduces the hardness

with respect to T4 condition. Precipitation of $Al_{10}V$ could not be observed neither by DSC nor CTE.

7.6 Al-Zn-Mg alloy

DSC and dilatometry tests were carried out on AW7349 (1C-A) alloy in three different (W.Q, T4 and T6) conditions. There is a clear correlation between the results of both. Our conclusion can be summarized as follows:

GP(I)-zones are formed over a wide temperature range, from room temperature to 130–140°C. The zones are coherent with the aluminum matrix. After quenching and during natural ageing, some particles are formed. They are identified as pre-precipitate solute clusters or GP zones.

During the early stages of artificial ageing at 100-110°C the solute clusters and/or GP zones dissolve partially and η' precipitates are simultaneously formed.

The partial dissolution of solute clusters/GP zones is accomplished with a significant loss of vacancies; therefore, these point defects could have an important role on the η' precipitation kinetics.

The effect of changing the aging methods is not only to change the driving force for the precipitation, but also to change the volume fraction of GP zones able to act as nucleation sites for η' . This effect, which is a consequence of the different aging, vacancy concentrations present interacts strongly in reversion of GP zones.

7.7 Identification of precipitation

This section describes which precipitate can be identified by dilatometry and which can't. In Al-Cu alloy, according to table 2.1 we could identify only θ phase because the vol./atom of this phase is $0.015\text{nm}^3/\text{atom}$, which is 90% of vol./atom of Al that cause a decrease in volume. We can't identify GPI, GPII (θ'') and θ' phases. Some evidence was given in table 2.2 the volume /atom of S phase is the same as of Al thus we can't identify any phases of this table.

No clear effects could be measured in AW3XXX alloys by dilatometry from CTE(T) curve.

Si precipitation, as well as Ge precipitation, is observed clearly by dilatometry in samples containing supersaturated Si and/or Ge, where the change in atomic volume is $> 20\%$.

In Al-Mg-Si alloy (table 2.4) with surplus of Si we can identify Si precipitates due to almost 31% increasing in volume with respect to Al. Mg_2Si -precipitation doesn't produce significant changes in expansion. As the difference between solute $2Mg+Si$ atoms is only 3-8% in atomic

volume with respect to Mg_2Si corresponding to a theoretical length change of 1-2.6%. The dilatometry curve is dominated by excess Si precipitation whereas the DSC curve represent as superposition of β'' - β' and Si precipitation. The comparison of both measurements allows to extract the Si effect on DSC thermograms. Dilatometry is useful to identify excess Si in 6XXX alloys.

According to table of 2.6, in Al-Zn-Mg alloy we can identify η phase, due to precipitation of this phase we get a big difference in change in vol/atom. The CTE(T) curves reflect the precipitation kinetics of GPZ- η' - η in formation and dissolution. The DSC curves show more oscillation than the CTE(T) curve.

By dilatometry the rate of transformation can be studied more flexible than in the DSC, because heating and cooling rate can be varied much more in the dilatometer. The advantage of dilatometry is in the investigation of isothermal precipitation as shown for Al-Si and Al-Mg. Isothermal calorimetry needs about 15-30 min for stabilization, whereas fast heating in the dilatometer requires only a few seconds after which the length changes can be measured very accurately of alloy systems providing a change of atomic volume $>10\%$ during precipitation or dissolution of precipitates of more than 1 vol%.

REFERENCES

1. E. Totten, D. Scott, Mackenzie Hand book of aluminium **1** (2003)
- 2 G.B. Rüttmann: The future of the aluminium industry, Aluminium, 76,4, (2000) 239-258
- 3 A. Smoel, State and development of some wrought aluminium alloys for special and general Applications, metalurgica **41** 3, 149-155 (2002)
- 4 J. Zander, R. Sandströmand, L. Vitos, Computational material science **41**, 86-95 (2007)
- 5 A.K. Dahle. Heat treatment of aluminium alloys, Encyclopedia of Material science and Technology **3** 2, 1-3 (2001)
- 6 G. Farhadi, Les effets des elements de trace sur les caracteristiques des alliages de type 6XXX Pour les applications automobiles, Ph.D thesis universite du Quebec a Chicoutimi, octobre 1999
- 7 J.C. Zhao, Methods for phase diagram determination, Elsevier Ltd, 2007
- 8 L. Katgerman and D. Eskin, Hardening Annealing and Aging Netherlands, Institute for metal research Delft the Netherlands (2003) 259
- 9 H.E. Boyer and T.L. Gall, Metal hand book 6.1- 6.4 American society for metals, Materials park, OH, 1985
10. M.H. Jacobs, Precipitation hardening, TALAT lecture, University of Birmingham, UK. (1994)
11. M.J. Mageto, TEM study of microstructure in relation to hardness and ductility in Al-Mg-Si (6XXX) alloys Department of Physics Faculty of Natural Sciences and Technology Norwegian University of Science and Technology (NTNU) MSc. Thesis (2003)
- 12 R. Gitter, Euro codes Background and applications, Design of aluminium structure at work shop in Brussels 20 Februar 2008
13. R. Cobden, Aluminium physical properties, characteristics and alloys, TALAT lecture 1501. UK. (1994)
- 14 M. Karlik, B. Jouffrey, Acta Mater **45** (8) (1997) 3251-3263
- 15 L. Loechte, A. Gitt, G. Gottstein, I. Hurtado. Acta Mater **48** (2000) 2969-2984
- 16 T.J. Konno, M. Kawasaki, K. Hiraga, Electron Microsc **50** (2) (2001) 105-111

- 17** T.J.Bastow, S.Celotto, *Acta Mater* **51** (15) (2003) 4621-4630
- 18** A.Hayoune, D.Hamana. Structure evolution during non isothermal aging of a dilute Al-Cu alloy by dilatometric analysis, *Journal of alloys and compounds* **474** (2009)118-123
- 19** N.Y.A. Belov, D.G.Eskin and Andrey A.Aksenov. Multi component phase diagrams applications for commercial aluminium alloys (2005) 47
- 20.** L.F.Mondolfo, *Aluminium alloys structure and properties* (1981)
- 21.**S.C.Wang,M.J.Starink and N.Gao. Precipitation and intermetallic phase in Al-Cu-Mg(Li) base alloys revisited, *Scripta Materialia* **54** (2006)287-291
- 22** J.R.Davis *Aluminium and aluminium alloys ASM hand book* 1993
- 23** T.Sheppard, *Extrusion of aluminium alloys*, Kluwer academic, Dordrecht (1999)
- 24.**C.Cayron, P.A.Buffat, *Acta Mater* **48** (10) 2639(2000)
- 25** R.Vissers, M.A.Vanhuis,J.Jansen, H.W.Zandbergen,C.D.Marioara, S.J.Andersen,*Acta Materialia* **55** (11)(2007)3851-3823
- 26.**M.J.Hass, *Grain boundary phenomena and failure of aluminium alloys*, University of Groningen (2002)
- 27** A.M.Camacho, H.V.Atkinson, P.Kapranos, B.B.Argent, *Acta Mater* **51** (2003) 2319-2330
- 28** G.E.Totten, D.S.Mackenzie, *Handbook of Aluminium, Vol.1, Physical metallurgy and Processes*, (2003)
- 29** K.H.Chen, H.W.Liu, Z:Zhang, S.Li, R.I:Todd, The improvement of constituent dissolution and Mechanical properties of 7075 aluminium alloy by stepped heat treatments, *Journal of material processing technology*, **142** (2003)190-196
- 30** X.Fan, D.Jiang, Q.Meng, L.Zhong. The microstructural evolution of an Al-Zn-Mg-Cu alloy during homogenisation, *Materials Lectures* **60** (2006)1475-1479
- 31** A.Deschamps, F.Livet, Y.Brechet, Influence of pre deformation on aging in an Al-Zn-Mg alloy microstructure evolution and mechanical properties, *Acta Mater* **47** (1)(1999)281-292
- 32** I.J.Polmer, *light alloys forth edition* 2006

- 33** H.K.D.H.Bhadেশia, Differential scanning calorimetry, Lecture University of Cambridge Material science and metallurgy, (2002)
- 34** S.C.Wang, M. J. Starink, N.Gao. Scripta Materials **55**(2007) 933-941
- 35** M.Wierzbinska, G.Mrowka-Nowotnik, Identification of phase composition of AlSi5Cu2Mg aluminium alloy in T6 condition, International scientific journal **30** (2) (2008) 85-88
- 36** M.J.Starink, A.M.Zahra. Low temperature of Al-Mg alloys, Phil.Mag. **76** (1997) 701-714
- 37** G.A.Edwards, K.Stiler.G.L.Dunlop, M.J.Couper. The precipitation sequence In Al-Mg-Si alloys, Acta. Mater 46 (11) 1998, 3893-3904
- 38** A.Deschamps, Y.Brechet, Influence of quench and heating rates on the aging response of Al-Zn-Mg (Zr) alloy, Material science and engineering A251 (1998) 200-207
- 39** M.J.Starink, A.M.Zahra, Precipitation kinetics of an Al-15%Mg alloys, Mater science Forum, Vol.217-222 (1996) 795-800
- 40** K.M.Ralls, T.H.Courtney, J.Wulff, An introduction to Materials Science and Engineering, John Wiley & Sons New York (1976) 542-545
- 41** F.Cverna, Thermal properties of Metals, ASM International Materials, Park, OH (2002) 1-10
- 42** G.W.Ehrenstiner, G.Ridel,P.Trawiel,.Praxis der thermischen Analyse von Kunststoffen, Hanser Verlag, München (1998)141-142
- 43** M.F.Ashby, Material selection and design material property charts ASM Handbooks Vol.20 (1997) 266-280
- 44** T.Kemny,J.Sestak, Comparison of crystallization kinetics determined by isothermal and non iso thermal Methods, Thermoch.Acta 110 (1987) 113-129
- 45** E.Louis, C.Garcia –Cordovilla. The determination of kinetics parameters through the peak peak method for differential scanning calorimetry,J.Therm anal. 29 (1984) 1139-1150
- 46** E.J.Mittemeijer, Analysis of the kinetics of phase transformations, J.Mater.Sci.27 (1992) 3977 3987
- 47** A.K.Galwey, M.E.Brown, Kinetic background to thermal analysis and calorimetry school of chemistry, Queen ´s university of Belfast, Northern Irland, (1998)
- 48** G.W.Smith, Themochimica Act 313.1 (1998) 27-37

- 49** G.W. Smith, N.A. Vaz, *Liq. Cryst.* 3 (1988) 543.
- 50** G.W. Smith, *Int. J. Modern Phys. B* 7 (1993) 4187.
- 51** G.W. Smith, *Mol. Cryst. Liq. Cryst.* 239 (1994) 63.
- 52** A.J. McAlister, J.L. Murray *Bull Alloy Phase Diag* 5 (1984) 341
- 53** L.F. Mondolfo, *Metallography of Aluminium alloy* (1943)
- 54** N. Ryum, *Physical Metallurgy of Heat Treatable Alloys*. in *Proceedings of an International Conference, Charlottesville, Virginia, USA*. 1986
- 55** E. Hornbogen, A.K. Mukhopadhyay, E.A. Starke, *Nucleation of the diamond phase in aluminum-solid solutions*, *Journal of materials science* 28 (1993) 3670-3674
- 56** I. Dutta, S.M. Allen, *A calorimetric study of precipitation in aluminum alloy 6061*, *J. Mater. sci.* 10 (1991) 323-326
- 57** S.K. Bose, R. Kumar, *Rapid solidification of Al-Mg-Si alloys from the liquid state in rapidly quenched metals* (N.J. Gran and B.C. Gressen, eds) 1(1976)169-177
- 58** E. Ozawa, H. Kumar, *Behavior of Excess vacancies during the nucleation of precipitate in aluminum silicon alloys*, *Mater. Sci. Eng.* 8 (1971) 327-335
- 59** D.L. Zhang, *Precipitation of Excess silicon during heat treatment of cast Al-7Wt%Si-0.4Wt%Mg alloy*, *Mat. sci. forum* 217-222 (1996) 771-776
- 60** E.A. Starke, *Aluminium alloys of the 70s.*, *Mat. Sci. Eng.* 29 (2) (1997) 99-115
- 61** P.R. Austen, H.M. Williamson, *The effect of non standard aging treatments on the fracture properties of Al-Mg-7wt%Si alloys*, *Met. Mar.* 20(1975)39-43
- 62** R.C. Dorward, *Preaging effects in Al-Mg-Si alloys containing 0.6 to 0.9 pct Mg₂Si* *Metall. trans.* 4(1973)507-512
- 63** K. Matsuda, H. Gamada, K. Fujii, Y. Uetani, T. Sato, S. Ikeno, *High resolution electron microscopy on the structure of Guinier Preston zones in Al-1.6 mass pct. Mg₂Si alloy*, *Metall. Mater. Trans. A* 29(1998)1161-1168
- 64** D.W. Pashley, J.W. Rhodes, A. Sendorek, *Delayed aging in aluminium –magnesium-silicon alloys effect on structure and mechanical properties*, *J. Inst. Metals*, 94(1996)41-49
- 65** M.H. Jacobs, *The structure of the metastable precipitates formed during aging of an Al-Mg-Si alloy*, *Phil. Mag.* 26(1972)1-13

- 66** A.Bbarcza, Magnetostriction in rare earth element measured with capacitance dilatometry, Diplomarbeit Universität Wien 2006
- 67** D.Scott Mackenzie, G.E.Totten, Analytical characterization of aluminum, steel and superalloys (2006) 304.
- 68** J.M.Papazian, Calorimetric studies of precipitation and dissolution kinetics in Aluminium 2219 and 7075 Metall. Trans. A.13A(1982) 761-769
- 69** R.Delasi, P.N.Adler, Calorimetric studies of 7000 series aluminium alloys, Metall.Trans.A.8A (1977) 1177-1183
- 70** I.Kechukwuka, N.A.Oguocha, Characterization of aluminium alloy 2618 and its composites containing aluminium particles PhD thesis 1999
- 71** F.A.Lasagni, The role of Si on the microstructure of Al casing alloys and short fiber composites PhD thesis 2006, Vienna University of Technology
- 72** M.J.Starink, Analysis of aluminium based alloys by calorimetry, quantitative analysis of reactions and reaction kinetics, International materials reviews 49 (3-4) (2004) 195
- 73** R.L.Hassel, American laboratory Vol.1 (1991)
- 74** R.Schneider, PhDthesis 2008 TU-Wien
- 75** S.Srikanth, D.Sanyal and P.Ramach and Rarao, Evaluation of the Al-Ge system Calphad 20 (3) (1996) 321-332
- 76** V.Radmilovic, D.Mittin, A.J.Tolley, U.Dahmen and J.Morris, Resistance to shape refinement of precipitates in Al-(Si,Ge) alloys during thermal cycling, Metall. Trans. A 34A (2003) 543-551
- 77** B.Dracup, P.E.A.Turchi, V.Radmilovic, U.Dahmen and J.W.Morris, Validation of predicted precipitate composition in Al-Si-Ge, Metall.Trans. A 35A (2004)2305-2311
- 78** E.Hornborgen, A.K.Mukhopadhyay and E.A.Stark, An exploratory study of hardening in Al-(Si-Ge) alloys, Z.Metallk. 83 (8) (1992) 577-584
- 79** E.Hornborgen, A.K.Mukhopadhyay, and E.A.Starke, precipitation hardening of Al-(Si-Ge) alloy, Scripta metal Mater 27(6) (1992) 733-738
- 80** M.M.Makhlof and H.V.Guthy, The aluminium silicon eutectic reaction mechanisms and crystallography, Journal of light metals 1 (2001)199-218

- 81** M.Warmuzek, Aluminium- Silicon casting alloys Atlas of microfractographs, ASM materials park OH 44073 (2004)
- 82** F.A. Lasagni, H.R.Mohammadian, A.Falahati, H.P.Degischer, Institute of Materials Science and Technology; Vienna University of Technology; Vienna, Austria.
- 83** A.Gaber, N.A.Fify, M.S.Mostafa, Gh.Abbady, Effect of heat treatment on the precipitation in Al-Mg-Si alloys. Journal of alloys and compounds (2009)
- 84** L.C.Dona, Y.Ohmori and K.Naakal, Mat.Trans. A41 (2) (2003) 300
- 85** A.K.Gupta, D.J.Lloyd, S.A.Court , Precipitation hardening in Al-Mg-Si alloys with and without excess Si , Material science and engineering A 316 (2001) 11-17
- 86** J.Buha, R.N.Lumley, A.G.Grosky, Secondary ageing in an aluminium alloys 7050, Material science and engineering A 492 (2008) 1-10
- 87** Y.J.Li,L.Arnberg, Evolution of eutectic intermetallic particles in DC-cast AA3003 alloy during heating and homogenization, Material science and engineering 347 (2003) 130-135
- 88** Y.J.Li,L.Arnberg, Quantitative study on the precipitation behaviour of dispersoids in DC-cast AA3003 alloy during heating and homogenization ,Acta Material 51 (2003) 3415-3428
- 89** A.Falahati; G.Requena, F.A.Lasagni, H.R.Mohammadian, H.P.Degischer, Precipitation kinetics of Si in Al-Si alloys revealed by dilatometry, Institute of material science and technology, Vienna University of technology 2008
- 90** S.Nebti,D.Hamana and G.Cizeron, Calorimetric study of pre-precipitation and precipitation in Al-Mg alloy Acta metall.mater 43 (9) (1995) 3583-3588
- 91** L.Hadjadj, R.Amira,D.Hamana, A.Mosbah, Characterization of precipitation and phase transformations in Al-Zn-Mg alloy, by the differential dilatometry, Journal of alloys and compounds 462 (2008) 279-283
- 92** R.G.Mortimer, Physical chemistry, Third edition, Elsevier Inc. 2008
- 93** K.C.Russel, Phase transformation, ASM (1970)
- 94** O.R.Myhr, O.Grong, Modeling of non-isothermal transformations in alloys containing a particle distribution, Acta Materials 48 (1605-1615), (2000)116,17,125,32
- 95** F.J.de Zwaan, Mathematical models for simultaneous particle dissolution and nucleation during heat treatment of aluminium alloys, PhD thesis Delft University of Technology (2006)

- 96** W.D.Callister Jr., Material science and engineering- an introduction, John Wiley & sons, Inc. fifth edition (1999) 6,8,10,13
- 97** X.Wang, W.J.Poole, S.Esmaeili, D.J.Lloyd and J.D.Embury, Precipitation strengthening of the aluminium alloy AA6111, *Met, Materials Trans. A* 34 (2003) 2913-2924
- 98** R.S. Yasser,D.P.Field, and H.Weiland, The effect of pre deformation on the β'' and β' precipitates and the role of Q' phase in an Al-Mg-Si alloy, *Scripta Materialia* , 53 (31) (2005) 299-303
- 99** W.F.Miao and D.E.Laughlin, Precipitation on hardening in aluminium alloy 6022, *Scripta Mater*, 40 (7) (1999) 873-878
- 100** A.K.Gupta, D.J.Lloyd and S.A.Court, Precipitation hardening process in an Al-0.4%Mg-1.3%Si-0.25%Fe aluminium alloy,*Mater. Sci, Eng. A* 301 (2000) 140-146
- 101** L. Zhen and S.B.Kang, DSC analyses of the precipitation behaviour of two Al-Mg-Si alloys naturally aged for different times, *Materials letters*, 37 (1998) 349-353
- 102** G.B.Burger, A.K.Gupta, P.W.Jeffrey and D.J.Lloyd, Microstructure control of aluminium sheet used in automotive applications, *Material characterization* 35 (1995) 23-39
- 103** I.Dutta and S.M.Allen, A calorimetric study of precipitation in commercial aluminium alloy 6061, *J. of Materials Sc.etters* 10 (1991) 323-326
- 104** G.A.Edwards, G. L. Dunlop and M.J.Couper, Fine scale precipitation in Al alloy 6061, 4th Int conference on aluminium alloys, Georgia Institute of Technology School of Materials Science and Engineering Atlanta GA, (1994) 668
- 105** A.K.Gupta, and D.J.Lloyd, The precipitation in a super purity Al-Mg-Si alloy, 3rd Int. Conf. aluminium alloys.
- 106** Y. Birol, DSC Analysis of the precipitation reaction in AA 6005 alloy, *Journal of Thermal Analysis and Calorimetry*, Vol. 93 (3)(2008) 977-981
- 107** G.J.Tomas, *Inst. Metals* 90 (1962) 57
- 108** M.H.Jacobs, *Phil. Mag.* 26 (1972) 1
- 109** A.K.Mukhopadhyay, Q.B.Yang, and S.R.Singh, *Acta. Metall.* 42 (1994) 3083
- 110** J.Lendvai, G.Honyek and I.Kovacs, *Scripta Metall* 13 (1979) 593

- 111** D. Mitlin, U. Dahmen V. Radmilovic J.W. Morris, Jr, Precipitation and hardening in Al–Si–Ge, Materials Science and Engineering A301 (2001) 231–236
- 112** H.C.Zeng, Ostwald Ripening: A Synthetic Approach for Hollow Nanomaterials, Current Nanoscience, 3(2007) 177-181
- 113** <http://xray.bmc.uu.se/terese/crystallization/tutorials/tutorial6.html>
- 114** C.C.Riccardi, H.E.Adabbo, and J.J.Williams. J.Appl.Polym.Sci. **29**. 2481, 1984
- 115**.V.M.Gonzalez and N.Casillas. Polym.Eng. and Sci. 29, 295, 1989
- 116** H.E.Kissinger. Anal. Chem.29, 1702, 1957
- 117** Internal technical report. Rohm and Haas Co., May 1989.
- 118** <http://environmentalchemistry.com/>